UNIVERSITY OF CALIFORNIA,
IRVINE

Optical Nanoantennas for Sensors, Microscopy and Spectroscopy

DISSERTATION

submitted in partial satisfaction of the requirements
for the degree of

DOCTOR OF PHILOSOPHY

in Electrical and Computer Engineering

by

Mahsa Darvishzadeh Varcheie

Dissertation Committee:
Professor Filippo Capolino, Chair
Professor Regina Ragan
Professor Eric Potma

2019

TABLE OF CONTENTS

LIST OF FIGURES

ACKNOWLEDGMENTS

I'm deeply indebted to my committee chair, Professor Filippo Capolino, for his invaluable guidance, inspiration and suggestions in my quest for knowledge. His enthusiasm and passion for perfection in engineering research have been a constant source of inspiration to me.

I would like to extend my sincere thanks to my committee members, Professor Regina Ragan and Professor Eric Potma who provided guidance and support in our collaborations continuously. I am indebted to their very valuable comments on this thesis.

Every result provided in this thesis was accomplished with the valuable help and support of my fellow lab mates and collaborators. I acknowledge the contribution of my collaborators, Dr. Regina Ragan, Will Thrift, Cuong Nguyen, and Dr. Jinwei Zeng and my lab mates Dr. Caner Guclu, Dr. Mohammad Kamandi and Dr. Mehdi Veysi who I had the opportunity to work with and learn from. I thank the former and current members of our research group, in particular Dr. Mohammad Albooyeh, Hamidreza Kazemi, Mohsen Rajaei, and Ahmad Tariq Almutawa. The former and current staff at the Electrical Engineering department always helped us in most urgent conditions. Therefore, I am very grateful to them, especially to Amy Pham, Susan Staebell, Loretta Waltemeyer, Luba Konkova and Elvia Salas.

My acknowledgement would be incomplete without thanking the biggest source of my strength, my family. The blessings of my parents and the love and care of my sisters and my husband have all made a tremendous contribution in helping me reach this stage in my life.

I like to thank Prof. G.P. Li and UCI INRF staff, Jake Hess, Richard Chang and Steven Martinez for helping me out to learn microfabrication process.

Last but not the least, I am grateful for the funding sources that allowed me to pursue my graduate school studies: The National Science Foundation and the USA Keck Foundation.

The text of this dissertation is a reprint of the materials as they appear in American Physical Society and Optical Society of America Journals. The co-authors listed in these publications directed and supervised research which forms the basis for the dissertation.

CURRICULUM VITAE

Mahsa Darvishzadeh Varcheie

2019 Ph.D. in Electrical and Computer Engineering, University of California, Irvine

2014 M.Sc. in Electrical Engineering, University of Tehran

2011 B.Sc. in Electrical Engineering, University of Tehran

EXPERIENCE

2019 Sr. Concept Engineer, Carl Zeiss Meditec, Dublin, CA

2014-2019 Graduate Student Researcher, Electrical Engineering and Computer Science, University of California Irvine, Advisor: Prof. Filippo Capolino

2018 PhD Engineering Intern, Medtronic, Northridge, CA, USA

FIELD OF STUDY

Nano-Optics, Spectroscopy, Optical Nanoanatennas, Electromagnetic modeling, Numerical methods

PUBLICATIONS

J1. **M. Darvishzadeh-Varcheie**, W. J. Thrift, M. Kamandi, R. Ragan, and F. Capolino, "Two-Scale Structure for Giant Field Enhancement: Combination of Rayleigh Anomaly and Colloidal Plasmonic Resonance," Phys. Rev. Applied, vol. 11, no. 5, p. 054057, May 2019.

J2. **M. Darvishzadeh-Varcheie**, C. Guclu, and F. Capolino, "Magnetic nanoantennas made of plasmonic nanoclusters for photoinduced magnetic-field enhancement," Phys. Rev. Applied, Vol. 8, No. 2, 024033, 2017

J3. **M. Darvishzadeh-Varcheie**, C. Guclu, R. Ragan, O. Boyraz, and F. Capolino, "Electric field enhancement with plasmonic colloidal nanoantennas excited by a silicon nitride waveguide," Optics Express, Vol. 24, No. 25, pp. 28337- 28352, 2016.

J4. **M. Darvishzadeh-Varcheie**, M. Kamandi, M. Albooyeh, and F. Capolino, "Optical magnetic field enhancement at nanoscale: a nanoantenna comparative study", Optics Letters (in print), 2019.

J5. J. Zeng, **M. Darvishzadeh-Varcheie**, M. Albooyeh, M. Rajaei, M. Kamandi, M. Veysi, E. O. Potma, F. Capolino, and H. K. Wickramasinghe, "Exclusive Magnetic Excitation Enabled by Structured Light Illumination in a Nanoscale Mie Resonator," ACS Nano, Vol. 12, No. 12, pp 12159–12168, 2018.

J6. W. J. Thrift, C. Q. Nguyen, **M. Darvishzadeh-Varcheie**, S. Zare, N. Sharac, R. Sanderson, T. Dupper, A. Hochbaum, F. Capolino, M. J. Abdolhosseini Qomi, and R. Ragan, "Driving Chemical Reactions in Plasmonic Nanogaps with Electrohydrodynamic Flow," ACS Nano, Vol. 11, pp. 11317–11329, 2017.

J7. J. Zeng, M. Kamandi, **M. Darvishzadeh-Varcheie**, M. Albooyeh, M. Veysi, C. Guclu, M. Hanifeh, M. Rajaei, E. O Potma, H. K. Wickramasinghe, F. Capolino, "In pursuit of photo-induced magnetic and chiral microscopy," EPJ Appl. Metamat., vol. 5, p. 7, 2018.

J8. C. Q. Nguyen, W. J. Thrift, A. Bhattacharjee, S. Ranjbar, T. Gallagher, **M. Darvishzadeh-Varcheie**, R. N. Sanderson, F. Capolino, K. Whiteson, P. Baldi, A. I. Hochbaum and R. Ragan, "Longitudinal Monitoring of Biofilm Formation via Robust SERS Quantification of Pseudomonas aeruginosa-Produced Metabolite," ACS Appl. Mater. Interfaces, Vol. 10, No. 15, pp 12364–12373, 2018.

ABSTRACT

Optical Nanoantennas for Sensors, Microscopy and Spectroscopy

By

Mahsa Darvishzadeh Varcheie

Doctor of Philosophy in Electrical and Computer Engineering

University of California, Irvine, 2019

Professor Filippo Capolino, Chair

Metallic nanosctructures possess electromagnetic properties useful for various applications, such as surface enhanced Raman spectroscopy (SERS), harmonic generation and solar cells. Specifically, because of their ability in confining electromagnetic fields to nanoscopic dimensions, they provide an exquisite platform for conducting studies on molecules placed in their vicinity. In this dissertation, I introduce and study various plasmonic nanostructures to achieve electric and magnetic field enhancement for spectroscopy and microscopy applications.

First, I investigate feasibility of CMOS-compatible optical structures to develop novel integrated spectroscopy systems. I show that local field enhancement is achievable utilizing dimers of plasmonic nanospheres that can be assembled from colloidal solutions on top of a CMOS-compatible optical waveguide. The resonant dimer nanoantennas are excited by modes guided in the integrated silicon nitride waveguide. Specifically, I investigate how the field enhancement depends on dimer location, orientation, distance and excited waveguide mode. However, the field enhancement achievable with using oligomers is limited due to inherent losses of plasmonic particles. Thus, I study a novel structure called two-scale, in which Rayleigh anomaly caused by a 1D set of periodic nanorods is utilized. A thorough study of this structure is carried out by using an effective analytical-numerical model which is also compared to full-

wave simulation results. Experimental results comparing enhancements in surface enhanced Raman scattering measurements with and without nanorods demonstrate the effectiveness of a Rayleigh anomaly in boosting the field enhancement.

The other side of the dissertation is dedicated to magnetic field enhancement. I propose various metallic and dielectric nanostructures for local magnetic field enhancement at optical frequencies. I show that dielectric structures can be a good alternative for their plasmonic counterpart due to their low loss. The idea behind each structure is supported by results from full-wave simulations. More importantly, I utilize azimuthally polarized beam as a way of boosting local magnetic field and isolating it from electric field. The magnetic field enhancement of these structures can be utilized in studying magnetic dipole transitions, magnetic imaging and enhanced spectroscopy applications.

CHAPTER 1 : INTRODUCTION

Sec. 1.1 Background

Enhancing light-matter interaction has attracted tremendous research interest due to the reliance of various applications ranging from sensing [1]–[4] and solar cells [5], [6] to harmonic generation enhancement [7]–[9] and perfect lensing[10] on local field enhancement. Owing to this fact, metallic nanoparticles have been the focus of attention for their ability to provide giant field localization at subwavelength scale. The peculiar properties of these structures originate from the coherent oscillations of free electrons near the surface of metals. These free electrons can propagate over the surface of extended metallic structures, while, they bring about the localized surface plasmon polaritons (LSPR) over the surface of metallic nanostructures where the size of the particle is comparable to the wavelength of light. Since the fields are confined over the nanoparticle surface, an LSPR has a small mode volume, thus, providing giant electromagnetic field enhancement. The simplest form of such a nanostructure is a nanosphere which can be viewed as an oscillating dipole. If I bring two nanospheres very close to each other, these dipoles interact with each other. These coupled LSPRs can lead to a very strong electromagnetic field. Their resonance frequencies are also determined by the geometric parameters of gap and the material of metallic objects.

Enhancing the electric field in near-field is crucial for sensory applications. Raman spectroscopy is a vibrational spectroscopy technique that provides information about the chemistry-specific signatures of analytes. However, Raman spectroscopy can't identify trace numbers of molecules due to low scattering efficiencies. Indeed, typical values for Raman scattering cross-sections are very low compared to other optical processes (like Florescence), ranging between 10^{-31}–10^{-29} cm^2/molecule[11]. Thus, a strong alternative method called surface enhanced Raman spectroscopy (SERS) have been developed to increase

Raman scattering by orders of magnitude. SERS utilizes the strong electric field to enhance the cross section of Raman scattering from analytes.

On the other hand, enhancing magnetic field is more difficult than its electric counterpart at optical frequencies. Conventionally, ferromagnetic materials are exploited to enhance the local magnetic fields. However, in the optical regime, the magnetic properties of materials are rather weak that I must resort to other means to enhance the magnetic near-field. The overall magnetism of a metamaterial can be engineered by tailoring the artificial magnetic resonance in "meta-atoms". These meta-atoms are responsible to create magnetic dipoles for which the ratio of the magnetic to electric near-field is enhanced. Many different structures such as metallic split ring or U-shaped resonators and nanostructured dielectric surfaces have been used to create a magnetic dipole to exclusively enhance the magnetic field [12]–[15]. The ability of circular nanostructures to develop magnetic moments offers the possibility to locally enhance the magnetic near-fields[16]–[20]. These types of structures are made of plasmonic particles. However, plasmonic structures are known to be affected by unavoidable losses in metals in optical frequencies. This inherent problem of metals can be avoided by using subwavelength dielectric particles with high permittivity providing a new paradigm to constitute building blocks of novel nanostructures for magnetic field enhancement [21]–[25]. Unlike plasmonic antennas where oscillations of the free electron plasma and collective lattice vibrations dictate the local response of the light-matter interaction, dielectric antennas rely on the fields and displacement currents induced in the antenna structure. On the other hand, structured light can be emploited to further enhance the magnetic field and separate the magnetic field enhancement from the electric dominant field. The magnetic field enhancement is crucial in studying the magnetic properties of materials and in magnetic microscopy to gain more insight into the properties of samples.

Sec. 1.2 Overview of dissertation

I have developed new structures and novel class of nanoparticles to enhance light-matter interaction to achieve electric and magnetic field enhancement for applications in optical spectroscopy and microscopy.

Specifically, I introduced two structures for enhancing electric field. In the first one, I integrated the SERS substrate consisting of gold oligomers over a waveguide to have an integrated CMOS-compatible sensor based on SERS. In the second design, I introduced a synergic structure called two-scale and made use of two parallel configurations for further enhancing the electric field 1) plasmonic oligomers which cause plasmonic resonance 2) 1D periodic nanorods which enable the Rayleigh anomaly. On the other hand, I introduced and thoroughly studied various structures to enhance magnetic field. Specifically, I designed different metallic and dielectric structures to enhance the local magnetic field and compared their performance under similar condition. I employed a structured beam as an excitation to achieve maximum magnetic to electric field enhancement. Specifically, I utilized vector beams with cylindrical symmetry, or so-called vortex beams, which are experimentally functional in the selective excitation of Mie resonances in dense dielectric particles[25], [26].

Sec. 1.3 Organization of dissertation

The dissertation is organized into Chapters that involve enhancing electric field for SERS and enhancing magnetic field for microscopy applications.

Chapter 2: I investigate the feasibility of CMOS-compatible optical structures to develop novel integrated spectroscopy systems. I show that local field enhancement is achievable utilizing dimers of plasmonic nanospheres that can be assembled from colloidal solutions on top of a CMOS-compatible optical waveguide. The resonant dimer nanoantennas are excited by modes guided in the integrated silicon nitride waveguide. Simulations show that 100-fold electric field enhancement builds up in the dimer gap as compared to the waveguide evanescent field amplitude at the same location. I investigate how the field enhancement depends on dimer location, orientation, distance and excited waveguide mode.

Chapter 3: I propose a CMOS-compatible surface enhanced Raman spectroscopy (SERS) scheme based on integrating plasmonic colloidal nanoantennas over silicon nitride dielectric ridge waveguide. In standard SERS experiment, the analytes are placed on a SERS substrate and excited with a laser and the SERS spectrum is collected by an objective lens. While this configuration is useful for applications in laboratories, it is not suitable for sensory applications in portable devices. I bridge the gap between CMOS-compatibility and high sensitivity by integrating plasmonic colloidal nanoantennas onto an optical waveguide. I compare my proposed structure with standard SERS substrate for excitation and collection of SERS signal and provide some insight for designing the waveguide and the nanoantennas.

Chapter 4: I demonstrate theoretically and experimentally a two-scale architecture able to achieve giant field enhancement by simultaneously exploiting both the Rayleigh anomaly and localized surface plasmon resonance. Metallic oligomers composed of colloidal nanospheres are well-known for the ability to strongly enhance the near-field at their plasmonic resonance. However, due to intrinsic nonlocality of the dielectric response of the metals along with their inherent loss, the achievable field enhancement has an ultimate constraint. I demonstrate that combining plasmonic resonance enhancements from oligomers, with feature size of tens of nanometers, with a Rayleigh anomaly caused bya1Dset of periodic nanorods, having a period on the order of the excitation wavelength, provides a mean to produce enhancement beyond that constrained by losses in near field resonances. Metallic oligomers are chemically assembled in between the periodic set of nanorods that are fabricated using lithographic methods. The nanorod periodicity is investigated to induce the Rayleigh anomaly at the oligomers plasmonic resonance wavelength to further enhance the field in the oligomers' hot spots. A thorough study of this structure is carried out by using an effective analytical-numerical model which is also compared to full-wave simulation results. Experimental results comparing enhancements in surface enhanced Raman scattering measurements with and without nanorods demonstrate the effectiveness of a Rayleigh anomaly in boosting the field enhancement. The proposed structure is expected to be beneficial for many applications ranging from medical diagnostics to sensors and solar cells.

Chapter 5: I combine the plasmonic resonance of the oligomers along with the Rayleigh anomaly achieved due to the presence of the periodic 2D nanorods to gain further field enhancement compared to oligomers alone when illuminated with an incident plane wave. Compared to 1D 2scale structure, the new scheme eliminates the limitation of dependency of the field enhancement on the direction of oligomers axis.

Chapter 6: In this chapter, I focus on a category of nanoantennas called magnetic nanoantennas made of a circular cluster of gold nanospheres that leads to enhanced local magnetic field oscillating at optical frequency. I elaborate on the magnetic field enhancement and the magnetic-to-electric-field ratio, i.e., the local field admittance, when the nanoantenna is illuminated by a single plane wave and by superposition of two plane waves to maximize the magnetic-only response. Single-dipole approximation is used to analyze magnetic nano-antennas and is verified by our findings with full-wave simulations. I derive a formula that estimates the natural frequency associated to the magnetic resonance of a circular plasmonic cluster with an arbitrary number of plasmonic nanospheres. Lastly, I classify clusters based on their quality factor and their ability to enhance the magnetic field and discuss the surface area with strong magnetic field provided by the plasmonic cluster.

Chapter 7: I propose various metallic and dielectric nanostructures for local magnetic field enhancement at optical frequencies. I elaborate on the origination of the magnetic field enhancement in each structure and define figure of merits to compare the ability of the structures to enhance magnetic field. I show that dielectric structures can be a good alternative for their plasmonic counterpart due to their low loss. The idea behind each structure is supported by results from full-wave simulations. The magnetic field enhancement of these structures can be utilized in studying magnetic dipole transitions, magnetic imaging and enhanced spectroscopy applications.

CHAPTER 2 : ELECTRIC FIELD ENHANCEMENT WITH PLASMONIC COLLOIDAL NANOANTENNAS EXCITED BY A SILICON NITRIDE WAVEGUIDE

Sec. 2.1 Motivation

The use of nanophotonic sensors enables on-site real-time qualitative detection of molecules or bio chemical agents [27]–[31] with detection limit approaching to single molecule level, and hence leads also to deep understanding of biological and chemical processes that are useful for medical diagnosis[32]–[37]. Using metal nanostructures for this purpose has been the subject of many studies[38]–[40] due to the strong near-field plasmonic coupling and local field enhancement that arise between nanospheres in such configurations. Moreover, metal nano architectures may lead to strong surface enhanced Raman scattering (SERS) intensities[41]–[43] depending on parameters such as size, shape, morphology, arrangement, and local environment. In particular, SERS is an optical spectroscopy method that can use nanoantenna surfaces to enhance signals of light scattered from molecular vibrations for detection of trace amounts of chemical and biological agents[44]. Surface plasmon excitation of a metallic structure in the vicinity of sample molecules is a key factor in the enhanced detection limits in SERS. In[45], it has been shown that the SERS enhancement is proportional to the field enhancement with the forth power (assuming that excitation and scattered frequencies are very close to each other). Surfaces of plasmonic nanosphere clusters have been shown to provide large electric field hot spots [46]–[49] and they have been utilized in SERS[50]–[53] where the number of particles per cluster and the cluster separation are stated as important factors for increasing the SERS intensity. An exponential dependence between SERS enhancement factor and gap spacing has been experimentally observed in [54]. Also it has been shown that surfaces made of regular

arrays made of plasmonic nanospheres have the capability to provide even stronger signals than non-arrayed surfaces[48], [49].

Nanosphere-based cluster assemblies in prior studies have exhibited signal enhancements in SERS sensors. However, the challenge of fabricating systems with high reproducibility in SERS response across the sensor surface is not frequently addressed. To overcome this challenge, in [52], [55] an innovative method for fabricating self-organized clusters of metal nanospheres with nanometer gap spacing on diblock copolymer thin films was successfully investigated. Specifically, monodisperse, colloidal gold nanospheres are attached on chemically functionalized polymer regions on a self-organized diblock copolymer template to engineer a high density of hotspots over large areas while using low cost fabrication methods. Although single molecule detection limits using nanostructured surfaces have been demonstrated previously, issues of large scale fabrication cost, shelf life, reproducibility in detection response, and integration have eluded researchers and this has resulted in limited technological impact.

In this chapter I investigate an on-chip architecture that eliminates structural constraints of an external microscope and integrates the entire excitation and detection mechanism into a single waveguide; thus reducing size and cost, increasing portability, usage flexibility and robustness of future spectroscopy based sensors. On chip spectroscopic measurements are enabled by silicon compatible materials with low loss at visible and at near IR frequencies. Here, the integration of nanoantennas with waveguides that I propose is a spectrometer building block which addresses the above challenges and only requires smaller sample solution volumes in comparison with open systems. With this goal in mind, I investigate the field enhancement capability of plasmonic nanoantennas composed of nanospheres from colloidal solution located on the surface of silicon nitride (Si_3N_4) waveguides. Silicon nitride waveguides may serve as both illumination and detection channels for exciting and collecting signals from nanoantennas. The silicon nitride waveguide platform is proposed instead of a silicon-on-insulator (SOI) platform for integrated photonic circuits[56]–[58] due to its advantages such as absence of multi photon absorption process[59],

lower fabrication cost and less propagation loss[60] at both visible and near infrared[61], [62]. infrared[61], [62]. In particular, I aim at sensing with wholly integrated system for bio applications, where most of the experimental work happens below 800nm, and silicon is not suitable for this wavelength range due to its absorption spectrum. Moreover in [63] authors fabricated a sub-micron silicon nitride waveguide, experimentally characterized the modal dispersion and loss of the guided wave and demonstrated that silicon nitride can be an alternative to SOI platform. The scheme of assembling dimer nanoantennas on the silicon nitride waveguides from colloidal solution allows for numerous nanoantennas present on the surface of the waveguide with high density which can be done via self-assembly on a chemically functionalized copolymer template. I assume in this investigation that dimer nanoantennas on the waveguides are separated by sufficient distances and do not couple with each other such that each nanoantenna can be modeled as an isolated nanoantenna integrated with the waveguide. However, to verify our assumption about considering each dimer isolated, I study also the effect of coupling between different nanoantennas, with different distances and orientations in Section 2. In other words, our goal is to investigate a mechanism for field enhancement by using nanoantennas coupled to and excited by the integrated waveguide, that can fabricated at lower cost compared to e-beam lithography that may generate a breakthrough in portable and affordable sensors. Hence, in the following I carry out the investigation on the performance of a dimer nanoantenna on top of a waveguide, and observe how the field enhancement depends on various geometrical factors.

The chapter is organized as follows. First, I demonstrate an E-field enhancement results pertaining to cases expected in experimental specimens, so I assume that a thioctic acid molecular layer (used for assembly) covers the gold nanosphere dimer on top of the waveguide to model realistic chemical and physical composition of the fabricated samples. Modeling of this thin layer requires fine meshes, which requires extra computational resources. Therefore, after investigating how the layer thickness affects the performance of the waveguide driven nanoantenna, I remove it to make our model simpler from the numerical point of view. I initially assume that the dimer is ideally aligned along the x-axis on top of the

middle of waveguide. Then I further analyze the dependence of the field enhancement on the waveguide modes, geometrical parameters such as waveguide dimensions, dimer location and orientation, the gap between nanospheres, and I study the coupling effect of different nanoantennas on each other. Finally, I compare the field enhancement performance of the proposed waveguide-driven nanoantenna structure with a more traditional way to conduct spectroscopy, i.e., with that consisting of the same nanoantenna dimer placed on top of a multilayer composed of silicon nitride on top of glass, with the same thicknesses as in the waveguide case, illuminated by an external plane wave. I conclude that the field enhancement is comparable.

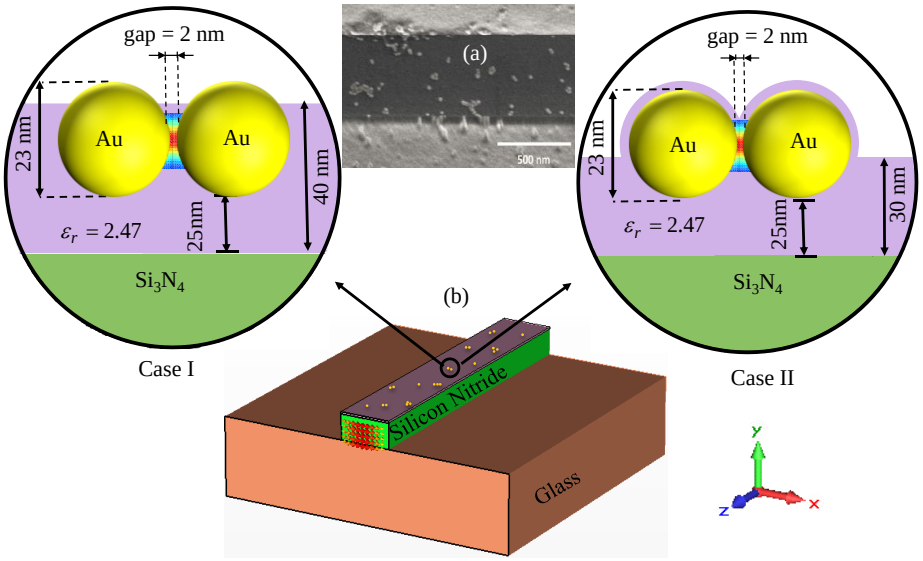

Fig. 2-1. (a) Scanning electron microscope (SEM) image with colloidal gold nanospheres on top of silicon nitride waveguide [38], (b) Proposed integrated CMOS-compatible waveguide with plasmonic nanoantennas (monomers, dimers, etc) immersed in a dielectric layer (represented in purple) covering the waveguide. The two examples, namely Case I and Case II, are investigated for field enhancement. In this chapter, I investigate the optical excitation of a dimer via guided modes in a silicon nitride waveguide, though other waveguide material choices could be utilized as well. In the bottom, the cross section field distribution of the fundamental propagating waveguide mode is shown, whereas on the top, the insets show the dimensions of the dimer and the "hot spot" where the strongest field occurs as a result of waveguide excitation.

Sec. 2.2 Field enhancement by a nanoantenna integrated with a waveguide

In previous works, as in[50]–[53], nanostructured surfaces made of nanospheres were investigated for detections of low molecular concentrations. The electric field enhancement is a critical parameter in decreasing detection limit down to single molecule level. Here I propose the use of a resonant plasmonic nanoantenna integrated with a CMOS-compatible waveguide to provide strong field enhancement. Specifically, the nanoantenna is composed of a dimer of gold nanospheres sitting above a silicon nitride waveguide that provides the optical excitation as shown in Fig. 2-1. The chemical assembly procedure of[52] and[55] involves depositing gold nanospheres with thioctic acids ligands from colloidal solution on a diblock copolymer thin film composed of poly(methyl methacrylate) (PMMA) and polystyrene (PS-b-PMMA). Nanospheres chemically attach to PMMA domains that are recessed with respect to PS regions due to the chemical functionalization process[55]. This thin film layer on top of the waveguide (shown in purple in Fig. 2-1) represents here the combination of thioctic acid ligands and copolymer template. The SEM picture in Fig. 2-1(a) shows various plasmonic gold nanoantennas (monomers, dimers, trimers, etc) assembled on PMMA domains on the PS-b-PMMA copolymer template, covering the top surface of a silicon nitride waveguide[52], [53], [55]. The SEM image demonstrates resulting nanoantennas via colloidal assembly of nanospheres via diffusion that creates random geometries with varying field enhancement ratios on top of the waveguide surface. The geometries in Fig. 2-1(b) and the two circular insets show the geometry considered and investigated in this chapter via full-wave numerical simulations as the deposition process can be varied to produce a large fraction of dimers on the surface[64]. In this article I first investigate the field enhancement produced by a dimer on top of the waveguide. In fact such nanoantennas with subwavelength sizes, in most of the cases, can be treated as isolated scatterers that do not couple significantly with other dimers based on the assumption that dimer density is not too high on the waveguide surface. The validity of this assumption is indeed shown later on in this chapter where I study the effect of

the coupling by considering different nanaoantennas with different orientations and distances from our main dimer.

The significant difference between the proposed structures in Fig. 2-1. and previous work such as[51], is the integrated excitation method; instead of illuminating the structure with an external beam, as in[51], the gold dimer is excited by the tail field of a guided mode propagating inside a waveguide on a glass substrate.

For all cases reported here, the vertical distance from the bottom of the nanospheres to the top surface of the silicon nitride waveguide is denoted by h and the shortest distance between the two nanospheres' surfaces is called the "gap", as shown in Fig. 2-1(b). According to the SEM images of a fabricated sample reported in[51]–[53], [55], an experimentally achievable gap between the nanospheres with diameters of 23 nm is 1-2 nm. Static, reproducible gap spacings have been achieved for distances between 0.9nm-5.3nm using small molecule linkers and DNA origami[65]–[68]. Highly monodisperse particles with ~10% relative standard deviations in particle size are commercially available and even more monodisperse Au nanoparticles have been synthesized in the literature[69]. Accordingly, here I assume a gap spacing of 2 nm and gold nanosphere diameter of 23 nm and the diameter is kept constant for all the cases reported throughout the chapter. The permittivity of gold is taken from the experimental data provided in[70]. In our model I consider a rectangular silicon nitride waveguide with cross section of $1\mu m \times 0.5\mu m$ as in Fig. 2-1. Two types of the thin film models are considered in the following: (Case I) a uniform layer with thickness of 40 nm surrounds a dimer that is partially submerged as shown in Fig. 2-1(b) (left panel), and (Case II) a 30nm-thick whole layer together with a 2nm single-molecule layer covering the entire dimer surfaces as in Fig. 2-1(b) (right panel). Case I represents the case when the dimers are located in a small valley in the PMMA and then a thin layer of thioctic acid molecules is deposited partially filling the gap region. Case II evaluates the contribution of the thioctic acid monolayer on the nanosphere surface. The comparison of the two cases provides insight into the enhancement resulting from the PMMA and from the thioctic monolayer.

For simplicity, in both Cases I and II I consider an average dielectric constant of 2.47 to include the effect of the PMMA and the thioctic acid molecules. The chosen dielectric constant has proven to accurately reflect experimentally observed SERS enhancements in prior work[52]. Full-wave simulations are performed by the frequency domain finite elements method (FEM), implemented in the commercial software CST Microwave Studio by Computer Simulation Technology AG.

I define the field enhancement (FE) as

$$FE = |\mathbf{E}| / |\mathbf{E_0}|. \tag{2.1}$$

where $|\mathbf{E}|$ is the electric field magnitude at the center of the gold dimer gap and $|\mathbf{E_0}|$ is the electric field magnitude at the same location in the absence of the dimer nanoantenna. Fig. 2-2. shows the comparison of the E-field enhancement for Cases I and II illustrated in Fig. 2-1(b), while the waveguide is excited with its fundamental propagating mode (Mode 1 in Fig. 2-3.) in the frequency range from 400 THz to 620 THz. Note that in Fig. 2-2 (a) $|\mathbf{E}_0|$ in Eq. (2.1) is calculated when there is no dimer and no thin film (I have observed that a definition of $|\mathbf{E}_0|$ based on field evaluation considering the thin film and nodimer, would not alter the results). Maximum enhancements are 102 and 82 for Case I and Case II, respectively. In Fig. 2-2(b) I show how the field in the gap region is enhanced with respect to the field at the center of waveguide, where the modal field has its peak, for these cases (I) and (II). Our results show that the local field at the gap center is much larger (13.5 for Case I and 10.8 for Case II) than the field at the center of waveguide at resonance frequencies (504 THz in both cases).

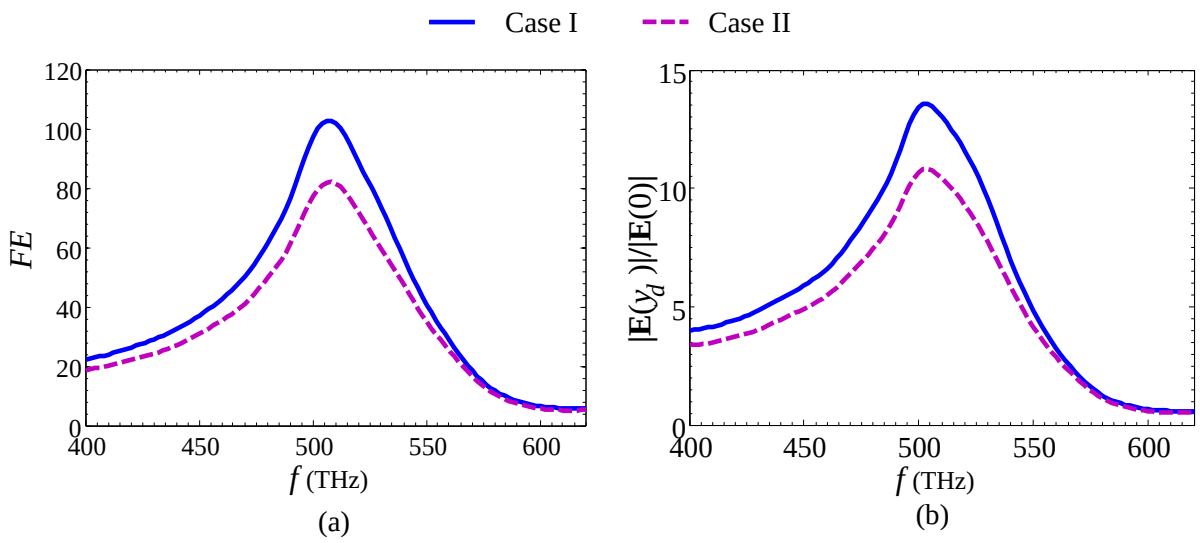

Fig. 2-2. (a) Field enhancement and (b) electric field at the dimer center (y_d = 286.5 nm) normalized to field at the waveguide center (y = 0), assuming the two different environments surrounding the plasmonic dimer nanoantenna: Cases I and II, with the thin film.

According to Fig. 2-2. the resonance frequencies, 504 THz, of the two proposed cases are the same, while Case I, gives higher electric field enhancement in comparison to Case II. The important physical difference between Case I and Case II, which affect the FE results, is the percentage of the gold dimer which is submerged in the thin layer with permittivity of 2.47. In Case I, the relative percentage submerged is larger than Case II. This is attributed to the local dielectric environment near the hotspot. In Case II, a single molecular layer with thickness of 2 nm covers the dimer and the gap between the nanospheres, the thickness of the thin layer leads to less field enhancement at the center in comparison to Case I that has a thicker dielectric layer. It is important to understand the dielectric environment can be used as a design parameter for optimizing spectroscopy integrated systems in addition to the geometric concepts proposed here.

As mentioned earlier, I consider a rectangular silicon nitride waveguide with cross section of $1\mu m \times 0.5\mu m$ .The waveguide dimensions are determined based on limits in conventional optical lithography features where $1\mu m$ is more or less the resolution limit due to optical diffraction limit of direct contact lithography[63], since our aim is not to rely solely on electron beam lithography which could achieve

smaller feature size. Because of silicon nitride dielectric density, the given waveguide hosts also higher order propagating modes (According to our simulations, the waveguide supports six propagating modes in the frequency range of 400-620 THz). A thinner waveguide would be easier to fabricate and provides stronger evanescent field compared to the reported case with 500 nm thickness, nonetheless it would suffer from larger loss. With the given dimer orientation (nanospheres aligned along the x-axis), a large field enhancement is achieved when the dimer is excited by horizontally polarized electric field[71], i.e., polarized along the *x*-direction, the dimer's axis. Therefore, I consider the first five propagating modes and I classify them as quasi TE and quasi TM modes shown in Fig. 2-3. Quasi TE modes have PEC symmetry (electric mirror symmetry) whereas quasi TM modes have PMC symmetry (magnetic mirror symmetry) where PEC and PMC stand for perfect electric and magnetic conductors. Fig. 2-3 shows FE in the frequency band from 470 THz to 520 THz when the waveguide is excited with the first five propagating modes, and the dimer is at x = 0 and at the height h = 25 nm from the waveguide surface, for the Case I illustrated in Fig. 2-1(b). The reported results shown in Fig. 2-3. demonstrate that for the first and the forth propagating modes (modes with strong electric field along the x-axis at the dimer location), the dimer resonates at 504 THz and leads to a FE level of approximately 102, whereas for the other modes whose their electric field does not have a horizontal component at the dimer gap, the FE is vanishing. From Fig. 2-3, I can infer that although the FE obtained for Mode 1 and Mode 4 is the same, the evanescent field of Mode 4 is much smaller than that of Mode 1 at the dimer location. Furthermore, here I assume that the dimer is placed at *x* = 0; if the dimer location changes horizontally along the *x*-direction, other modes also can create large field enhancement as examined in Fig. 2-8 (c-d).

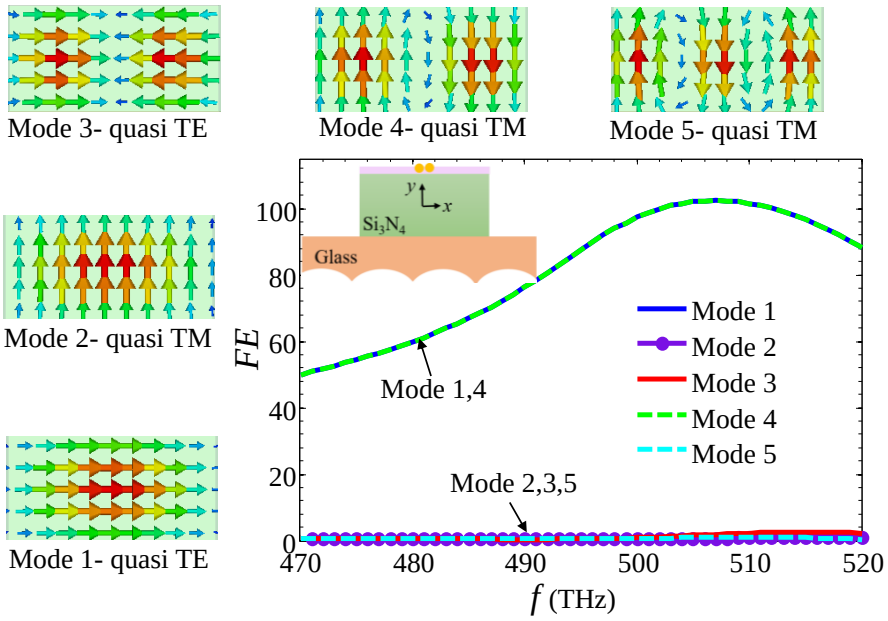

Fig. 2-3. First five propagating modes (quasi TE and quasi TM modes) in the silicon nitride waveguide, and field enhancement in the middle of the dimer (above the waveguide) for Case I as shown in Fig. 2-1(b) when each mode is individually excited.

In all the following full-wave simulation results, I assume the waveguide is excited only by its fundamental propagating mode (Mode 1 in Fig. 2-3.) with horizontal polarization. Fig. 2-4. shows the electric field localization for Case I of Fig. 2-1(b). by plotting the electric field magnitude maps, normalized to the electric field magnitude at every point, in the absence of dimer and thin layer, on the three orthogonal cross-sectional planes of the dimer. The E-field hot spot is localized mainly at the gap as expected, and the shape of the field profile between the nanospheres indicates the dipolar nature of the scattering from the nanospheres.

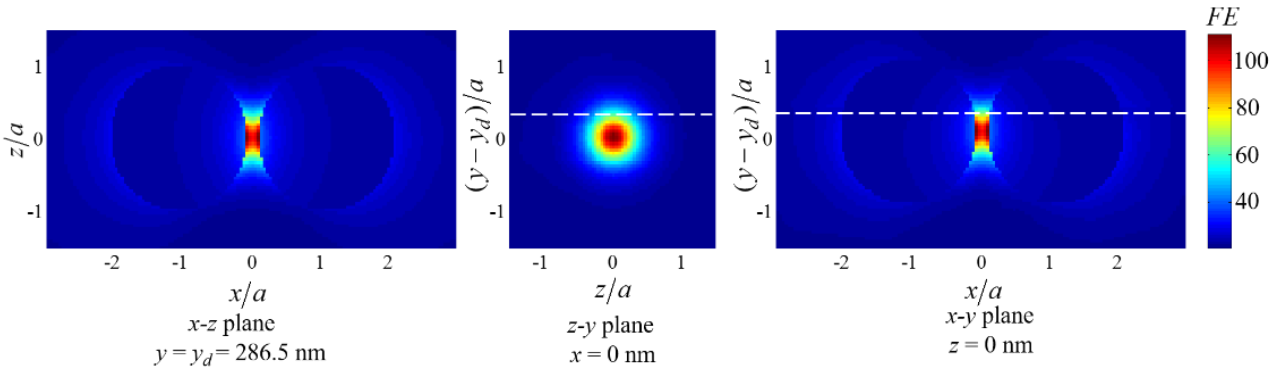

Fig. 2-4. E-field enhancement on three principal cross-sectional planes generated by the dimer nanoantenna Case I excited by the fundamental propagating mode of the integrated waveguide, at the dimer's resonance frequency of 504THz. Field has been normalized with respect to magnitude of electric field at each location in the absence of dimer and the thin layer, and the colors are linearly mapped as shown in the legend. The vertical distance of the dimer from the waveguide surface, h, is 25 nm. The white dashed lines for the two right figures, show the interface of the thin layer in Fig. 2-1. and vacuum. In the labels, "*a*" is the radius of nanosphere and "y_d "is the dimer's center location along the *y* axis.

The E-field enhancement profile $|\mathbf{E}(y)|/|\mathbf{E_0}(y)|$ along the y axis (vertical axis in the middle of the waveguide passing through the dimer's gap center) for Case I of Fig. 2-1(b) is reported in Fig. 2-5(a), when h is fixed at 25 nm (thus gap center is at yd = 286.5 nm) at 504 THz. Here $|\mathbf{E}(y)|$ and $|\mathbf{E_0}(y)|$ denote the magnitude of electric field, both as a function of vertical coordinate y, at the presence and absence of the nanoantenna and the thin layer, respectively. (I leave the *y* dependency in the formula to stress that $|\mathbf{E_0}(y)|$ also depends on vertical position for the analysis presented in Fig. 2-5(a) whereas in Fig. 2-5(b) $|\mathbf{E}(y)|$ is normalized with respect to $|\mathbf{E_0}(y=0)|$.) Fig. 2-5(a) provides the signature of the dimer near field that is characterized by a peak at the gap center. The zoom in the inset shows the actual peak width of few nanometers. The nanoantenna provides a strong enhancement of the field compared to the field at the same location without a nanontenna and the thin layer, but it is also interesting to observe how strong is the field in the nanoantenna gap when compared with the field guided by the waveguide reported in Fig. 2-5(b). Indeed, there I report the ratio $|\mathbf{E}(y)|/|\mathbf{E_0}(y=0)|$ defined as the magnitude of electric field along a scan line

coinciding with the y axis in presence of the nanoantenna, normalized by the electric field magnitude at the center of the waveguide (y = 0 nm) where the modal guided electric field is maximum.

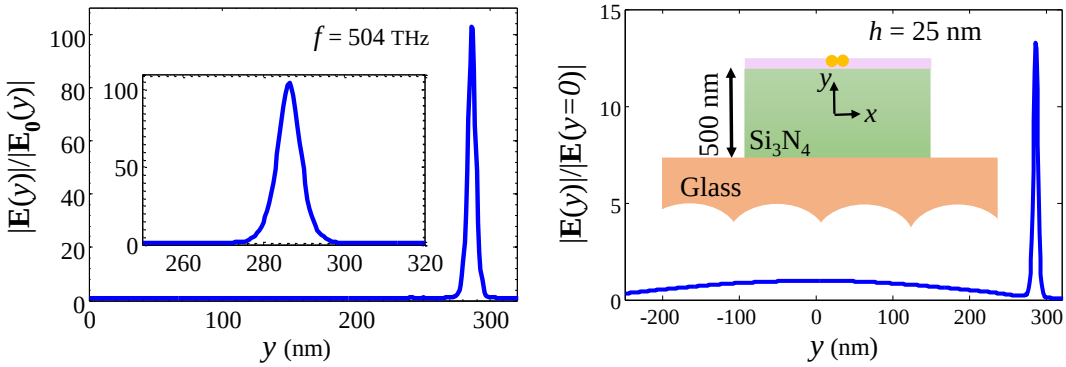

Fig. 2-5. (a) Field enhancement profile at 504 THz along the y axis, i.e. vertical line passing through the dimer gap center, for Case I. Here h = 25 nm, the dimer is centered at y = 286.5 nm where the sharp peak occurs. (b) Electric field profile, normalized by the electric field at the center of the waveguide (y = 0 nm) for the same case in (a) at 504 THz. Two things must be noticed: (i) The left plot (a) shows a strong field enhancement within the nanoantenna gap. This field enhancement will be affected if the material hosting the nanoantenna has a different dielectric constant, as shown next. (ii) The right panel (b) shows that the field within the nanoantenna gap is 13.5 times stronger than the electric field at the center of the waveguide.

The electric field at the dimer's gap center is 13.5 times stronger than the guided electric field at the waveguide center, hereby stressing that the resonant plasmonic dimer's near field, driven by the weaker evanescent field tail outside the waveguide, reaches even larger levels than the maximum of the guided field at the center.

Note that by invoking reciprocity, the field scattered by the dimer, when excited by an emitting molecule in the gap region, is efficiently coupled into the waveguide and the coupled electric field amplitude is over 13.5 of field at the emitted field in the dimer's gap. Note that this result pertains to the well confined field of Mode 1 of the waveguide (Fig. 2-3.).

Although the realistic case for putting gold nanoantenna on top of the waveguide is based on a colloidal assembly method, for the sake of understanding what contributes to the field enhancement I now study the effect of removing the thin dielectric layer, and varying the vertical position of dimer "*h*" on the

FE. Therefore in Fig. 2-6. I compare the FE results of Case I with h equals to 25 nm to the cases where I remove the thin dielectric layer (the thin purple layer in Fig. 2-1(b)) and the dimer is assumed to be located at various vertical distance from the waveguide surface, h, in the range from 0 nm to 25 nm while keeping the horizontal position of the dimer fixed above the center of the waveguide (x = 0 nm) and the gap spacing as 2 nm.

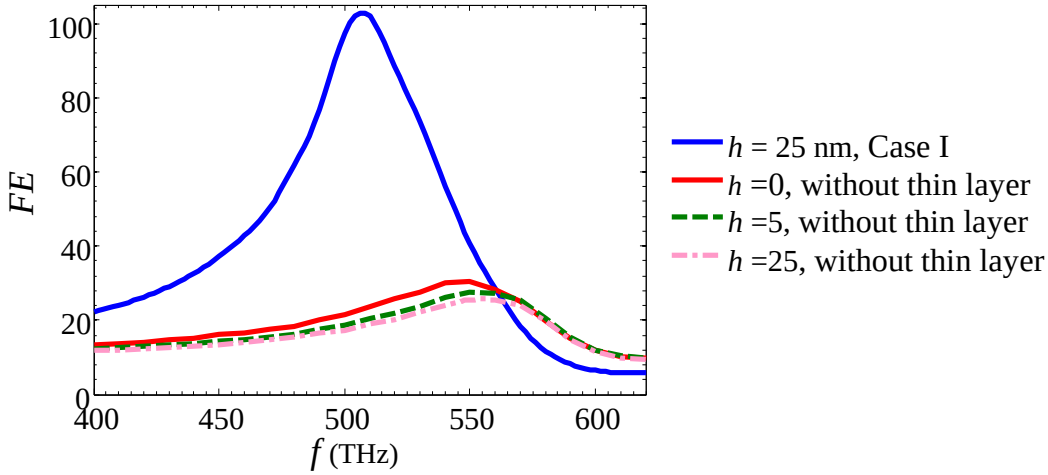

Fig. 2-6. Field enhancement versus frequency, with the thin layer (Case I) and without the thin dielectric layer for three vertical displacements h. Dimer is still above the center of the waveguide and the gap is 2 nm as in the previous figures.

It was reported in[51] that thioctic acid present in the gap increases the enhancement in surface enhanced Raman scattering measurements and leads to a redshift in the plasmon resonance due to the increased dielectric constant in the gap as compared to vacuum. According to Fig. 2-6. an average dielectric constant of 2.47 in the region between nanospheres due to PMMA environment and thioctic acid ligands on the dimer's surface (Case I), and the resulting dielectric contrast with respect to the surrounding vacuum, indeed leads to a red-shif in the plasmon resonance in comparison to the cases without the thin layer. The plasmon resonance is determined to be 504 THz for Case I and 549 THz, 550 THz, and 554 THz for the three cases without a thin dielectric layer, with varying distance from the surface (h equals to 0, 5, and 25 nm respectively). In absence of the thin dielectric layer, as h increases from 0 nm (dimer is in contact with the waveguide) to 25 nm (the same vertical location as Case I), the field enhancement drops monotonically

from 30.4 to 25.7, and the resonance frequency exhibits a small shift to higher frequencies. It is clear that there is only slight difference between the results of FE when h =0 nm (the dimer is on top of the waveguide) and h =25 nm in vacuum (the same dimer location as in Case I), where the main effect on FE is the local dielectric constant. As determined from simulations, the 40nm PS-b-PMMA copolymer template both leads to higher FE and a redshift of the plasmon resonance with all other physical results remaining similar. In order to minimize computation time and explore a larger range of experimental parameters, in all the following studies about the effect of waveguide size, gap between the nanospheres, position and orientations of the dimer, I consider the dimer at h = 25 nm above the waveguide to be consistent with the vertical position of the experimental case (Case I) and I remove the thin layer to avoid the cost in computation time associated with the need to finely mesh the thin film to get accurate numerical results. The trends will be analogous to the Case I with thin layer shown in Fig. 2-1(b). Our goal is to show for the first time that this integrated technology is feasible for SERS and fluorescence spectroscopy as it generates the necessary field enhancement. One can only expect higher FE when incorporating the thin film in the experimental system.

As mentioned above, I consider our waveguide dimension as $1\mu m \times 0.5\mu m$. The fabrication geometry is adopted from an experimental demonstration[63] with gold colloidal assembly for nonlinearity enhancement. The effect of changing the waveguide dimension on FE is shown in Fig. 2-7. In each case I assume the waveguide to be excited by only its first propagating mode which has a profile as shown in Fig. 2-3, Mode 1. In all cases, the vertical distance of dimer and waveguide surface (h) and the gap between the nanoantennas are kept constant (h = 25 nm and gap = 2 nm respectively) and I do not consider the thin layer for simplicity. Reducing the waveguide dimensions will indeed enhance the evanescent field and facilitate the delivery of power to the nanoantennas, however according to the results of Fig. 2-7, the FE as an antenna property which is the ratio of two electric fields, remained constant. Since FE is an antenna property as the result shows, I do not expect any significant FE change also for other small variations of the waveguide dimensions.

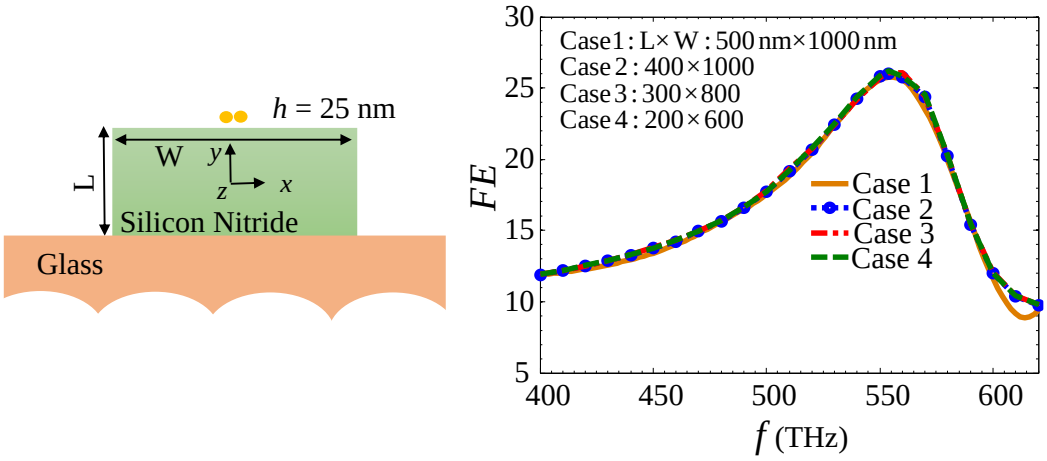

Fig. 2-7. FE for various waveguide cross sectional dimensions when the waveguide is excited with its first propagating mode. In all cases h = 25 nm and gap = 2 nm.

Until this point, I have simulated the case where a dimer nanoantenna is located exactly above the top center of the waveguide ($x = 0$) and the dimer's gap is 2 nm, however in experimental systems based on colloidal deposition, dimers may be located at various places across the waveguide surface with potentially varying gap spacings. Therefore, in the following analysis, I report the field enhancement, FE, versus frequency for various horizontal x-positions of the dimer and having different gap spacing in Figs. 2-8 and 2-9, respectively. Fig. 2-8(a) shows the FE versus frequency from 400 to 620 THz when h and the gap are fixed at 25 nm and 2 nm and the dimer's horizontal position is varied, with the center of the dimer located at $x = 0$ (the center of the waveguide), 100, 200, and 400 nm, keeping in mind that the waveguide terminates at x =500 nm; furthermore there is no thin dielectric layer and the waveguide is excited with its first propagating mode. Results in Fig. 2-8(a) show that when the waveguide is excited with its first propagating mode, the horizontal position of the dimer has negligible impact on the field enhancement level and the resonance frequency except for the position at x = 400 nm, i.e. where the dimer is closest to the edge of the waveguide. At the edge there is a slight decrease in enhancement level and a small increase in the resonant frequency. Fig. 2-8(b) shows the E-field enhancement profile $\left(|\mathbf{E}|/\overline{|\mathbf{E_0}(y=250)|}\right)$, in which $|\mathbf{E}|$ is the magnitude of electric field at the dimer gap and $\overline{|\mathbf{E_0}(y=250)|}$ is the average of magnitude of electric field

in the absence of dimer at the waveguide surface (the waveguide surface is at y = 250 nm), versus dimer's horizontal *x*-position when the waveguide is excited with its first propagating mode at the resonance frequency of 554 THz. As Fig. 2-8(b) represents, the best location for dimer is exactly above the center of waveguide, where according to the profile of mode 1, in Fig. 2-3., the electric field has its maximum *x*-component, and by increasing the distance of the dimer from $x = 0$, the E-field enhancement decreases. Fig. 2-8 (c-d), represent the FE for different dimer locations along the *x*-direction, assuming also higher order modes are present in the waveguide. Fig. 2-8(c) and 2-8(d) show the FE versus frequency from 540 to 570 THz for different horizontal dimer locations along the *x*-axis, $x = 200$ nm and $x = 400$ nm respectively, while the waveguide is selectively excited with its first five propagating modes and $h = 25$ nm and the gap is 2 nm. I expect that when the dimer is placed at a location with electric field polarized along the dimer gap, I get considerable field enhancement. According to Fig. 2-8(c) and 2-8(d), when I change the horizontal position of dimer, and excite the waveguide with its higher order modes, at locations that the electric field has an *x*-component (1^{st}, 3^{rd}, and 5^{th} mode for the $x = 200$ nm case and 1^{st} and 3^{th} mode for the $x = 400$ nm case), I have as strong FE as I can get only with the first propagating mode.

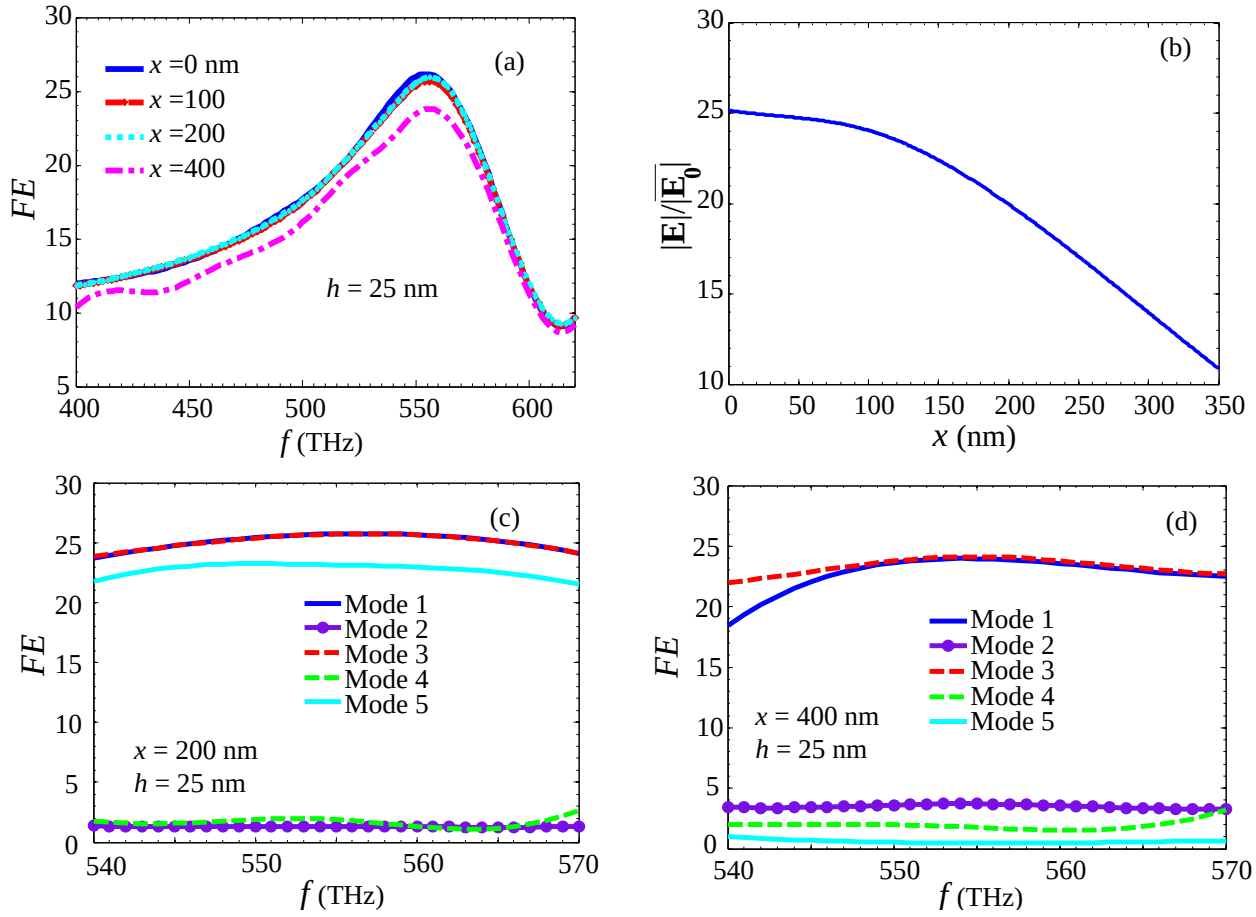

Fig. 2-8. Field enhancement in the absence of the thin dielectric layer (a) for various horizontal positions of the dimer versus frequency when h = 25 nm and the gap is 2 nm are kept constant. (b) Electric field profile at the dimer gap normalized to the average electric field at the waveguide surface (y = 250 nm), for various dimer's horizontal positions along x-axis at 554 THz when h = 25 nm and the gap is 2 nm are kept constant. FE (c) for dimer's horizontal position x = 200 nm and (d) for position t x = 400 nm, versus frequency when h = 25 nm and the gap is 2 nm are kept constant and the waveguide is selectively excited by the waveguide's higher order propagating modes.

In Fig. 2-9. FE versus frequency is reported for different gap sizes (2, 4, 6 and 10 nm). This figure shows that the highest field enhancement is obtained in case of a 2 nm gap. Increasing the gap size shifts the resonance frequency slightly (554, 565,567 and 567 THz for the gap size of 2, 4, 6 and 10 nm, respectively). As it can be noticed from results in Fig. 2-6., Fig. 2-8. and Fig. 2-9., the most critical parameter for FE is the gap size.

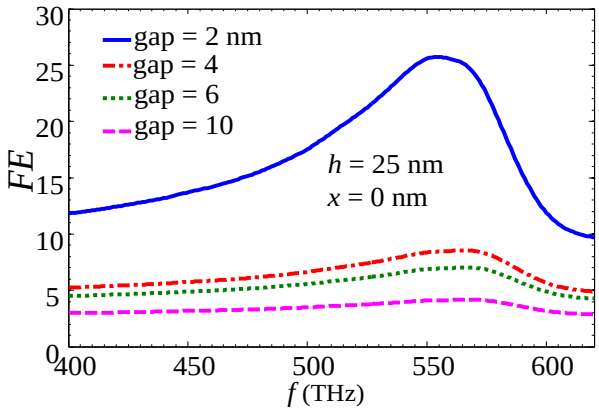

Fig. 2-9. Field enhancement versus frequency for various gap sizes when the dimer is located at h=25 nm and $x=0$, and there is no dielectric thin layer.

Depending on the procedure for depositing dimers on the waveguide surface, one does not have complete control on the orientation of the dimer axis on the x-z plane. Thus in Fig. 2-10 (a-d), I investigate the effect of different dimer orientations (90, 60, 30, and 0 degrees with respect to the z-axis along the waveguide, respectively) on the field enhancements when h is 25 nm and the dimer is centered at x = 0. I assume that the first five propagating modes are present in the waveguide and I do not consider the thin dielectric layer. In the right panel of Fig. 2-10, the E-field profile in the x-z plane at the dimer location (h = 25 nm) at 554 THz is shown for the first five propagating modes. As expected, FE increases when the electric field of waveguide propagating mode is completely polarized along the dimer axis. In agreement with the E-field profile, when $\theta = 90^\circ$ (Fig. 2-10(a), for dimer axis along x), Mode 1 and Mode 4 are completely polarized along x- axis at the dimer location, hence they generate the strongest FE. Whereas for $\theta = 0^\circ$ (Fig. 2-10(d), the dimer axis is along z), Mode 3 is completely polarized along this dimer's axis and generate the strongest FE. Note that the peaks are at the same frequency determined by the dimer's resonance.

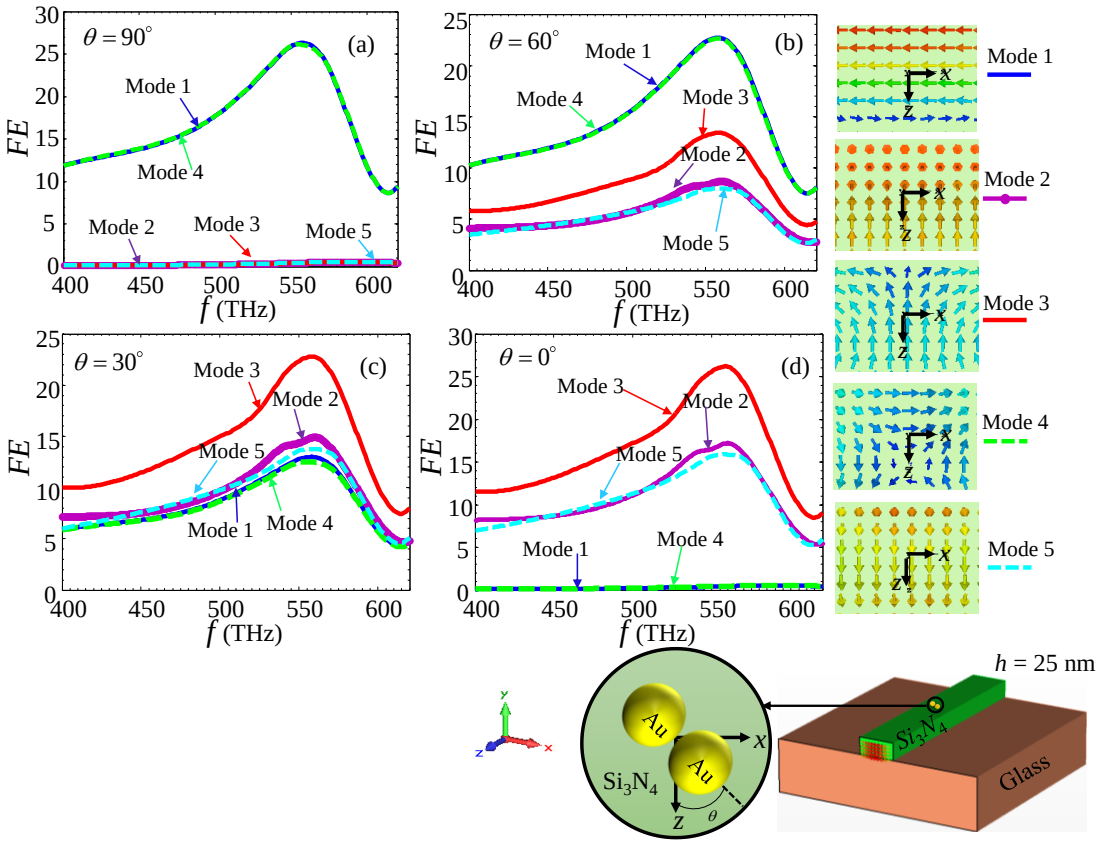

Fig. 2-10. FE for different dimer orientations with respect to the waveguide longitudinal axis *z* (a) 90 degrees, (b) 60 degrees, (c) 30 degrees and (d) 0 degrees, considering the waveguide's first 5 propagating modes. The E-field profile in the *x*-*z* plane at the dimer location (h = 25 nm and dimer centered at x = 0) at 554 THz is shown in the right side.

As mentioned in the Introduction, in a colloidal assembly deposition procedure, nanoantennas are randomly deposited on top of the waveguide surface. Also, in all the cases I study, I consider that the density of nanoantennas are low and they are separated from each other with enough distance to neglect the coupling effect between the studied dimer and other surrounded nanoantennas. Here to study the coupling effect, I consider some cases which consist of existence of other nanoantennas (monomer and dimer) at different distances and orientations from our main dimer in the absence of the thin dielectric layer and h=25nm. Their coupling effect on field enhancement is shown in Fig. 2-11. In Fig. 2-11(a) the effect of the coupling between the considered dimer and another one at a given distance in the *x*-direction is shown, considering distances of 5 nm (Case 2) and 50 nm (Case 3), compared to the case of isolated dimer (Case 1). For Case

3 the FE is basically equal to that for Case 1, indicating that a distance of 50 nm is already large enough to neglect coupling (50 nm is approximately $\lambda/10$ where λ is the wavelength of resonance frequency 554 THz of a dimer). For Case 2, coupling causes a larger FE than the isolated dimer (Case 1). Indeed, for Case 2 the other dimer is at a very short distance, comparable with the dimer's gap. For a distance of 5 nm, which is approximately $\lambda/100$, the coupling effect exists and cannot be avoided, however for the studied case it generates larger enhancement. However, the possibility of having another nanoantenna very close to our dimer is very low according to the assumption of low density of nanoantennas. Previous work on particle assembly demonstrates that cluster surface coverage exceeding 40% are not physically achievable using the assembly method[52] but still large SERS is experimentally observed.

There are many possible coupling scenarios, and here I consider three other cases in Fig. 2-11 (b) with different distances and orientations of a monomer from the considered dimer, all compared to Case 1, the isolated dimer. Case 2 and Case 3 show a small increase of FE, that is consistent with the results in[51]–[53] for trimers, that show larger enhancement compared to dimers. Case 4 in Fig. 2-11(b) represents monomer nanoantenna with an orthogonal orientation with the considered dimer, and even at such small distance, the coupling effect is negligible.

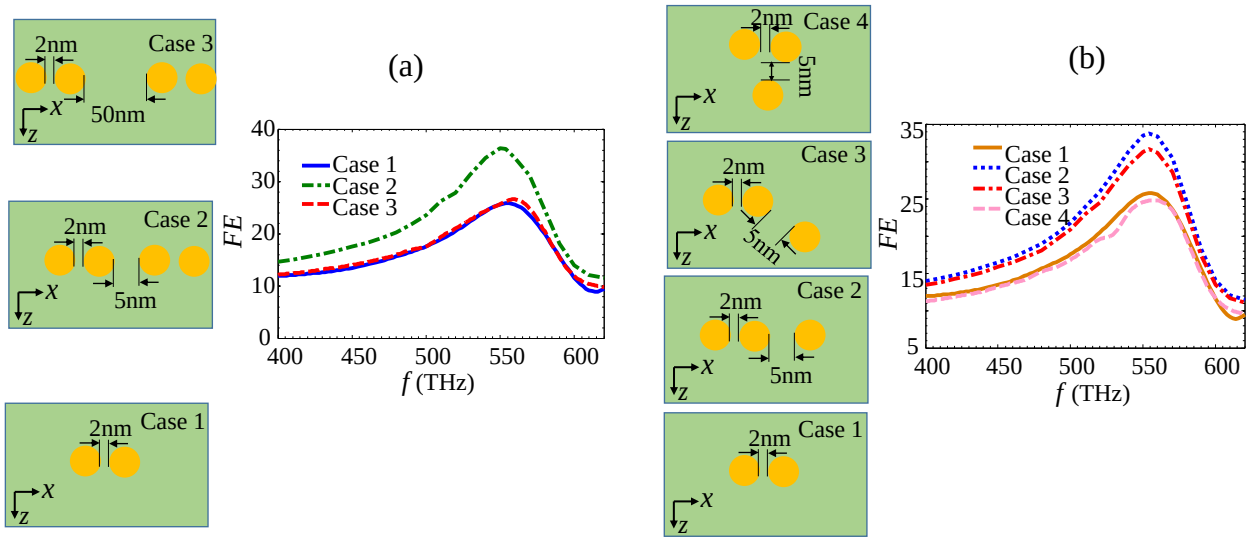

Fig. 2-11. Top view of different nanoantenna distributions on top of waveguide surfaces in the absence of thin dielectric layer is illustrated. I study the effect of coupling between nanoantennas on FE with respect to the case with

an isolated dimer nanoantenna. (a) Effect of distance on coupling between two dimers; (b) effect of orientation on coupling between dimer and monomer.

Sec. 2.3 Comparison with field enhancement by a nanoantenna excited by a plane wave

The proposed waveguide scenario for field enhancement is compared with the traditional one where nanoantennas on a surface are excited by an external beam. In [51], field enhancement resulting from various oligomer geometries of gold nanospheres, including dimers, were investigated on top of layered structure illuminated by an external plane wave. Here, I take the same vertical stack of materials and the dimer nanoantenna as in Section 2.2 and compare the field enhancement in the layered structure under a plane wave illumination from[51] and [72]–[74] with the waveguide-driven nanoantenna topology similar to that in Fig. 2-1. In Fig. 2-12. the simulated multilayer structure composed of (from bottom to up) glass, silicon nitride and vacuum is illustrated. The vertical distance between the bottom of the spheres and the top of the silicon nitride layer is denoted by *h* and the definition of the "gap" is the same as that in Section 2, shown in Fig. 2-12. The silicon nitride layer thickness is $0.5\mu m$, i.e. equal to the waveguide thickness in Section 2. The two gold nanospheres have constant diameter and gap distance as those in Section 2 (23 nm and 2 nm, respectively). The polarization of normally incident wave is along the *x* direction as shown in Fig. 2-12. The normal plane wave incidence is simulated assuming plane wave excitation on a multilayer structure with size of $3\mu m \times 3\mu m$ in *x-y* plane ($3\mu m$ is 4 times of wavelength at 400 THz), and $1.5\mu m$ for glass thickness, and applying the software's "open boundary condition". In Fig. 2-12, I report the field enhancement for various *h* (0 nm, 5 nm and 25 nm) versus frequency ranging from 400 to 620 THz. Our simulation results show that by increasing the distance *h*, the resonance frequency slightly shifts to higher frequencies and field enhancement decreases monotonically, with enhancement levels dropping from 30 to 25. Here it is stressed that similar trends of enhancement levels and resonance frequencies are obtained in Fig. 2-6 for the waveguide-driven nanoantenna topology without considering the thin dielectric layer. Our simulation results for FE are in agreement with the findings in[51]. However, there is a main differences

between the interaction scenario in Fig. 2-1 and the more traditional one in[51] and in previous related work. Here instead of having a nanoantenna excited by an external light beam and its scattering collected by a lens with large numerical aperture which causes an expensive and bulky setup, I propose to have nanoantennas integrated with a silicon nitride waveguide, so I can excite the nanoantenna with an evanescent field from the waveguide and as a result our proposed structure may have advantages in terms of cost, integrability and volume occupancy.

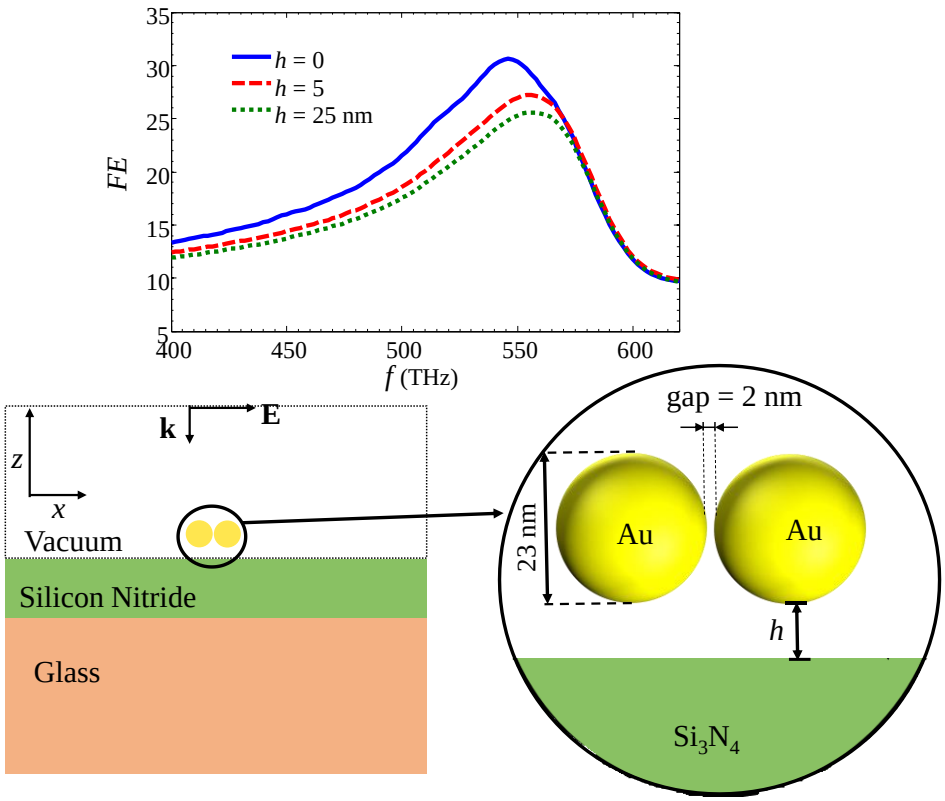

Fig. 2-12. Topology of a nanoantenna on top of a multilayer structure excited by a normally incident plane wave, and plot of field enhancement versus frequency for h = 0, 5, 25 nm, using the same gold nanosphere diameter and gap as in the waveguide-driven structure reported in Section 2.

Next, I assess the impact of the dielectric thin film as in Section 2. and I consider two types of the thin film formation cases as in Fig. 2-1. but considering plane wave excitation as in Fig. 2-12. In Fig. 2-13. I report the results for Cases I and II with the thin film and for the case without the thin dielectric film over the surface (but still with h = 25 nm) for both the waveguide-driven nanoantenna (solid curves) and the

plane wave driven multilayer topologies (dashed curves). I observe that in all the cases, with and without the thin film both waveguide-driven and the plane wave driven structures provide the same field enhancement. On the other hand, when considering the cases with the thin film both waveguide-driven structure and the plane wave driven structure provide stronger field enhancement (102 and 82 for Case I and Case II, respectively). For both cases, the waveguide and plane wave driven structures, when the thin films are taken into account, the resonance frequency of the dimers shift to lower frequencies. Overall the waveguide-driven nanoantennas are able to provide similar trends and electric field enhancement, FE, levels to the plane wave driven structures.

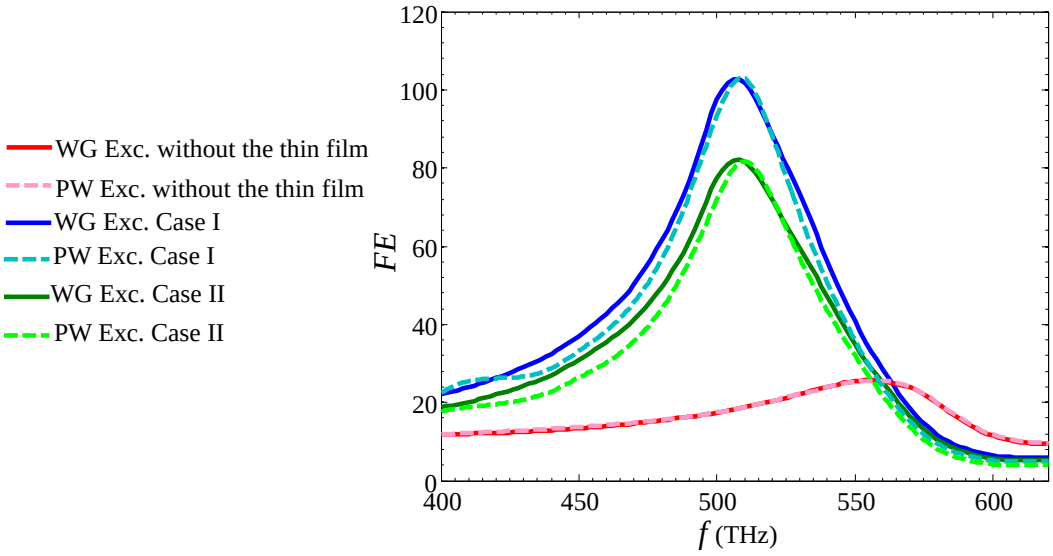

Fig. 2-13. Comparison of field enhancement for different structures with two kinds of excitation (Exc.). I compare the field enhancement of the waveguide (WG) based topology in Fig. 2-1. with the more traditional one, the plane wave (PW) illumination. Results of both topologies are in strong agreement. Furthermore, in both topologies the thin dielectric film results in stronger field enhancement and in an expected red-shift of the resonance frequency.

Sec. 2.4 Conclusion

In this chapter I have proposed a configuration that provides strong electric field enhancement by placing colloidal plasmonic dimer nanoantennas on top of an integrated silicon nitride waveguide. I also considered the effect of a layer of PMMA and thioctic acid molecules which has been used previously for

fabrication of dimers assembled from colloidal solution. It is significant that the presence of this polymer film results in an even stronger field enhancement due to an increase in dielectric constant. The results presented here demonstrate that a CMOS compatible waveguide geometry can yield strong field enhancement when inexpensive and chemically driven fabrication processes are adopted. While I consider only the excitation of colloidal nanoantennas in this chapter, the results imply that scattering process by molecules in the nanoantenna gap would also generate the excitation of guided modes that can be eventually detected in silicon technology. Field enhancement of the proposed waveguide topology is analogous to that obtained with the more traditional open space topology with an external beam, with the advantage of integrability and size reduction for possible future economical integrated spectrometer systems.

CHAPTER 3 : ENABLING INTEGRATED SURFACE ENHANCED RAMAN SPECTROSCOPY WITH SILICON NITRIDE WAVEGUIDE

Sec. 3.1 Motivation

As was discussed in the last chapter, in an standard SERS experiment, SERS substrate is excited by laser and the spectra is collected by an objective lens. However, due to the nature of the excitation and collection of signals in these structures, they can't be integrated on a device and thus are not suitable for massive fabrication for sensory applications. This limitation calls for alternative methods for exciting and collecting the spectra of SERS signal.

Recently hybrid structures which combine the capabilities of photonic waveguides and plasmonic structures have received a great deal of interest [19–22]. Indeed, this type of technology enables integration of plasmonic structures with various optical functionalities into optical waveguides and thus provides the opportunity for miniaturization and massive fabrication through CMOS-compatible foundry fabrication process with silicon-on-insulator (SOI) platform [23]. Recently, the technology based on silicon nitride (Si3N4) has been brought up as an alternative to SOI silicon platform for photonic integrated circuits (PICs) due to its lower cost of fabrication and lower loss [24,25]. Therefore, it would be an ideal solution to combine the plasmonic particles needed for SERS with CMOS-compatible technology of optical waveguides to enable integration of various sensors in portable devices.

Sec. 3.2 Objective and operational principle

In this chapter, I propose an integrated structure that consists of oligomers of colloidal plasmonic nanospheres on top of a silicon nitride waveguide. The analytes are placed at the hotspot of oligomers who are excited by the evanescent wave of a Si_3N_4 waveguide. The Raman signal scattered from the analytes is

then coupled back to the waveguide and is collected at its end. I compare this structure with standard SERS substrate (in which substrate is excited by laser and the spectra is collected by an objective lens) for exciting the analytes and collecting the SERS spectra. The optical properties of oligomers, such as resonance wavelength and enhancement factor of electric field, are highly dependent on geometry and the type of metal and will be studied thoroughly here.

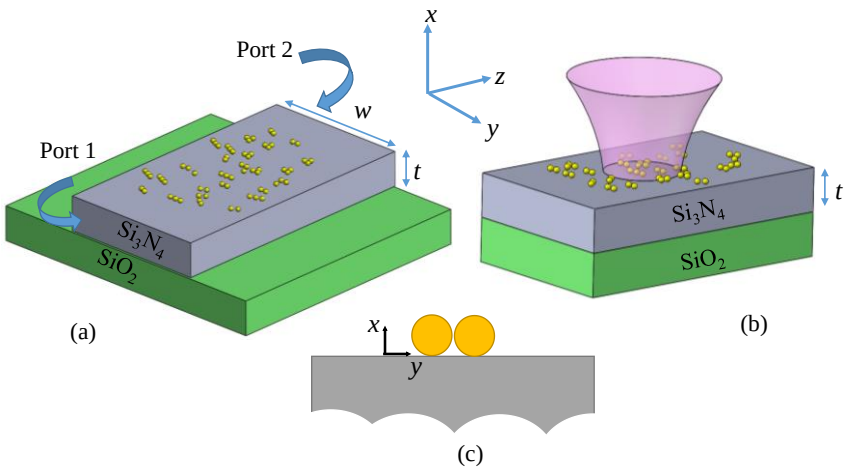

Fig. 3-1.(a) Proposed integrated structure for SERS which consists of Si3N4 waveguide and the plasmonic oligomers above it. The power is injected from port 1 and the SERS spectra is collected at the other port (b) Standard SERS structure in which the nanoantennas are excited from above and the SERS spectra is collected by objective lens (not shown in this figure). (c) Sideview of a gold dimer, as an example of oligomers on top of Si3N4 waveguide or a substrate.

Fig. 3-1 (a) shows a sketch of the integrated SERS substrate made of a Si_3N_4 waveguide. The single mode waveguide is excited at port 1 and plasmonic nanoantennas are over the middle part of the waveguide. The evanescent wave outside the waveguide excites the plasmonics nanoantennas which in turn enhance the field at the hotspots in the gaps of the plasmonics nanoantenna (where the analytes are present). The enhanced Raman signal scattered from the analytes is coupled back to the waveguide via the same mechanism and is collected at port 2 of the waveguide. The oligomer excitation depends on the polarization of the evanescent field, which in this case is assumed to be along the *y*-axis because of the *y*-polarized single mode excited in the dielectric waveguide. Here, as an example, I assume to have a linear oligomer oriented

along the *y*-axis, so that its polarizability matches the polarization of the evanescent field just outside the waveguide. Indeed, my proposed platform makes use of the strong evanescent field on the surface of the waveguide to efficiently excite and collect Raman scattering of analytes. Fig. 3-1 (b) shows a standard SERS substrate which consists of plasmonic nanoantennas over a substrate made of Si_3N_4 and silica (SiO_2), for ease of comparison excited from above. In this standard configuration, Raman signal is collected by an objective lens above the substrate. The bigger the numerical aperture of the objective lens, the higher the amount of Raman signal collected by it. It should be noted that in Raman spectroscopy the excitation and emission frequencies occur at different frequencies, and it is best to have strong field enhancement at both excitation and scattering frequencies. Therefore, in the following, I design the nanoantennas such that they provide strong field enhancement over a relatively wide frequency band. Furthermore, in all the results, I assume the width and thickness of the silicon nitride waveguide to be w =600 nm and t =200 nm, respectively, to have a single mode waveguide with its fundamental mode polarized parallel to the oligomer's axis (the *y*-axis in Fig.3-1). The thickness of the silicon nitride in the SERS substrate is assumed to be t=200 nm throughout the chapter. It's worth mentioning that although silica can be used alone as the standard Raman substrate, here for the sake of comparison with the proposed waveguide structure, I assumed Si_3N_4 is deposited over silica.

In my investigations, I aim to compare the detection ability of the waveguide structure with colloidal nanoantennas with that of planar SERS substrate with top excitation using two figure of merits. Raman signal is proportional to the fourth power of the electric field hence having strong field at the location of analytes (i.e. gap of the oligomers) greatly enhances the emitted Raman signal. Thus, I will compare the electric field in the gap of the oligomers for both structures. On the other hand, collecting the maximum amount of Raman signal emitted by analytes is of high interest. Therefore, I will compare the ability of both structures in collecting the emitted Raman signal from analytes. Without loss of generality, throughout this chapter, I use dimers as nanoantennas with nanospheres having 40 nm radius and 2nm gap. As described

before, this sub nanometer gap is made possible using electrohydrodynamic flow and chemical crosslinking [16]. I have designed the size and the gap between nanoantennas such that the field enhancement (due to plasmonic resonance) is strong between the excitation frequency (785 nm) and scattering frequency (for example at 897 nm) of standard SERS analyte like benzenethiol (BZT). It is noteworthy to mention that majority of oligomers have a resonance near the ones of linear dimers and trimers [16]. In particular, I compare the electric field enhancement at the hot-spot of a dimer, i.e., in the middle of the gap when this is placed, : 1) on top of the proposed waveguide excited through Port 1 (left port in Fig. 3-1) with 100 µW power; 2) on top of a substrate excited through a Gaussian beam propagating down (in the *x* direction) with half-waste parameter w_0=250 nm and 100 µW power. Numerical simulations are carried out using the finite element method implemented in CST Studio Suite. In Fig.3-2 (a), I have shown the full-wave simulation results of the electric field in the hot-spot of a dimer (between two adjacent nanospheres as shown in the figure with red dot) for both cases versus the excitation wavelength (note that the field for standard SERS substrate is multiplied by 10). As one infers, the field level obtained with the excited waveguide structure is almost 15 times stronger than the one relative to the beam excitation of a standard substrate (using the same power in both cases). This means that our proposed structure provides significantly higher electric field compared to the standard SERS substrate. Since this enhancement at the hot-spot of dimer occurs also in the scattering process, we expect to have an overall 15^4 increase in SERS signal. Indeed, to quantify precisely the field enhancement in both structures, I use the electric field enhancement which was defined in Eq. (2.1). The geometry of the nanoantenna is the same as Fig. 3-2 (a). As one can observe from the results, I almost get the same value for field enhancement for both cases, the field enhancement is a feature of the nanoantenna and not the structure surrounding it or the exciting wave. Based on this result, the waveguide structure can provide the same field enhancement (which is vital to SERS) as the standard SERS substrate. It is worth mentioning that the length of the waveguide doesn't play

a role since in this first simulations aiming at showing the main concepts I neglect scattering or dissipation losses in the waveguide that however are in general not high.

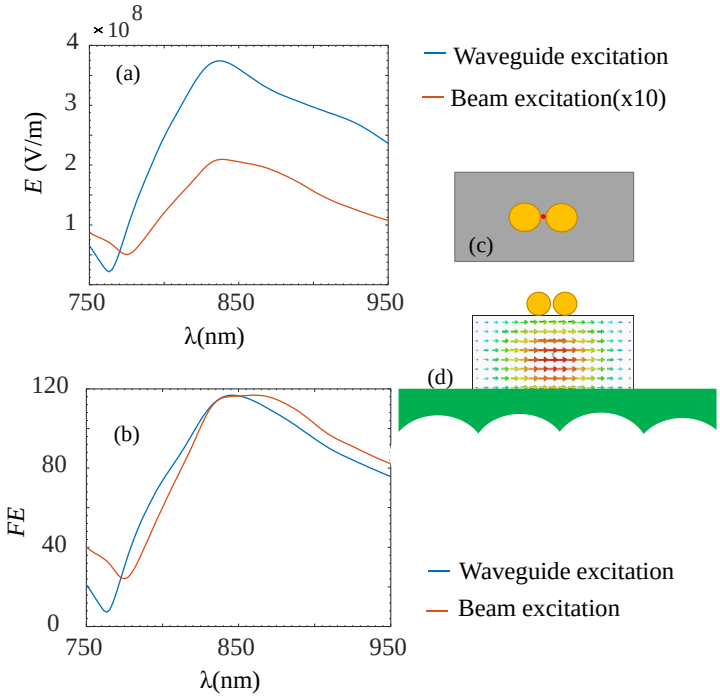

Fig. 3-2. Electric field available (a) and field enhancement (b) at the hot-spot of dimer (shown with red dot in (c)) for both beam (standard SERS) and waveguide (proposed structure) excitations. (c) and (d) show the top and front view of the dimer on top of the waveguide structure, respectively. The fundamental mode of waveguide at its port is shown in (d). Note that I designed the nanoantenna system such that the field enhancement is strong in a range between the excitation and scattering wavelength of standard SERS analyte BZT. The important result of this figure is that field enhancement is a feature of nanoantenna not its surrounding structure.

As mentioned earlier, the other important point to investigate is comparing ability of the waveguide structure in collecting the Raman signal with that of a standard SERS experiment with top collection with an objective lens. Indeed, I need to make sure that the collected Raman signal at the other port of the waveguide is strong enough for detection. Thus, I compare the collected Raman signal by the waveguide and the one collected by an objective lens with numerical aperture NA = 0.9 (to model such a numerical aperture in full-wave simulations, I integrate the power over a circular surface with a specific distance from the top of the waveguide). To that end, I calculate the collected power emitted from a horizontal elementary

Hertzian dipole oriented along the *y* direction with dipole moment p = 1 Am radiating at the hotspot of the dimer (this unit is often used in antenna engineering and it is used in the commercial software CST). However, for the moment, I assume the dimer is not present. The dipole is modeling the scattering source in an analyte molecule via Raman mechanism. Fig. 3-3 demonstrates the collected power for both structures versus the wavelength of the dipole source (P_{obj} and P_{port} are both normalized to their respective maxima in the observed wavelength range). Based on full-wave simulation results, the ratio of the collected power at the waveguide port to the collected power by objective lens for λ = 897 nm (scattering wavelength of BZT [26]) is 0.75. Although the collected power by the objective lens is slightly higher for the same dipole scatterer, since the achievable electric field is much stronger for our proposed integrated structure (as Fig. 3-2 (a) demonstrates), our Raman spectroscopy platform has better overall performance. Indeed, as was mentioned in the introduction, the goal of using a waveguide structure is not increasing the sensitivity of Raman spectroscopy system but to enable the integration of such a system in a CMOS-compatible structure. It's crucial mentioning that since the interaction the evanescent wave with analytes takes place over the whole length of the waveguide, the proposed waveguide setup could provide even stronger signal than the standard SERS substrate in which the interaction area is limited to the objective lens focus.

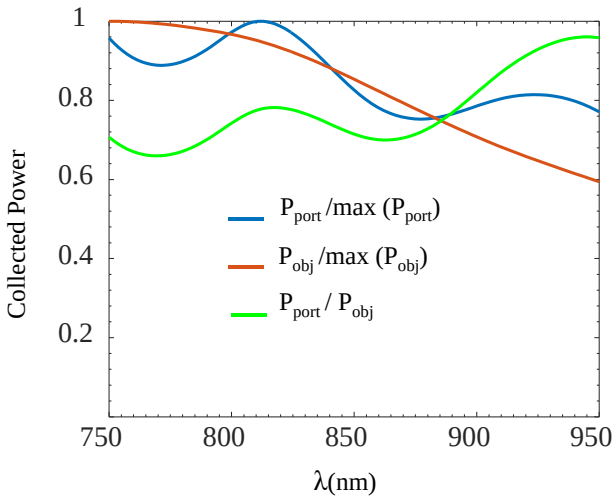

Fig. 3-3. Normalized collected power generated by an elementary Hertzian dipole from a dipole in the hot-spot of a dimer versus wavelength for waveguide structure and standard SERS substrate in the absence of dimer. For each case the

collected power is normalized to its maximum value. The ratio of waveguide to standard SERS substrate collected power (without normalization) is shown in green.

So far, in our simulations for the waveguide structure in Fig. 3-3, I have assumed that the dipole to mock-up the analytes molecule is located exactly above the top center of the waveguide (y = 0) along the y direction. However, in SERS experimental systems analytes molecules may be located at various spots across the waveguide surface. They may also get polarized in different directions, based on the orientation of the nanoantenna that they are in between. Here I report the effect of the orientation and y position of a dipole on the collected power at Port 2. To that end, we define *d* as the offset, i.e., the distance between the center of the waveguide and the location of the dipole and θ as the angle between z-axis and the axis of the dipole.

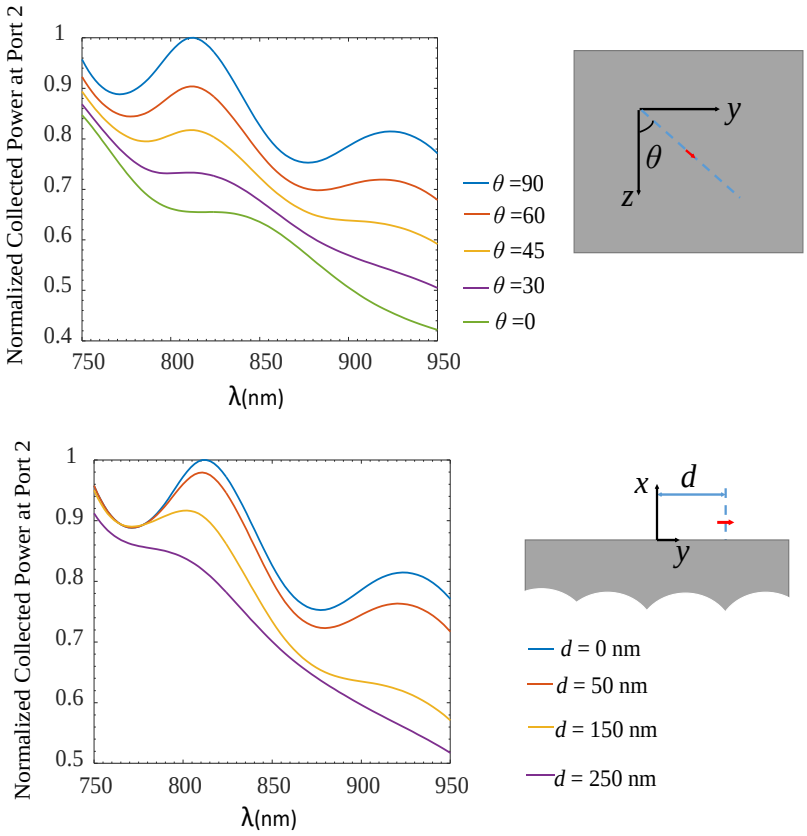

Fig. 3-4. Collected power at port 2 of the integrated SERS waveguide for (a) various orientation angles from the y-axis normalized to maximum collected power when θ=90 (b) various horizontal positions of the dimer versus frequency normalized to maximum of the case with *d*=0 nm (b).

The effect of orientation of a dipole around *y*-axis is shown in Fig. 3-4 (a) (the results are normalized to the maximum of θ=90° case). As one observes, the collected power at port 2 drops as θ decreases. To clarify this result, we note that the electric field of the fundamental mode of the waveguide is polarized along the *y*-axis. When the dipole is along the *y*-axis, the coupling of its emitted wave to the fundamental mode is strong and as it rotates, the coupling decreases. Fig. 3-4 (b) illustrates the collected power at port 2 for varying values of *d* versus wavelength. The power in each case is normalized to the maximum of power for *d*=0 case, i.e. dipole on top of the center of the waveguide. As demonstrated, as the dipole gets farther from the center of the waveguide, the collected power at port 2 diminishes since the coupling to the fundamental mode of the waveguide weakens.

Lastly, it is worth looking at collected power at the waveguide port and objective lens, when the dipole is located at the hot spot of dimer nanoantenna, to mock-up the Raman scattering phenomenon of an analyte molecule in the SERS experiment. Fig. 3-5 compares the normalized collected power at port 2 and objective lens in the presence of the dimer (dipole is located in the hot spot of a dimer with geometry as of Fig 3-2). A very important observation is that the reciprocity theorem holds for both schemes, meaning, the excitation and scattering for both the waveguide and objective lens structures, follow the same trend. Indeed, for the waveguide structure, maximum of both excitation and scattering happens around 830nm while this maximum occurs at 850 for the objective lens scheme.

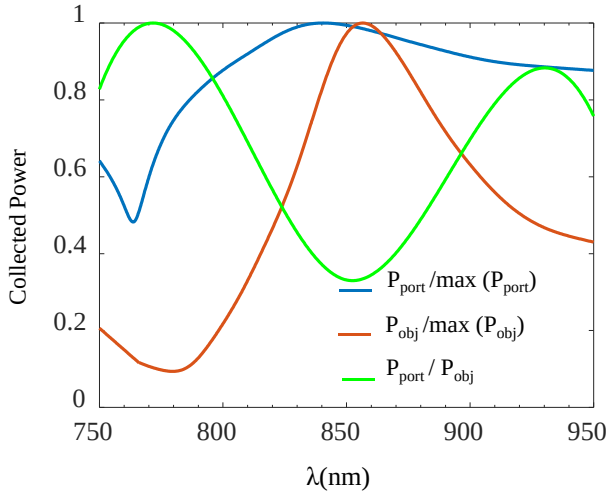

Fig. 3-5. Normalized collected power, generated by an elementary Hertzian dipole in the hot-spot of a dimer versus wavelength for the waveguide structure and the standard SERS substrate in the presence of the dimer.

Sec. 3.3 Conclusion

In conclusion, I have shown the functionality of an integrated SERS platform using a single-mode Si_3N_4 waveguide and investigated how its performance compares to the that of standard SERS substrate. I compared the field in the hot-spot of the nanoantenna for both structures and found out that the electric field produced at the hot-spot of a dimer is 15 times stronger with the waveguide excitation compared to the standard SERS substrate. Moreover, I have shown that the collected power at the waveguide port is comparable to the power collected by an objective lens with NA=0.9 at a slightly longer wavelength. It is also important to mention that due to the long interaction length along the waveguide, the proposed integrated structure can collect more scattered Raman signal compared to a standard SERS substrate method. Finally, it is worth mentioning that such an integrated structure not only is useful for Raman spectroscopy, but also for many similar applications like fluorescence and other nonlinear phenomena.

CHAPTER 4 : TWO-SCALE STRUCTURE FOR GIANT FIELD ENHANCEMENT: COMBINATION OF RAYLEIGH ANOMALY AND COLLOIDAL PLASMONIC RESONANCE

Sec. 4.1 Motivation

In the second chapters, I showed that the hotspot of the field enhancement occurs between nanometer-sized gaps of nanoparticles where the intensity of light is enhanced by orders of magnitude [107]. In order to attain nanoscale gap between the nanoparticles in the cluster (down to 1 nm) and avoid costly and time consuming lithographic techniques, chemical self-assembly techniques have been exploited [108]–[111]. For example, in [112], [113] electrohydrodynamic flow and chemical crosslinking are combined to yield gold nanospheres cluster with 0.9 nm sized gaps. Although reducing the gap size boosts the field, the field enhancement that can be achieved using sub nanometer-sized gap plasmonic particles has an ultimate constraint [114], [115]. Strictly speaking, the intrinsic nonlocality of the dielectric response of the metal causes this ultimate constraint rather than its inherent losses[116]–[118]. From a physical point of view, the charge density is not perfectly restrained on the surface but is slightly diffused into the volume of the nanoparticle [119] which restricts the field enhancement. Realization of sensitive sensors requires even higher levels of field enhancement than what is currently achieved in current plasmonic chemically assembled surfaces. Consequently, it is of crucial importance to make use of other pathways along with plasmonic resonances to further enhance the field.

On the other hand, periodic structures provide another avenue to tailor light-matter interaction. Specifically, one promising way of further enhancing the field and overcoming the aforementioned limit is to employ the constructive interference of scattered fields in periodic arrays of metallic nanostructures. This interesting phenomenon, also known as Rayleigh anomaly, leads to sharp resonant-like peaks in the

scattering, absorption and emission spectra at the wavelength close to the period of the structure. With this goal of combining the capability of plasmonic resonances with Rayleigh anomaly, periodic arrays of metallic nanoparticles have been used to obtain remarkably narrow plasmonic resonance [120]–[128] in which the coupling between local surface plasmon resonance (LSPR) modes of the metallic nanoparticles and the lattice modes of the array has further enhanced the field compared to the field enhancement taken of individual metallic nanoparticles. However, in order to pattern periodic nanoparticles precisely, lithographic techniques need to be used [125], [127] which not only are expensive, restrict the size and the shape of individual nanoparticles, they also greatly limit the minimum gap spacing in nanoantennas. For instance, the gap spacing achieved in [127] using electron beam lithography is 5 nm which restricts getting strong field enhancement at the hot-spot of nanoparticles.

In this chapter, I introduce an architectural scheme that is translatable to large area manufacturing to achieve giant field enhancement by combining the Rayleigh anomaly and plasmonic resonance of nanoparticles. Compared to previous studies, I use two different sets of structures (with two distinct geometrical scales) and two different fabrication methods concurrently to realize high localization of fields. I refer to it as a "two-scale" method since the periodic array of scatterers and the chemically assembled oligomers have completely different scales and complementary fabrication methods. In the past Rayleigh anomaly has been used either to enhance the field in the periodic structure itself or to enhance the field that excites lithographically patterned nanoantennas located within the periodic array. Instead, working with directly and chemically assembled oligomers, as proposed here, allows to achieve nanogaps of the order of 1-2 nm[3], [108], [109], [112], [113]. Particularly, I use a periodic set of metallic nanorods deposited over a substrate along with chemically assembled metallic oligomers with nanometer-sized gap, between the nanorods (Fig. 4-1). The period of the nanorods is chosen such that its scattering resonance due to Rayleigh anomaly overlaps with the LSPR mode of the oligomers. In such a design, when the structure is illuminated with an incident wave, the coherent scattering from the nanorods (Rayleigh anomaly) boosts the field and

transfers energy to the LSPR mode of the oligomer nanoantennas (which have nanometer gap spacing) that leads to strong field enhancement. Indeed, I prove that the field enhancement achieved with this structure is the multiplication of that at each individual geometrical scale (nanoscale oligomers and microscale rods). Using a rigorous analytical study, I find an upper limit for the enhancement achieved from the periodic set of nanorods. The deposition of the nanorods can be done using lithography or by using the near-field electrospinning (NFES) method [129]. After depositing the nanorods with a suitable period, self-assembly techniques can be used to form cluster of oligomers with reproducible nm-sized gap. Notice that, in our proposed structure, I separate the fabrication of the periodic array from the formation of clusters of oligomers (which is done by self-assembly). Thus, oligomers which provide the field localization in their plasmonic resonance are not restricted for their shape or size and the interparticle gap spacing can be reduced to 0.9 nm thanks to the self-assembly method which leads to giant electric field enhancement. Note that despite all the efforts on pushing electron beam lithography into getting sub-10 nm gap spacing, still it is extremely difficult and costly to pattern nanoantennas with small feature sizes over a large area using that technique; this has been the base of our motivation to use chemical assembly techniques to reach 1 nanometer size gaps in nanoclusters over large surface areas [108], [109], [112]. I experimentally verify the ability of our structure for field enhancement by exploiting it for surface-enhanced Raman spectroscopy (SERS) which is a vibrational spectroscopy technique for identification of trace amounts of analytes. Approximately, SERS is proportional to the quadratic power of the field enhancement, if I assume that the excitation and scattering frequencies are close to each other. Therefore, probing SERS enhancement is a suitable tool to reveal the usefulness of the proposed two-scale structure. One of the most important aspects of our structure is that it does not require slow and expensive fabrication methods such as electron beam lithography (EBL) and focused ion beam (FIB) since the oligomers are formed using colloidal assembly and the nanorods can be fabricated using standard optical lithography or nanoimprinting. Note that the extra field enhancement obtained here by exploiting the Rayleigh anomaly cannot be obtained by further reducing

the nanoantennas gaps, since they are already in the few nm ranges thanks to direct chemical assembly of oligomers.

This chapter is organized as follows: first, I analytically demonstrate the effect of periodicity on the resonance wavelength of individual nanorods. Then I investigate the efficacy of the two-scale structure by tuning the nanorods period on boosting the near-field enhancement in hot-spot of oligomers. In the end, I illustrate the experimental SERS result and compare it with our defined figure of merit based on the field enhancement results achieved by full-wave simulations. Finally, I will conclude the chapter with some remarks.

Sec. 4.2 Statement of the problem

Our proposed two-scale structure consists of oligomers of plasmonics nanospheres with subwavelength diameter and gaps directly assembled on a surface in between the nanorords of a one dimensional (1D) periodic array, with period close to the resonance wavelength of the oligomers, as shown in Fig. 4-1(a). As it is well established, plasmonic nanospheres arranged as oligomers over a surface provide hot-spots for very large electric field in the nanogaps due to their plasmonic resonance. As already mentioned, the goal of this chapter is to combine the plasmonic resonance of the oligomers along with the Rayleigh anomaly due to the presence of the periodic 1D nanorods to achieve further, as factor, field enhancement compared to that of oligomers alone when illuminated with an incident plane wave. It is worth mentioning that the resonance frequency of oligomers depends on the number, size and the gap between the nanospheres which form the oligomers [3] though it is mainly dictated by the polarizability of single nanospheres. On the other hand, the wavelength at which the Rayleigh anomaly occurs depends on the period of the structure, host medium and angle of incidence. For the purpose of evaluating the ability of the two-scale structure in boosting the electric field, I define the electric field enhancement (FE) as a figure of merit [3], [99], [112], [130]

$$FE = \frac{|\mathbf{E}^{\text{tot}}(\mathbf{r})|}{|\mathbf{E}^{\text{inc}}(\mathbf{r})|} \tag{4.1}$$

where $|\mathbf{E}^{\text{tot}}(\mathbf{r})|$ is the magnitude of the total electric field at location $\mathbf{r}$, and $|\mathbf{E}^{\text{inc}}(\mathbf{r})|$ is the magnitude of the incident electric field at the same location in the absence of the structure. The FE indicates the ability of a nanoantenna system to enhance the electric field locally with respect to the incident illuminating field. Since the sizes of the 1D periodic nanorods and the oligomers are incomparable, for our proposed structure, with good approximation I can neglect the back-coupling from the oligomers to the nanorods and consider the plasmonics oligomers excited by the illumination field plus the one scattered by the nanorods. Thus, the total field enhancement achieved by the two-scale structure (FE_t) can be approximated with the product of field enhancement obtained by the periodic nanorods (FE_r) and the oligomers (FE_o) individually:

$$FE_t \approx FE_r \times FE_o \tag{4.2}$$

The mechanisms responsible for these two field enhancements are distinct: in oligomers, it is the plasmonic resonance whereas in the 1D periodic array of nanorods, the field enhancement is due to the Rayleigh anomaly (in [124] it is referred to as structural resonance).

Fig. 4-1(a) illustrates the general two-scale structure which consists of colloidal oligomers with random orientations located in between the periodic nanorods. In the two-scale structure, as it is shown in Fig. 4-1(a), the colloidal oligomers consist of an arbitrary number of plasmonic nanospheres with diameter "d_s", gap "g" and relative electric permittivity "ε_s". For what matters in this chapter, when their density is not high, these subwavelength oligomers can be considered as isolated scatterers by neglecting their mutual electromagnetic couplings. The larger scale is made of rods with diameter "d_r" and relative permittivity "ε_r", have period "p_r" along the *x*-direction and are long compared to the wavelength so they

are considered infinitely long along the *y*-axis. The rods are placed on top of a substrate with permittivity "ε_{sub}" under a medium with relative permittivity "ε_h".

Throughout this dissertation, the monochromatic time-harmonic convention $\exp(-i\omega t)$ is implicitly assumed and its notation is suppressed in the following. In all equations, bold fonts are used for vector quantities in phasor domain, and a bar under a bold font is used for dyadic quantities. Unit vectors are bold with a hat on top.

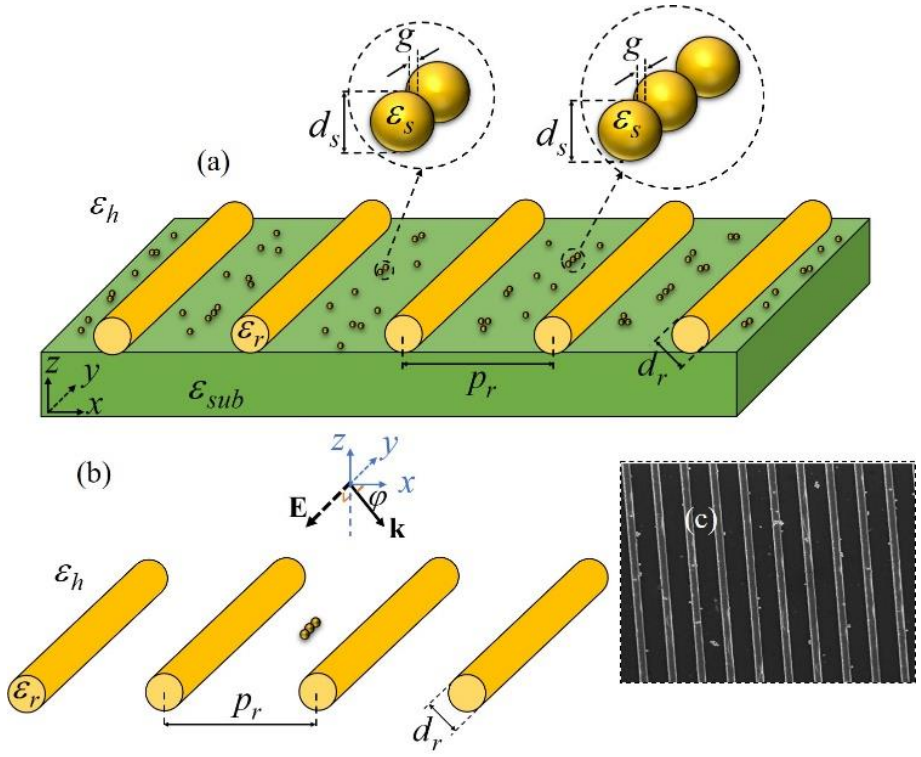

Fig. 4-1. (a) Proposed "two-scale" structure for enhancing the electric field at optical frequencies. It is made of oligomers of colloidal plasmonic nanospheres assembled within the nanorods of a 1D periodic array, on top of a substrate. (b) Simplified two-scale structure for analytical investigation consisting of a representative plasmonic linear trimer in the middle of the 1D periodic array of plasmonic nanorods in a homogeneous host medium. The orientation of the trimer is parallel to the nanorods axes and to the polarization of the incident plane wave. (c) Scanning Electron Microscopy (SEM) image of the fabricated structure, which consists of gold oligomers placed in between the periodic gold nanorods on the glass substrate. In this chapter, I investigate the field enhancement in the hot-spots of the oligomers.

Sec. 4.3 Analytical model

I present an analytical approach to determine the field enhancement of our proposed structure. While the method is general, in order to simplify the analytic investigation of the two-scale structure, I limit our study to linear oligomers of plasmonic nanospheres (dimers or trimers) that are placed in between plasmonic nanorods inside a homogeneous host medium with permittivity ε_h , as shown in Fig. 4-1(b). I consider that the nanorods are periodic along the x-axis and are long enough (compared to the wavelength, along the y-axis) so in absence of the nanospheres, I presume $\partial/\partial y = 0$ for any field quantity. Furthermore, as mentioned earlier, I consider the oligomers in between the nanorods to be subwavelength and separated from each other with enough distance. Therefore, I neglect not only the coupling among oligomers but also the coupling effect of oligomers on the nanorods but not vice-versa, i.e., I will focus on the field scattered by the nanorods that excites the oligomers. As previously shown in Eq. (4.2), the total field enhancement is the multiplication of the field enhancement caused by the 1D periodic array of nanorods, i.e., FE_r and the field enhancement produced due to the plasmonic resonance of the oligomers, i.e., FE_0 since the mechanism of each type of field enhancement is distinct. I start by obtaining the scattered field from the nanorods and then investigate the field enhancement caused by the oligomers in the next subsections, respectively.

A. Enhanced scattered electric field by the nanorod array

The goal of this section is to calculate the external electric field at the oligomers' location, which is the summation of the incident field and the scattered field from the nanorods. I start our analysis by assuming an oblique incident plane wave with transverse electric (TE) polarization along y , as noted in Fig. 4-1(b), as $\mathbf{E}^{\text{inc}}(\mathbf{r}) = \hat{\mathbf{y}}\, E_0 e^{ik_x x} e^{-ik_z z}$, where $k_x = k_h \cos(\varphi)$, $k_z = k_h \sin(\varphi)$, $k_h = k_0\sqrt{\varepsilon_h}$ is the wavenumber of host medium $k_0 = \omega\sqrt{\mu_0 \varepsilon_0}$ is the wavenumber of free space and φ is the angle of incidence with respect to x-axis. Since the incident field is polarized along the nanorods axis (the y-direction), and the nanorods are

long compared to the incident wavelength and their diameter is subwavelength, I model each nanorod with an induced equivalent electric polarization current I_n along the nanorod[131]–[133]. The induced current of the nth nanorod at location $\mathbf{r}_n$ (nth nanorod's location) is given by

$$I_n = \alpha_r E_r^{\text{loc}}(\mathbf{r}_n) \tag{4.3}$$

where $E_r^{\text{loc}}(\mathbf{r}_n)$ is the local electric field at the nth nanorod location polarized along y-direction and α_r is the electric polarizability of an infinitely long rod with diameter d_r (the cross section area is $A = \pi d_r^2/4$) defined as [134], [135]

$$\alpha_r = \frac{-i\omega\varepsilon_0(\varepsilon_r - \varepsilon_h)A}{1 - i\frac{k_h^2}{4}A(\varepsilon_r - \varepsilon_h)}. \tag{4.4}$$

Note that since the polarization currents and electric field are all along the *y*-axis, I simplify all the equations to scalar equations. The rods are periodic in the *x*-direction with period of p_r, and the location of the nth nanorod is $\mathbf{r}_n = \mathbf{r}_0 + np_r\hat{\mathbf{x}}$ where $\mathbf{r}_0$ denotes the reference rod location which I assume to be $\mathbf{r}_0 = 0\hat{\mathbf{x}} + 0\hat{\mathbf{z}}$. Therefore, the corresponding location of the nth nanorod is $\mathbf{r}_n = np_r\hat{\mathbf{x}}$. The polarization current on the nth nanorod is then $I_n = I_0 e^{ik_x np_r}$, where I_0 is the reference current (of the 0th nanorod) [136]. Thus, the external electric field at a general location $\mathbf{r}$ is written as the summation of the incident electric field and the scattered field from the 1D periodic set of nanorods as [137]

$$E_r^{\text{ext}}(\mathbf{r}) = E^{\text{inc}}(\mathbf{r}) + i\omega\mu I_0 G^{\infty}(\mathbf{r}, \mathbf{r}_0) \tag{4.5}$$

where $G^{\infty}(\mathbf{r}, \mathbf{r}_0)$ is the scalar periodic Green's function of magnetic vector potential with respect to the *y*-direction. The definition of elements of Green's function is presented in the Methods (A). The nanorods' local field at the reference rod location to be used in Eq. (4.3) is

$$E_r^{\text{loc}}(\mathbf{r}_0) = E^{\text{inc}}(\mathbf{r}_0) + i\omega\mu_0 I_0 \breve{G}^{\infty}(\mathbf{r}_0, \mathbf{r}_0) \tag{4.6}$$

Note that in the definition of local field (Eq.(4.6)), the contribution from the reference nanorod itself should be removed [136] and the value of the "regularized" scalar periodic Green's function $\breve{G}^{\infty}(\mathbf{r}_0,\mathbf{r}_0)$ is determined by the limit $\breve{G}^{\infty}(\mathbf{r}_0,\mathbf{r}_0)=\lim_{\mathbf{r}\to\mathbf{r}_0}[G^{\infty}(\mathbf{r},\mathbf{r}_0)-G(\mathbf{r},\mathbf{r}_0)]$, since both $G^{\infty}(\mathbf{r},\mathbf{r}_0)$ and $G(\mathbf{r},\mathbf{r}_0)$ are singular at $\mathbf{r}=\mathbf{r}_0$, where $G(\mathbf{r},\mathbf{r}_0)$ is the two dimensional scalar Green's function of magnetic vector potential as defined in the Methods (A). Substituting $E_r^{\mathrm{loc}}(\mathbf{r}_0)$ from Eq.(4.6) in Eq.(4.3), the current along the reference nanorod is found as

$$I_0=\frac{\alpha_r E^{\mathrm{inc}}(\mathbf{r}_0)}{1-i\omega\mu_0\alpha_r\breve{G}^{\infty}(\mathbf{r}_0,\mathbf{r}_0)} \tag{4.7}$$

By substituting Eq. (4.7) into Eq. (4.5), one can easily calculate the external electric field as a result of incident field and the multiple scattering by nanorods at an arbitrary oligomer location. One should note, as shown in Methods (B) that the periodic Green's functions in Eq. (4.7) and Eq. (5) have the terms $k_{zp}=\sqrt{\varepsilon_h k_0^2-(k_x+2\pi p/p_r)^2}$, with $p=0,\pm1,\pm2,...$, at the denominator. Therefore, when a given $k_{zp}\approx 0$ one has $G^{\infty}(\mathbf{r},\mathbf{r}_0)\approx B/k_{zp}$ and $\breve{G}^{\infty}(\mathbf{r}_0,\mathbf{r}_0)\approx C/k_{zp}$. At the Rayleigh's anomaly wavelength (which will be discussed later in Eq. (4.12) with more details), the scalar periodic Green's function of the magnetic vector potential has a "spectral" singularity occurring when $k_{zp}=0$ i.e., when $(k_x+2\pi p/p_r)=\pm\sqrt{\varepsilon_h}k_0$. Thus, I can approximate the reference current in Eq. (7) as $I_0\approx E^{\mathrm{inc}}(\mathbf{r}_0)\Big/\left(-i\omega\mu_0\breve{G}^{\infty}(\mathbf{r}_0,\mathbf{r}_0)\right)$. However, $E_r^{\mathrm{ext}}(\mathbf{r})$ in Eq. (4.5), has a finite value i.e., the electric field enhancement of the nanorods evaluated in the middle of two nanorods and at $d_r/2$ distance from the substrate is equal to 2 (This issue is investigated comprehensively in the Methods (B) by exploiting the Ewald representation of the Green's functions). Hence, the incident field intensity is enhanced by a factor of 4. Indeed, in the Raman spectroscopy, when the scattered frequency is close to the incident one, the maximum SERS intensity enhancement is 16.

In the next section, using these external field calculated at the location of an arbitrary oligomer, I will find the total electric field at the hot-spot of the oligomer.

B. Total electric field at oligomers' hot-spots

In the previous section I only investigated the field generated by the nanorods, however in the two-scale structure discussed here I consider an oligomer with subwavelength gap spacing placed between two adjacent nanorods. The field calculated in the presence of the nanorods in Eq.(4.5) acts as the external field applied to oligomers. I employ the single dipole approximation (SDA) method [3], [138] to model each of the M nanospheres of an oligomer. Accordingly, each plasmonic nanosphere is modeled with an induced electric dipole moment $\mathbf{p}_m$, with $m = 1, 2, ..M$. Indeed, due to the subwavelength size and the material of the nanospheres, I neglect their magnetic dipole and quadrupole moments. The induced electric dipole moment of the mth nanosphere at location $\mathbf{r}_m$ is found as

$$\mathbf{p}_m = \alpha_s \mathbf{E}_s^{\text{loc}}(\mathbf{r}_m) \tag{4.8}$$

where α_s is the electric polarizability of every nanosphere, assumed to be isotropic [138], [139] and $\mathbf{E}_s^{\text{loc}}(\mathbf{r}_m)$ is the local electric field at the m$^{\text{th}}$ nanosphere's location. The local electric field is the summation of the external field given by Eq. (4.5) and the field scattered by all the other nanospheres of the oligomer. Thus, the local electric field at the mth nanosphere's location is given by

$$\mathbf{E}_s^{\text{loc}}(\mathbf{r}_m) = \mathbf{E}^{\text{ext}}(\mathbf{r}_m) + \sum_{\substack{l=1 \\ l \neq m}}^{M} \underline{\mathbf{G}}(\mathbf{r}_m, \mathbf{r}_l) \cdot \mathbf{p}(\mathbf{r}_l) \tag{4.9}$$

where $\underline{\mathbf{G}}(\mathbf{r}_m, \mathbf{r}_l)$ is the dipole dyadic Green's function providing the electric field as defined in [3]. To find the electric dipole moment $\mathbf{p}(\mathbf{r}_l)$ of the mth nanosphere, I combine Eq. (4.8) and Eq.(4.9), and solve the linear system ($m = 1, 2, ...M$) [3], [140]

$$\sum_{l=1}^{M} \underline{\mathbf{A}}_{ml} \cdot \mathbf{p}(\mathbf{r}_l) = \alpha_s \mathbf{E}^{\text{ext}}(\mathbf{r}_m), \;\; \underline{\mathbf{A}}_{ml} = \begin{cases} \underline{\mathbf{I}} & l = m \\ -\alpha_s \underline{\mathbf{G}}(\mathbf{r}_m, \mathbf{r}_l) & l \neq m \end{cases} \tag{4.10}$$

The total scattered field by the rods (E_r^{ext} in Eq. (4.5)), is polarized along the *y*-axis and acts as the external field for the oligomers and therefore $\mathbf{E}^{\text{ext}}$ has nonzero component only in the *y*-direction. For simplicity, for a linear oligomer along the *y*-direction, the total electric field at the hot-spot (interparticle gap of the oligomer) along the *y*-direction reads

$$E^{\text{tot}}(\mathbf{r}_{\text{obs}}) = E_r^{\text{ext}}(\mathbf{r}_{\text{obs}}) + \frac{\sum_{m=1}^{M} \alpha_s g(\mathbf{r}_{\text{obs}}, \mathbf{r}_m) E_r^{\text{ext}}(\mathbf{r}_m)}{1 - \sum_{\substack{l=1 \\ l \neq m}}^{M} \alpha_s g(\mathbf{r}_m, \mathbf{r}_l)} \tag{4.11}$$

where $g(\mathbf{r}_{obs}, \mathbf{r}_m)$ is the $\hat{\mathbf{y}}\hat{\mathbf{y}}$ element of the dipole dyadic Green's function defined in [3]. By dividing Eq. (4.11) over the incident electric field, I obtain total field enhancement of Eq. (4.1).

So far, I have developed a rigorous analytical method to calculate the field enhancement of our proposed structure. Using the above method, in the next section, I obtain the field enhancement for different cases of our proposed two-scale structure.

Sec. 4.4 Results and discussions

A. Rayleigh anomaly

Our goal is to exploit the Rayleigh anomaly to enhance local fields beyond that which can be achieved solely using LSPR. The Rayleigh anomaly arises in a periodic array of scatterers when the wavelength is related to the period of structure (as described in Eq. (4.12)) due to the coherent interaction in multiple scattering. This interaction yield a geometric sharp "resonance-like" peak which appears when the wavelength of the incident light matches the periodicity of the structure [124], [141], [142]. I can achieve our goal by carefully choosing the period of an array of nanorods such that the spectral location of the

anomaly is commensurate with the plasmonic resonance of oligomers. In this system, the nanorods deliver enhanced local field to the plasmonic oligomers which then enhance it further.

The Rayleigh anomaly in periodic structures becomes visible as a sudden change of a measurable parameter such as transmission or reflection from a surface under the incident wave when the wavelength or angle of incidence is varying and happens at the wavelength [143], [144]

$$\lambda_r = \frac{p_r}{p}\sqrt{\varepsilon_h}\left(\pm 1 - \cos\varphi\right), \quad p = \pm 1, \pm 2, \ldots \tag{4.12}$$

For normal (to the plane of periodicity) angle of incidence and assuming the host medium to be the vacuum, a Rayleigh anomaly occurs when the wavelength of incident wave matches the array period. To demonstrate this phenomenon more clearly, I consider a 1D periodic set of gold nanorods in a homogeneous host medium (vacuum), when the structure is excited by a normal plane wave polarized along the nanorod, as shown in Fig. 4-2, and investigate the electric field enhancement FE_r for various nanorods diameter and periodicity. The electric field enhancement is calculated based on Eq. (4.1), in the middle of the unit cell of a periodic array of gold nanorods. I use the Drude model for gold permittivity of the nanorods as in [145]. I consider rods' diameters of 40 and 80nm and different array periods of 545, 633 and 785 nm.

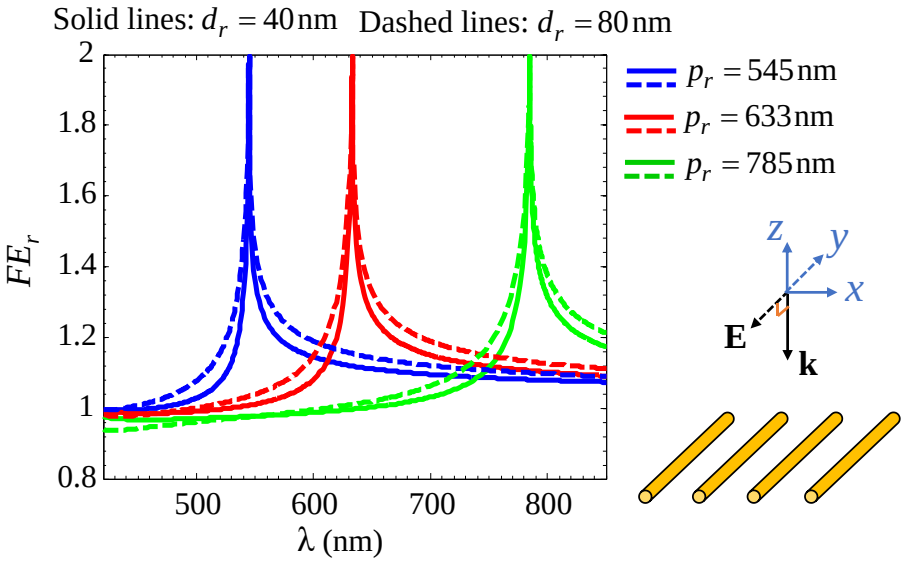

Fig. 4-2. Electric field enhancement FE_r achieved in the middle of the unit cell of a periodic array of gold nanorods, in a vacuum host medium, when the nanorods are excited by normal incidence plane wave polarized along the rod axis. (Field is evaluated at a point equidistant from the two adjacent rods.) Solid and dashed lines represent the result pertaining to rods' diameter of 40nm and 80 nm respectively. The period of nanorods assumed to be 545nm, 633nm and 785 nm, shown with blue, red and green respectively. Rayleigh anomaly happens at wavelength equal to the period here (normal incidence case), independent of rods diameter.

As it is clear from Fig. 4-2, the periodic structure possesses a sharp peak at the wavelength that is commensurate to the period of the structure when it is illuminated with a normal plane wave polarized along the nanorods. Moreover, as discussed in section (3. A) and also in Methods (B), the magnitude of the peak is equal to 2, independent of the value of the rod diameter and period. This is a striking result since for most of the spectroscopy applications, the signal enhancement is proportional to the fourth power of electric field enhancement. Therefore, spectroscopy signals can be significantly enhanced by simply using a two-scale structure. It is worth mentioning that, although the diameter of rods does not play any role in determining the anomaly frequency when it is subwavelength, larger diameters provide field enhancement in wider bandwidth.

Despite the importance of normal incidence, it is interesting to study the effect of the wave incident angle on the frequency and strength of the anomaly since in experiments the structure will be excited by a

Gaussian beam which can be represented as a weighted summation of multiple plane waves coming at different angles. To that end, I consider a 1D periodic array of gold nanorods with diameter of 80 nm and period of 545 nm, located in a homogeneous host medium (vacuum). I assume a plane wave polarized along the rod's axis, arriving at an angle φ with the plane of period, as shown in Fig. 4-3. I calculate the electric field enhancement in the middle of an array unit cell, as a function of incident angle and wavelength based on the formulation in Section 3. Results in Fig. 4-3 describe that the maximum electric field enhancement is obtained at normal incidence ($\varphi = 90^o$), at the wavelength that matches the period of structure (Rayleigh anomaly at 545nm). For other angles of incidence ($\varphi \neq 90^o$), the structure provides a field that peaks at both larger and smaller wavelengths (compared to periodicity) as is also clearly illustrated in Eq. (4.12). A result showing the field enhancement FE_r at any location between two contiguous rods, calculated based on full-wave simulations, is shown in Methods (B), for the case of a period of $p_r = 785$ nm, at the Rayleigh anomaly wavelength ($\lambda_r = p_r$), leading to a result in agreement with the green curve in Fig. 4-2.

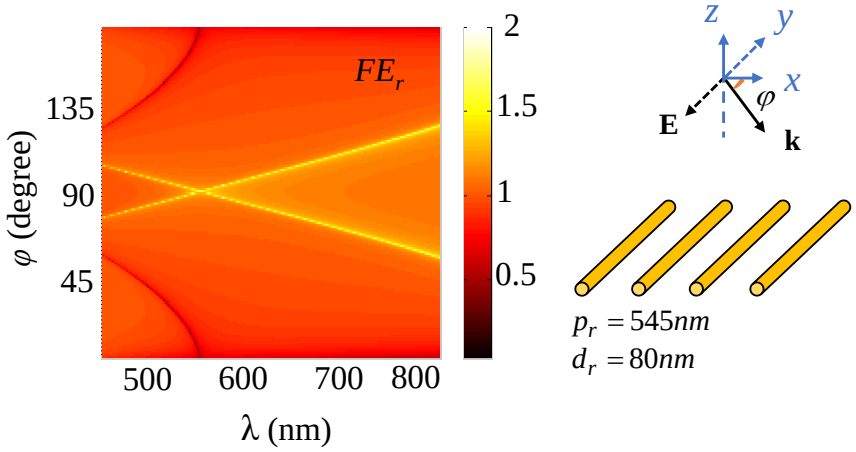

Fig. 4-3. Electric field enhancement FE_r versus wavelength and plane wave angle of incidence, calculated in the middle of a unit cell of the array (at the same distance from the two nearest nanorods). Gold nanorods have diameter $d_r = 80$ nm and period $p_r = 545$ nm, all supposed to be in vacuum for simplicity. The Rayleigh anomaly, responsible for the strongest enhancement, occurs at the wavelength given by Eq. (4.12).

B. Two-scale structure field enhancement

So far, I have only used the structural field enhancement due to the 1D periodic set of gold nanorods. However, the our ultimate goal is to combine this coherent kind of enhancement due to the larger scale of fabrication with the one caused by gold oligomers' plasmonic resonance In doing so the wavelength of geometric field enhancement (i.e., the array's period) should be tuned close to the localized surface plasmon resonance of the oligomers to achieve an even stronger electric field than that obtained by the oligomers alone [3], [109]. Fig. 4-4 illustrates the electric field enhancement versus wavelength of the incident plane wave for a linear trimer of gold nanospheres located in the middle of a unit cell of the periodic array of gold nanorods, as shown in Fig. 4-1(b). The maximum electric field enhancement achieved by a linear oligomer occurs if the polarization of incident field is parallel to the oligomer axis [3], [99], [146]. So, I assume that the trimer axis is parallel to the nanorods and also to the polarization of the incident plane wave as shown in Fig. 4-4. I consider two different cases for the period p_r of gold nanorods: (i) when the period is far from the resonance wavelength of the trimer (Fig. 4-4(a)) and (ii) when the period is the same as the trimer resonance wavelength (Fig. 4-4(b)).

In both cases, the diameter of each nanosphere of the trimer and the gap spacing between them are fixed as $d_s = 40$ nm and $g = 5$ nm respectively. If I apply the SDA method in Eq. (4.11) to calculate the trimer resonance in the vacuum, the resonance wavelength would be 496 nm. Therefore, for the first abovementioned case, I choose $p_r = 750$ nm (this is pretty arbitrary, and I chose this number for the period to be far from the trimer's plasmonic resonance). The zoomed-in inset in Fig. 4-4 (a) shows the nanorods anomaly which happens at the wavelength equal to the period. It is clear that since the 1D periodic set of nanorods does not have anomaly at 496 nm, the field enhancement of the two-scale structure (rods + trimer) does not differ from the field enhancement of the trimer without periodic nanorods. It is also worth noting that the field enhancement of the two-scale structure has another small peak around the wavelength near to the period of the nanorods. This is due to the Rayleigh anomaly. Note that because the plasmonic resonance

of the trimer does not coincide with the Rayleigh anomaly, the total field enhancement is not further boosted in this case.

In the second case in Fig. 4-4(b), the period of nanorods is chosen to be the same as the trimer resonance wavelength, i.e. $p_r = 496$ nm. As Fig. 4-4(b) illustrates the field enhancement of the two-scale structure has only one peak. In this case the field enhancement is approximately equal to the product of electric field enhancement achieved by each of the two different structures individually as shown in Eq. (4.2).

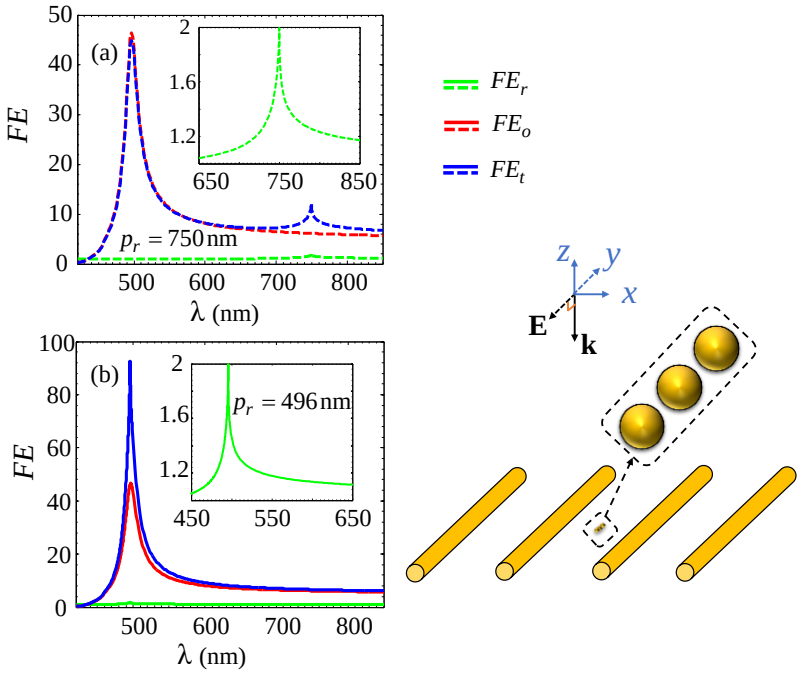

Fig. 4-4. Electric field enhancement versus wavelength of the incident light (polarized along the *y*-axis) obtained using the two-scale method, which consists of mixing a gold linear trimer placed in between the 1D periodic array of gold nanorods. The nanorods' period and the trimer resonance plasmonic wavelength are (a) different, and (b) the same. The diameter of nanorods and nanospheres, as well as the gap between spheres, are kept constant as 80, 40 and 5 nm, respectively. The nanorod array period is $p_r = 750$ nm in the first case (a) and $p_r = 496$ nm in the second one (b). In order to achieve maximum field enhancement by the two-scale structure, the nanorods period must commensurate with the oligomer's resonance wavelength.

So far, I have used plane wave excitation as the incident field in our analysis. However, in reality, used laser beams possess Gaussian-like spatial field distribution. In order to study the ability of our proposed two-scale structure in further enhancing the field under Gaussian beam illumination, I recall that any beam can be decomposed into an infinite set of plane waves with different amplitudes and angles of incidence. Therefore, I approximate the Gaussian beam with a finite set of plane waves ranging from -30 degrees to 30 degrees from the normal incidence with different amplitudes (to mimic the continuous field distribution that make up the Gaussian beam) and use our aforementioned analysis of plane waves to obtain the field in the presence of the periodic nanorods (note that this is a good approximation since the waist of the beam is much larger than the wavelength and the weights of plane waves with other angles of incidence are negligible). It is important to note that the waist of the Gaussian beam w_0 [147] should be chosen large (compared to the wavelength) to excite a sufficient number of nanorods (more than 15 nanorods). To that end, I excite our proposed structure using a Gaussian beam with minimum waist $w_0 = 4$ μm (see Fig. 4-5) assuming the period of the nanorods to be $p_r = 496$ nm. The diameter of nanorods, and diameter and gap spacing of trimer are kept constant as the case studied in Fig. 4-4(b) as 80 nm, 40 nm and 5 nm, respectively. Note that since the waist of the Gaussian beam is large compared to the wavelength, the weight of the normal plane wave and of plane waves with incidence angles close to normal incidence are larger than that relative to other angles in forming the Gaussian beam. Therefore, I do not expect the results of the field enhancement due to the Rayleigh anomaly to be drastically different from the results of normal incidence illumination. I mainly expect a broadening of the peak when varying wavelength, i.e., a wider bandwidth of field enhancement caused by the array of rods. However, as results clearly illustrate, the peak of the field enhancement for the Gaussian beam is slightly smaller than that of a plane wave in Fig. 4-2, since for this scenario the power of the beam is distributed over different angles. Besides, in this case, there are two peaks (see the green line) which do not happen at the period of the nanorods. To provide the reason for this behavior, note that as Fig. 4-3. illustrates, when the wavelength of the incident light matches the period,

field enhancement peaks at normal incidence, however, for larger and smaller wavelengths, the field enhancement peaks at two oblique angles. Therefore, for wavelengths close to (and not equal to) the period of the nanorods, the field enhancement peaks.

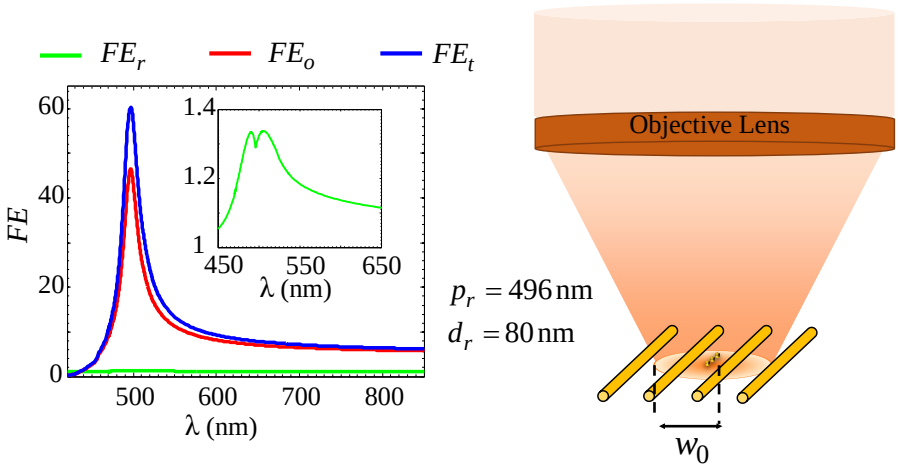

Fig. 4-5. Electric field enhancement versus wavelength of an incident field (a Gaussian beam), generated by: a 1D periodic array of gold nanorods (green line), a hot-spot of an individual gold trimer (red line), and a hot-spot of a trimer located in between the array of nanorods – the two-scale structure (blue line). The hot-spot is in the middle of a gap between two nanospheres of the trimer. The simulation is obtained assuming: the diameter of gold nanorods, the diameter of nanospheres, the gap spacing between nanospheres, and the period of the nanorod array are kept constant as 80 nm, 40 nm, 5 nm, and 496 nm, respectively. As one observes, the idea of two-scale structure is not limited only to the plane wave excitation and works well even with Gaussian-beam excitation.

The capability of obtaining large field enhancement has been extensively utilized in SERS spectroscopy [148] to detect trace amount of biochemical analytes [149]. Here I demonstrate that our two-scale structure is suitable for this particular and important application. In Fig. 4-6 I consider a 1D periodic set of gold nanorods on a glass substrate with the vacuum above. SERS involves at least two wavelengths in the measurement process, the incident field – here 785 nm – and the Raman scattered light which is reduced in energy – here I assume 850 nm for simplicity based on a 1000 cm-1 vibrational frequency [112], [113]. Thus, I design the period of our structure to attain the largest multiplicative enhancement at these two wavelengths. I use gold nanorods with square cross section with 150 nm side size and with period of 900

nm. I consider a gold oligomer placed on top of the substrate in the middle of the nanorod's array unit cell, where the diameter of each nanosphere is 80 nm and the gap spacing of them is 0.9 nm. The value for gap spacing is taken from [150], [151], [112], [113] which shows reproducible gap spacings of 0.9 nm. Moreover, [112] shows that the majority of oligomers have a resonance wavelength near that of linear trimers, therefore, in our model I use a single linear trimer between the nanorod array arranged parallel to the nanorods. Full-wave simulations in Fig. 4-6 are based on the frequency domain finite element method (FEM), implemented in the software CST Microwave Studio by Computer Simulation Technology AG. I consider normal plane wave excitation with electric field polarized along the nanorods and the linear trimer axis. Fig. 4-6 depicts the electric field enhancement achieved by individual trimer and the combination of trimer and gold nanorod array (i.e., by the proposed two-scale method).

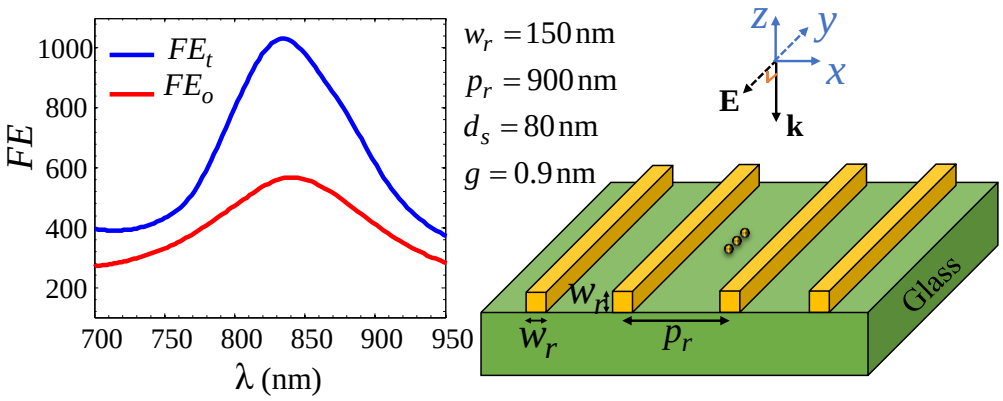

Fig. 4-6. Electric field enhancement versus wavelength of incident light generated by an individual gold trimer (red line) and by the combination of a periodic array of nanorods and trimer, i.e., the proposed two-scale structure (blue line). Field enhancement is calculated in the trimer hot-spot using full-wave calculations based on the FEM. The structure is located on a glass substrate, with the vacuum above. The side width of gold nanorods with square cross section is 150 nm whereas the array period is 900 nm. The diameter of gold nanospheres and the gap between them is 80nm and 0.9nm, respectively. The structure is excited by a normal-incidence plane wave polarized along the nanorods and trimer axis. For SERS application, I design our structure to attain the largest multiplicative enhancement at incident and scattered wavelength (see Eq. (4.13)).

To evaluate the performance of our two-scale structure, I define a figure of merit as

$$FoM = \left|FE_t / FE_o\right|^2_{\lambda=785} \times \left|FE_t / FE_o\right|^2_{\lambda=850} \quad (4.13)$$

where FE_t and FE_0 are the field enhancement of the two-scale structure and the individual oligomers at 785 nm and 850 nm, that are the incident and Raman scattered wavelengths, respectively. FoM is our figure of merit that shows the enhancement of the SERS enhancement factor from incorporating our nanorod array, compared to the case without periodic nanorods. According to Fig. 4-6, $\left|FE_t / FE_o\right|^2_{\lambda=785}$ is 2.31 and $\left|FE_t / FE_o\right|^2_{\lambda=850}$ is 3.06, yielding an FoM of 7.07. These results theoretically demonstrate the benefit of our two-scale structure.

C. Experimental results

I now verify our theoretical predictions of augmented electric field enhancement due to the exploitation of Rayleigh anomaly through SERS measurements. Here SERS is generated by a surface fabricated using two completely different fabrication methods. As described in the methods section (C-D), I use a simple self-assembly method to deposit colloidal gold nanosphere oligomers on a glass substrate and fabricate periodic gold nanorods on a glass substrate through standard electron beam lithography. Once the rods are fabricated, gold nanospheres are chemically crosslinked onto the glass with an amine coupling. This process is repeated yielding oligomers. Previous work has shown that diffusion drives the formation of gold nanosphere oligomers suitable for investigation in this work [108]. Fig. 4-7 (a) and (b) depict scanning electron microscopy (SEM) images of gold nanosphere oligomers deposited on bare glass, and also deposited within the gold nanorod array, respectively. In Fig. 4-7 one may observe similar characteristics of gold nanosphere oligomers in both cases. The oligomers are separated by enough distance to avoid intra-oligomer strong coupling since the scope of this chapter is just showing the oligomers-nanorods combined effect. Previous work has shown that the resonance frequency of close-packed gold nanosphere oligomer is nearly the same as the linear oligomers' with the same number of particles along

the axis of polarization[112]. Consider a close-packed hexamer (as shown in Fig. 4-7 of [112].): three nanospheres are along any given axis of polarization. For such an arrangement of nanospheres, the oligomer resonates at nearly the same frequency as a linear trimer [112]. I have chosen 80 nm gold nanosphere oligomers because the resonance frequency of dimers and trimers of these sizes are best suited for providing large field enhancements at both 785 nm and approximately 850 nm.

Fig. 4-7(c) depicts the SERS spectra of standard SERS analyte benzenethiol (BZT) obtained using a surface with the two-scale structure and also (for comparison) using a surface covered only with colloidal oligomers, acquired as outlined in the methods section. Here, I use the same substrate for SERS measurements within (blue curve) and away from the gold nanorods (red curve), but on the same glass substrate, allows to minimize variation of oligomer enhancement and focus instead on the field enhancement augmentation due to the nanorod array (blue curve). Both spectra exhibit a large fluorescence peak from the glass microscope slide that appears in this background-subtracted data as a broad peak from 875 nm to 885 nm. Comparison of the two spectra at BZT's in-plane ring breathing mode at 1000 cm−1 (observed at 852 nm) reveals a signal enhancement of 5.84 times for the surface made of the two-scale structure compared to the surface made of individual oligomers. This experimentally observed enhancement is in good agreement with the predicted FoM for this system and demonstrates that the Rayleigh anomaly field enhancement is relatively robust to scattering caused by fabrication defects.

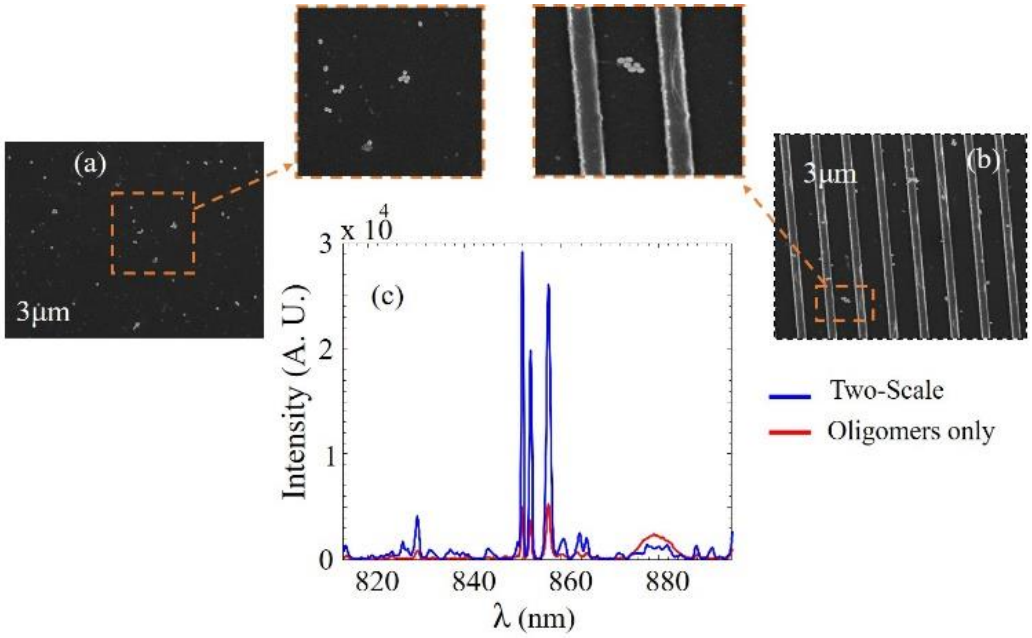

Fig. 4-7. SEM images of gold nanosphere oligomers without nanorod array(a) and when placed within the gold nanorod array (b). In both cases, the structure is deposited on glass. The gold nanorods have a period of 900 nm and square cross section with 150 nm side. The gold nanosphere oligomers are expected to have an 80 nm diameter and a 0.9 nm gap from nanosphere to nanosphere. (c) shows the SERS spectra relative to the proposed two-scale structure shown in Fig. 4-7(b) and to the oligomers-only structure shown in Fig. 4-7(a), versus wavelength. The two-scale structure provides much stronger SERS signal.

Sec. 4.5 Methods

A. The magnetic vector potential Green's function

The spectral representation of the magnetic vector potential Green's function $G^{\infty}(\mathbf{r},\mathbf{r}_0)$ for a periodic array of line sources along the *y*-direction where $\mathbf{r}$ is the observation point and $\mathbf{r}_0$ is the reference source point (the source of a reference rod) is defined as [152]

$$G^{\infty}(\mathbf{r},\mathbf{r}_0)=\sum_{p=-\infty}^{\infty}\frac{i}{p_r}\frac{e^{ik_{xp}(x-x_0)}}{2k_{zp}}e^{ik_{zp}|z-z_0|} \tag{4.14}$$

where $k_{zp}=\sqrt{k_h^2-k_{xp}^2}$ and $k_{xp}=k_x+2\pi p/p_r$ is the pth Floquet harmonic wavenumber. Here $k_x p_r$ is the phase shift from one line source to the other, imposed by the incident field. Note that here, G^{∞} is the Green's function of the magnetic vector potential A (both are scalar and in the y direction) and is related to the y component of the electric field as $E(\mathbf{r})=i\omega\mu_0 A(\mathbf{r})$. I apply the Ewald method to accelerate the convergence of the above series, and to have explicit both spatial and spectral singularities. Therefore, the Green's function is written as the summation of the spatial and the spectral parts as[152]

$$G^{\infty}(\mathbf{r},\mathbf{r}_0)=\sum_{n=-\infty}^{\infty}g_n^E(\mathbf{r},\mathbf{r}_0)+\sum_{p=-\infty}^{\infty}\tilde{g}_p^E(\mathbf{r},\mathbf{r}_0) \tag{4.15}$$

where the first term is the modified spatial representation and the second term is the modified spectral representation of the Ewald formulation which are presented in Eq. (4.5) and Eq. (4.6) of [153] respectively. The spatial part contains the logarithmic singularity in g_0^E when $\mathbf{r}\to\mathbf{r}_0$ whereas the spectral part contains the spectral singularities when $k_{zp}\to 0$. The "regularized" Green's function in Eq. (4.6) is defined as $\breve{G}^{\infty}(\mathbf{r}_0,\mathbf{r}_0)=\lim_{\mathbf{r}\to\mathbf{r}_0}[G^{\infty}(\mathbf{r},\mathbf{r}_0)-G(\mathbf{r},\mathbf{r}_0)]$, where $G(\mathbf{r},\mathbf{r}_0)=(i/4)H_0^{(1)}(k_h|\mathbf{r}-\mathbf{r}_0|)$ represents the scalar 2D Green's function of the magnetic vector potential of the array, that is evaluated at the reference nanorod location $\mathbf{r}_0$ without considering the field contribution of the same nanorod at $\mathbf{r}_0$. After taking the limit, this regularized Green's function is represented based on the Ewald method as

$$\breve{G}^{\infty}(\mathbf{r}_0,\mathbf{r}_0)=\sum_{p=-\infty}^{\infty}\frac{i}{2p_r k_{zp}}\operatorname{erfc}\left(\frac{-ik_{zp}}{2E}\right)+\sum_{\substack{n=-\infty\\ n\neq 0}}^{\infty}\frac{1}{4\pi}e^{ik_x np_r}\left(\sum_{q=0}^{\infty}\left(\frac{k_h}{2E}\right)^{2q}\frac{1}{q!}E_{q+1}(R_n^2E^2)\right)+\frac{1}{2\pi}\ln\left(\frac{k_h}{2E}\right)+\frac{\gamma}{4\pi}-\frac{i}{4}+\frac{1}{4\pi}\sum_{q=1}^{\infty}\left(\frac{k_h}{2E}\right)^{2q}\frac{1}{q!}\frac{1}{q} \tag{4.16}$$

where $R_n=|n|\,p_r$ and E is the Ewald splitting parameter. The optimum value to minimize the overall number of terms needed to calculate the Green's function is $E_{opt}=\sqrt{\pi}/p_r$ [153]. In Eq. (4.16) though the spectral singularity remains as in Eq. (4.15) and it plays a major role in the field enhancement due to the singularity arising when $k_{zp}\to 0$ for some p.

B. Limit of field rnhancement at Rayleigh anomaly

I prove here that in our periodic structure, when the wavelength of the incident light matches λ_r in Eq. (4.12), the field enhancement due to the nanorods in the middle of two adjacent nanorods (FE_r) and at $d_r/2$ distance from the surface of the substrate is exactly 2. Indeed, I note that at that wavelength, $|k_{xp}|=|k_x+2\pi p/p_r|=k_h$, hence $k_{zp}=0$. Therefore, $G^{\infty}(\mathbf{r},\mathbf{r}_0)$ in Eq. (4.14) and Eq. (4.15) tends to infinity. On the other hand, also the first summation in Eq. (4.16) in calculating $\breve{G}^{\infty}(\mathbf{r}_0,\mathbf{r}_0)$ is singular, i.e., $\breve{G}^{\infty}(\mathbf{r}_0,\mathbf{r}_0)$ tends to infinity as well. By substituting Eq. (4.7) in Eq. (4.5), I get

$$E_r^{\text{ext}}(\mathbf{r})=E^{\text{inc}}(\mathbf{r})+i\omega\mu_0\frac{\alpha_r E^{\text{inc}}(\mathbf{r}_0)}{1-i\omega\mu_0\alpha_r\breve{G}^{\infty}(\mathbf{r}_0,\mathbf{r}_0)}G^{\infty}(\mathbf{r},\mathbf{r}_0). \tag{4.17}$$

Note that when $k_{zp}\to 0$ both the numerator and denominator of the second term in Eq. (4.17) tend to infinity because of the singularity in both $G^{\infty}(\mathbf{r},\mathbf{r}_0)$ and $\breve{G}^{\infty}(\mathbf{r}_0,\mathbf{r}_0)$. Assuming the reference nanorod is

at $\mathbf{r}_0 = (0,0)$ and that the field observation point is at $\mathbf{r} = p_r / 2\ \hat{\mathbf{x}}$, i.e., exactly in the middle of two nanorods, due to the Rayleigh condition (12) I have $\mathbf{r} = \lambda_r / 2\ \hat{\mathbf{x}}$. Therefore, by taking the limit of $E_r^{\text{ext}}(\mathbf{r})$, I get

$$\lim_{k_{zp}\to 0} E_r^{\text{ext}}(\mathbf{r}) = E^{\text{inc}}(\mathbf{r})\left[1 - e^{-ik_{\text{h}}(x-x_0)}\right] = 2E^{\text{inc}}(\mathbf{r}) \tag{4.18}$$

which proves that the field enhancement due to the Rayleigh anomaly is equal to 2. The field intensity enhancement is thus equal to 4. Despite the analytic theory whose results are shown in Fig. 4-2, I also confirm the findings with full-wave simulations. Fig. 4-1. M.B. illustrates the field enhancement at the Rayleigh anomaly wavelength ($\lambda_r = p_r$), between two adjacent nanorods. The result is calculated using full-wave simulations based on the software CST Microwave Studio by Computer Simulation Technology AG, for an array of periodic gold nanorods, with 80 nm diameter and 785 nm period. The field enhancement for the same geometrical configuration versus wavelength, calculated based on the analytic formulation in Section 3 is shown with the green dashed line in Fig. 4-2.

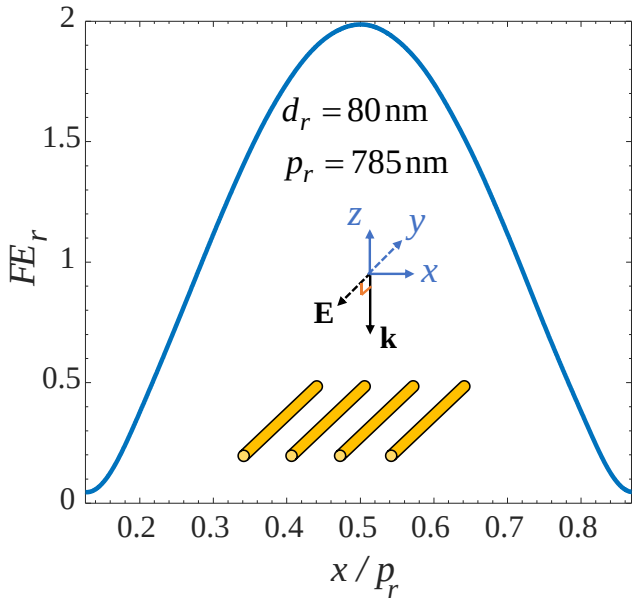

Fig. 4-8. Electric field enhancement between two nanorods in a periodic array of nanorods calculated at the Rayleigh anomaly wavelength $\lambda_r = p_r$ by full-wave simulations for normal plane wave incidence.

As Fig. 4-8 demonstrates, the maximum field enhancement FE_r is achieved in the middle of two nanorods, because of the Rayleigh anomaly, and it reduces closer to the nanorods. As a result, in general, by using a two-scale structure in SERS experiment, nanoparticles will experience an enhanced electric field compared to a conventional SERS substrate (without periodic rods). The maximum enhancement happens when the gold nanoparticles are in the middle of two contiguous nanorods.

C. Fabrication of nanorod array substrate

Array of nanorods with side size of 150 nm is fabricated using standard negative tone electron beam lithography. Briefly, glass coated with 50nm gold and a 5nm Titanium adhesion layer (Ted Pella) substrates are cleaned and then Ma-N 2401 (Microchem) is spin coated for use as the photoresist. The resist is exposed in a Magellan XHR SEM (FEI) at 25 pA and 30kV and subsequently developed in Ma-D (Microchem). The substrate is then etched with ion milling (IntIvac) to remove gold in the unexposed regions leaving nanorods. The titanium layer is etched with a 1:4 H2O2:H2SO4 solution to ensure that nanoparticle attachment will occur on the plane of the array, and to remove remaining photoresist.

D. Nanoparticles attachment

Nanorod array substrates are submerged in 0.5mMol (3-Aminopropyl) triethoxysilane (APTES) (Sigma Aldrich) in deionized water overnight to form a self-assembled monolayer selectively on glass yielding primary amine groups. 80 nm lipoic acid functionalized gold nanoparticles synthesized via a seeded growth method described by [154]. These particles are functionalized with carboxylic acid end groups by replacing the solution with DI water adjusted to pH 11.67 with sodium hydroxide (Sigma) and 0.1 mMol Lipoic acid and allowing the particles to sit overnight. The particles are washed with DI water and are deposited onto the glass surface by carbodiimide crosslinking with the APTES monolayer as described elsewhere. Diffusion drives the formation of random nanoparticle oligomers [109].

E. Surface-enhanced Raman scattering spectroscopy measurements

Nanorod array substrates with attached Au nanosphere oligomers – two-scale structures - are soaked overnight in 0.5 mMol benzenethiol in ethanol solution and then rinsed thoroughly prior to all SERS measurements. SERS measurements of two-scale structures, and Au nanosphere oligomers on glass are acquired in a Renishaw inVia Raman microscope for 10s at 0.125 mW using a 50x air objective lens. Spectra are background subtracted and Savitzky Golay smoothed. Spectra are obtained on and off of nanorod arrays using the same substrate to reduce possible sample to sample variation.

Sec. 4.6 Conclusion

By combining plasmonic resonance of metallic colloidal oligomers with a Rayleigh anomaly (i.e., a structural field enhancement due to coherent superposition of fields) of a 1D periodic array of nanorods, I overcame the limitation for field enhancement imposed by losses and nonlocality of the gold nanospheres' dielectric response. The method is called "two-scale" because it involves two completely different, and complementary, fabrication methods for enhancing electric fields: direct colloidal assembly and lithographic techniques. Specifically, the field enhancement of our proposed two-scale structure has been proved superior, theoretically and experimentally. to the field enhancement of a surface made of colloidal oligomers only (i.e, without the 1D periodic array of nanorods). I have provided a model that explains in physical and mathematical terms such field enhancement and its limitations and provided an experimental demonstration of the proposed structure showing SERS spectra of BZT analytes with increased FE due to the Rayleigh anomaly. The proposed process can eliminate the need to utilize slow and expensive fabrication methods (such as FIB and EBL) to form the oligomers and nanorods themselves by using nanoimprint or transfer methods.

Based on reciprocity of electromagnetic fields, giant field enhancement at the hot-spot of oligomers also implies that a photo-induced dipole (e.g., a dye) located in the proximity of the nanogap hot-spot of

oligomers radiates very strong far-fields, stronger than it would in absence of the nanorod array. Thus, the two-scale structure enhances radiation emission of dipoles as well. This physical effect is partly responsible to the two-scale structure Rahman enhancement since also the Raman scattered fields are enhanced with the mechanism discussed in this chapter, providing an order of magnitude extra SERS enhancement. I expect these two-scale fabricated substrates to find several applications in medical diagnostics, solar cells, sensors, and single molecule detectors because they provide an easy way to get extra field enhancement that cannot be obtained by further reducing the gaps, since they are already in the 1-2 nm range thanks to direct chemical assembly of oligomers.

CHAPTER 5 : POLARIZATION INSENSITIVE TWO-SCALE STRUCTURE FOR GIANT FIELD ENHANCEMENT

Sec. 5.1 Motivation

In the last chapter, I introduced a synergic structure, called two-scale, where field in the hotspot of nanometer-size oligomers is further enhanced by the Rayleigh anomaly caused by 1D set of periodic nanorods. Although 1D two-scale structure is capable of further enhancing the field (compared to using only plasmonic oligomers), the axis of the oligomer should be parallel to the nanorods to get maximum further field enhancement of 2 (this will be made clear later in this chapter). Thus, if majority of the oligomers' axis is not along the nanorods, the field enhancement that can be further achieved would be limited.

In this paper we combine the plasmonic resonance of the oligomers along with the Rayleigh anomaly achieved due to the presence of the periodic 2D array of nanorods to gain further field enhancement compared to oligomers alone when illuminated with an incident plane wave. Compared to the 1D array two-scale structure, the new scheme eliminates the limitation of dependency of the field enhancement on the direction of oligomers axis.

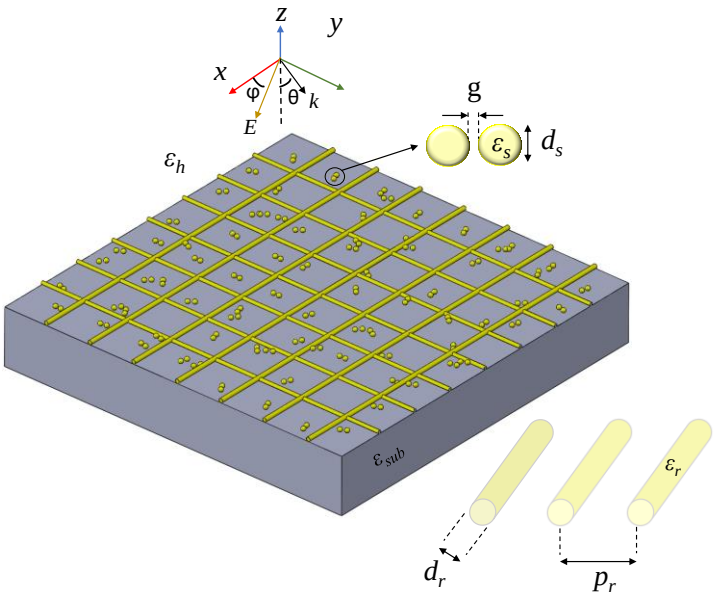

Fig. 5-1. Proposed "2D two-scale" structure for enhancing electric field at optical frequencies. It is made of oligomers of colloidal plasmonic nanospheres assembled within a 2D periodic array of nanorods, on top of a substrate, generating Rayleigh anomalies.

Sec. 5.2 Operational principle

To facilitate the explanation of our proposed structure, I show the 2D two-scale structure which is utilized in this chapter for field enhancement in Fig. 5-1. The interactive system of gap-sized oligomers and 2D periodic nanorods is excited by incident light from above (propagating along the –*z* direction). The large scale consists of a 2D plasmonic lattice of nanorods with equal period p_r along *x* and *y*, diameter d_r and relative permittivity ε_r. As was mentioned before, these rods can be fabricated using lithography and nanoimprinting methods. The Rayleigh anomaly frequency of this 2D set of nanorods (which will be discussed later) depends on its period and angle of the incident wave θ. The small scale is formed by an arbitrary number of metallic nanospheres with diameter d_s, relative permittivity ε_s and gap *g*, creating the oligomers. As already mentioned, the resonance frequency of oligomers depends on their number, material, size and the gap between the nanospheres which form the oligomers. Since the size of the oligomers is completely different with the nanorods, the coupling between them can be neglected and these subwavelength oligomers can be considered as isolated scatterers in first approximation. When a normal

incident wave propagating along –*z* direction with x-polarized electric field impinges this structure, the electric field polarizes the nanorods which are along x-direction Thus, mainly the scattering from this set of x- oriented nanorods causes a field enhancement die to the Rayleigh anomaly. Therefore, this field enhancement further enhances the field of those oligomers with axis along x-axis. For the case of *y*-polarized incident field, the nanorods in the *y*-direction would be mostly responsible for the field enhancement due to the Rayleigh anomaly. Any polarization in between, would polarize both the set of nanorods (since the incident field can be decomposed into its *x* and *y* components). The most important point of this discussion is that, when only one set of nanorods is present, only oligomers parallel to the nanorods benefit from the further enhancement provided by Rayleigh anomaly [15]. However, when both sets of nanorods are present, the direction of the axis of oligomers doesn't play any role and the oligomers would benefit from the further field enhancement from both sets nanorods. As previous chapters, FE indicates the ability of a system to enhance the electric field locally with respect to the incident illuminating field. As was mentioned before, since the coupling between the oligomers and the nanorods is negligible, the total field enhancement achieved by the two-scale structure can be approximate with the product of field enhancement obtained by periodic nanorods and the oligomers individually.

To illustrate the ability of Rayleigh anomaly in enhancing the field, we consider a 2D periodic array of nanorods made of gold (we use Drude model in our full-wave simulations) as shown in Fig. 5-1 with diameter d_r = 80 nm, and period p_r = 800 nm along both the *x* and *y* directions; for the moment we assume the oligomers are not present. The incident field is normal to the plane of periodicity with parameter φ showing the angle of the electric field with the *x*-axis. As first case we assume the substrate is vacuum, i.e., ε_{sub} = 1. Full-wave simulation based on the finite element method (FEM) implemented in CST Studio suite results are used to evaluate the field enhancement in the middle of a unit cell versus free-space wavelength. Field enhancement peaks when the wavelength is equal to the period p_r = 800 nm. The maximum of the enhancement as was shown in [15] is equal to 2. In Fig. 5-2.b, the substrate is assumed to be glass with

ε_{sub}=2.25 and the period is assumed to be p_r = 900 nm. Note that the maximum happens at a wavelength smaller than the period because of the presence of the substrate. Also, its value is less than 2, since the reflection from the substrate interferes with the constructive scattering from the nanorods, reducing the field enhancement value.

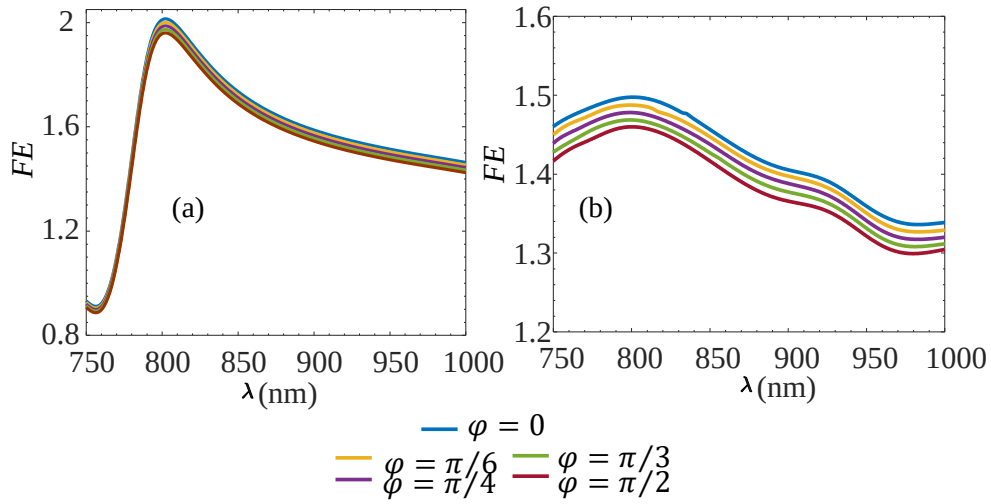

Fig. 5-2. Electric field enhancement (FE) achieved in the middle of a unit cell of a 2D periodic array of gold nanorods excited by a normally incident plane wave polarized along an angle φ with respect to the *x* axis: (a) in a vacuum host medium, (b) over a glass substrate.

The maximum of constructive scattering occurs in the middle of the unit cell, i.e. where we are monitoring the field in Fig 5-2. Although the field enhancement peaks exactly in the middle of four crossing nanorods, the field remains high in almost all the space between the four nanorods. In Fig. 5-3 we show how the value of the field varies between two adjacent nanorods in one direction (the *x* distance is normalized to the period) versus φ (angle of polarization of the incident electric field). In Fig. 5-3 the field is evaluated at middle of the unit cell in the *y*-direction (*y*=0), versus *x*, for the same configuration of Fig. 5-2 (a), and three angles represent the electric field polarization along φ =0 ^{o}, φ =45^{o} and φ =90^{o}. Two important results may be taken from this figure. The first observation is that, although maximum *FE* happens

exactly in the middle, *FE* is still higher than 1 for a very good part of the space in middle of unit cell. The next observation is that, polarization of light interacts with the set of nanorods which are parallel to it. In other words, when the electric field is along the *x* direction, φ =0 °, nanorods along the x-axis (with periods along y) are those who interfere constructively. This can be simply understood by comparing φ =90° and φ =0 ° results. For φ =0 ° the field is almost constant as we move along the *x* direction since the polarization of the incident field is perpendicular to the nanorods along y-axis, meaning that only nanorods along the x direction are those who contribute in making the Rayleigh anomaly (due to the symmetry, moving along the *x* direction does not change the value of *FE*). However, for ϕ=90° case, the field varies significantly varying *x* since as we got farther from the middle, the interference of scattered waves becomes more destructive. Variation of *FE* for ϕ=45° case is something in the middle of the aforementioned cases, since this polarization excites both set of nanorods.

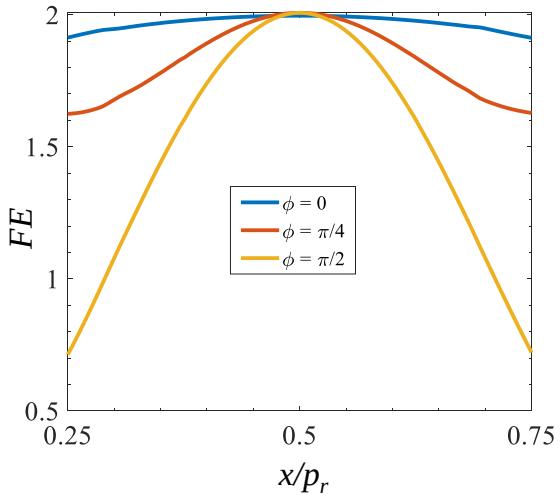

Fig. 5-3. Electric field enhancement (*FE*) achieved by a 2D periodic array of gold nanorods in free space, at the middle of unit cell in the *y* direction, versus *x* position. The maximum field enhancement happens at the middle of unit cell, and it is flatter for incident polarization along φ = 0°, i.e., along the *x* direction. Rods diameter is d_r = 80 nm and period p_r =900nm.

So far, we only demonstrated the ability of a 2D periodic array of nanorods in enhancing the field. Next, in Fig. 5-4 we show the FE when we combine a 2D periodic set of nanorods with the oligomers to

find the *FE* of the proposed 2D two-scale structure and compare it with using oligomers alone in providing field enhancement. We use the same configuration as in Fig. 5-1, with diameter of nanorods d_r = 80nm, period of nanorods p_r =900nm, diameter of spheres d_s = 80 nm with gap g = 0.9nm. The substrate is glass with ε_{sub} = 2.25 and polarization is along φ=0. In Fig. 5-4 we monitor the field in the hotspot of a dimer located at the center of a unit cell. The field enhancement of the oligomers alone is shown with a red curve whereas the *FE* of the 2D two-scale is shown with a yellow-solid curve. As one can observe, the *FE* provided by the proposed 2D two-scale structure is always higher than the one achieved with oligomers alone. *FE* achieved with nanorods (Rayleigh anomaly) is shown in the subset of the figure. The importance of this further Rayleigh anomaly-induced field enhancement is made clear in applications like SERS where the strength of the signal is proportional to the fourth power of the electric field.

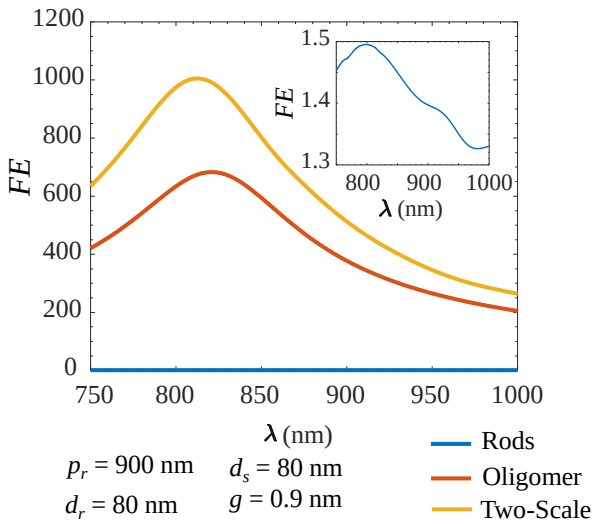

Figure 5-4. Electric field enhancement versus wavelength of incident light generated by an individual gold dimer (red line) and by the combination of a 2D periodic array of nanorods and dimer, i.e., the proposed 2D two-scale structure (yellow line). Field enhancement is calculated in the dimer hotspot via full-wave simulations. The structure is located on a glass substrate, with vacuum above.

In the last part of the paper, we turn our attention to the case of oblique incidence of light. To that end, in Fig. 5-5 we assume that the angle θ between the wavevector k and the z axis is greater than zero

(zero is the case for normal incidence) and study the field enhancement in the middle of the unit cell for the configuration of Fig. 5-4 with the exception that here we assume two different cases of $\theta = \pi/3$ and $\theta = 7\pi/12$. Based on Rayleigh anomaly equation, for normal incidence, maximum happens only for one wavelength (for each specific p integer) since $\cos(\pi/2) = 0$, however, for other angles of incidence, two peaks are observed from Rayleigh anomaly equation. The same result can be inferred from full-wave FEM simulations reported in Fig. 5-5 where two peaks appear for each angle of incidence.

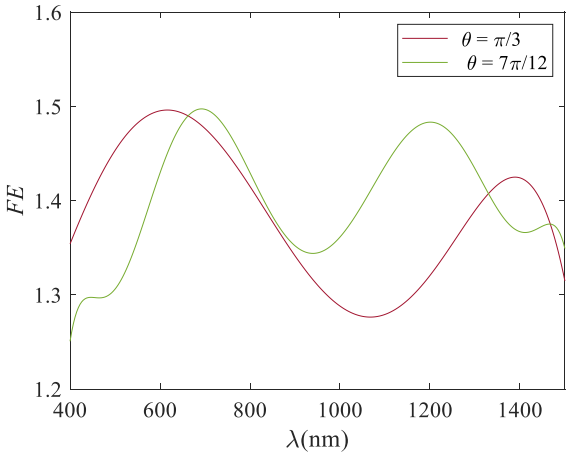

Fig. 5-5. Field enhancement for configuration of Fig. 4 for two oblique incidences of $\theta = \pi/3$ and $\theta = 7\pi/12$. As was implied from Rayleigh anomaly equation, instead of one peak which occurs in the normal incidence case, two peaks occur for each angle of incidence.

Sec. 5.3 Conclusion

In conclusion, in this paper we have introduced the concept of Rayleigh anomalies in a 2D periodic grid interacting with the plasmonic resonances of colloidal oligomers as a new avenue for providing additional field enhancement. Indeed, the additional field provided by Rayleigh anomaly could be as strong as 2, however, substrate has negative effect on *FE* in the cases studied, reducing the maximum achievable *FE*. We expect these two-scale substrates to find several applications in medical diagnostics, solar cells, sensors, and single molecule detectors. A preliminary version of this concept has been experimentally validated for a 1D periodic array of nanorods [15],

leading to almost an order of magnitude field enhancement in Raman scattering, the experimental verification of the polarization insensitive FE method described in this paper is subject of future studies.

CHAPTER 6 : MAGNETIC NANOANTENNAS MADE OF PLASMONIC NANOCLUSTERS FOR PHOTOINDUCED MAGNETIC-FIELD ENHANCEMENT

Sec. 6.1 Motivation

The magnetic interaction of light and matter is weaker than its electric counterpart at optical frequencies[155]–[158]. Due to this reason, achieving resonant magnetism in the optical regime has become the focus of attention in the physics and engineering communities[159]–[165]. The overall magnetism of a metamaterial (i.e., relative magnetic permeability different from unity) is tailored by engineering the artificial magnetic resonance in "meta-atoms"[166], [167]. For instance, engineered metamaterials with magnetic response was demonstrated in[168]–[172]. Split ring resonators (SRR) are the most explored building blocks in engineering artificial magnetism at the microwave spectrum[173]–[176]. Moreover, in [177]–[180], it is shown that by tuning the dimensions of SRR and by implementing a precise fabrication, the magnetic resonance at near infrared and visible frequencies, is achievable. In[181]–[184] using effective medium theory, a three-dimensional collection of polaritonic, nonmagnetic spheres have been shown to produce negative permeability at terahertz and infrared frequencies. Furthermore, other structures such as the spherical constellations[185]–[189], composite medium made of arrays of dielectric spheres[190], a periodic lattice of clusters comprising four silver plasmonic dimers[191] have been used to make metamaterial constituents which provide magnetic polarization in the visible and infrared spectrum.

Circular clusters made of plasmonic nanoparticles, which are of interest in this chapter, not only can provide engineered negative permeability[192], but also they can be used to achieve Fano resonances[193]–[196], [49], and as magnetic nanoprobes enhance light matter interaction[197], [198] at optical frequencies.

Conventionally, plasmonic nanoantennas are utilized at optical frequencies owing to their exotic property of enhancing the electric field. However, here I relate to the important quest to enhance magnetic field instead of the electric field [199]. In this chapter, inspired by these referenced studies, I focus on the specific category of plasmonic nanoantennas made of circular clusters and focus on the enhancement of magnetic field. I refer to these antennas as magnetic nanoantennas or magnetic nanoprobes in the rest of the thesis. Magnetic nanoantennas can be useful for enhancing quantum magnetic transitions in molecules which are in general overshadowed by the electric ones [200]–[203], [197], [198]. The magnetic resonance in a cluster of plasmonic nanoparticles corresponds to a dark resonance, i.e., a resonance that is neither easy to excite nor easy to measure its scattered field, which have higher quality factor and narrower bandwidth than the bright electric resonance counterpart. In [202], a cluster of six silver nanospheres has been studied under azimuthally polarized beam which selectively excites the dark resonance of the cluster with attention to the magnetic field enhancement and to the local field admittance of the scattered near-field. However, to the best of the authors' knowledge, the exploration of the best clusters for magnetic field enhancement and the amount or surface area where such enhancement occurs is still lacking in the literature as well as a simple analytic formula that estimates the magnetic resonance frequency, given here for the first time.

Hence, in this chapter I investigate properties of different clusters of gold nanospheres, such as dimers, trimers, tetramers, pentamers, hexamers, and octamers in a host dielectric medium (e.g., glass or a general solution). Plasmonic gold nanoparticles have applications in medical diagnostics [204], [205], sensing [206]–[209] and imaging [210] in the optical spectrum because of moderately low-loss compared to several other metals and also they are one of the least reactive chemical elements. Our goal is to investigate how magnetic nanaoantennas made of gold are able to create a magnetic dominant region in which the magnetic field is enhanced over a certain surface area where the electric field ideally vanishes. Specific figures of merit (the magnetic field enhancement and the normalized local field admittance) are defined and used for that purpose as explained in the next Section.

Sec. 6.2 Statement of the problem

I consider clusters of gold nanospheres with various numbers of elements, relative permittivity ε_m in a host medium with relative permittivity ε_h, shown in Fig. 6-1. For the purpose of stressing the capabilities of magnetic nanoantennas in boosting quantum magnetic transitions in matter that are overshadowed by electrical ones, I define two figures of merit [202]: the magnetic field enhancement and the magnetic to electric field ratio, i.e. the normalized local field admittance:

$$F_H = \frac{\left|\mathbf{H}^t(\mathbf{r})\right|}{\left|\mathbf{H}^i(\mathbf{r})\right|} \tag{6.1}$$

$$F_Y = \eta \frac{\left|\mathbf{H}^t(\mathbf{r})\right|}{\left|\mathbf{E}^t(\mathbf{r})\right|} \tag{6.2}$$

Here, $\left|\mathbf{H}^t(\mathbf{r})\right|$ and $\left|\mathbf{E}^t(\mathbf{r})\right|$ are the magnitude of total magnetic and electric fields at position $\mathbf{r}$, and $\left|\mathbf{H}^i(\mathbf{r})\right|$ is the magnitude of incident magnetic field at the same position, respectively. The magnetic field enhancement (F_H) indicates the ability of a magnetic nanoantenna to enhance the magnetic field with respect to the incident one. The normalized magnetic to electric field ratio, i.e., the normalized local field admittance (F_Y), shows the ability of a magnetic nanoantenna to enhance the magnetic field relatively to the total electric field, normalized to the field impedance $\eta = \sqrt{\mu_0 / (\varepsilon_0 \varepsilon_h)}$ of a plane wave in the same host medium. Large local field admittance in a region shows the magnetic nanaoantenna succeeds in generating a magnetic dominant region, and $F_Y > 1$ means that the magnetic to electric field ratio is larger than that of a plane wave.

Scattering from magnetic nanoantennas is characterized using two types of illuminations: (i) a single plane wave, (ii) two counter-propagating plane waves with anti-symmetric electric field with respect to the cluster symmetry plane (*y-z* plane in Fig. 6-1) to have a vanishing electric field at the center where a

maximum of incident magnetic field occurs. The symmetry of illumination can be further augmented using azimuthally polarized beams with longitudinal magnetic field on their axis [202], [211], [212] whose field disposition matches perfectly to the magnetic mode of the clusters characterized by the rotationally symmetrical circulating electric dipole moments about the cluster center. The two counter-propagating plane waves excitation is preferred over azimuthally polarized beam illumination solely due to its instant availability and relaxed computation resource requirements in commercial electromagnetic full-wave simulation software packages.

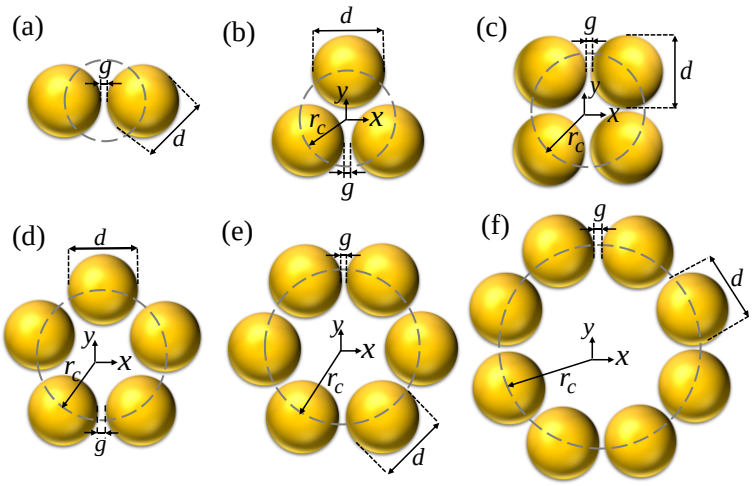

Fig. 6-1. Plasmonic clusters with varying number of nanospheres: (a) dimer, (b) trimer, (c) tetramer, (d) pentamer, (e) hexamer, and (f) octamer. r_c is the cluster radius and g is the gap between nanoparticles with diameter d.

The cluster types used in our investigation, namely dimers, trimers, tetramers, pentamers, hexamers and octamers are illustrated in Fig.6-1. In all structures, the diameter of the nanospheres is "d" and the gap between them is "g". For a cluster made of N spheres, each sphere is centered at the corners of a regular polygon whose circumscribed circle has radius r_c called here the cluster radius, given by

$$r_c = \frac{d+g}{2\sin(\pi/N)} \tag{6.3}$$

In this thesis, the monochromatic time harmonic convention $\exp(-i\omega t)$ is implicitly assumed and the notation is suppressed. In all equations, bold fonts are used for vector quantities in phasor domain, and a bar under a bold font is used for dyadic quantities. Unit vectors are bold with a hat on top.

Sec. 6.3 Analytic formulation

I apply the single dipole approximation (SDA) method to model clusters of nanoparticles[213], [214]. It means I model each nanosphere with a single electric dipole moment $\mathbf{p}$. The electric dipole moment of the nth nanosphere at location $\mathbf{r}_n$ is found by

$$\mathbf{p}_n = \alpha \mathbf{E}^{loc}(\mathbf{r}_n) \tag{6.4}$$

where α is the electric polarizability of the nanosphere, assumed to be isotropic and $\mathbf{E}^{loc}(\mathbf{r}_n)$ is the local electric field at the nth nanosphere's location which is the summation of the incident field and the field scattered by all the other nanospheres of the cluster. The electric polarizability of the nanospheres is here given by its Clausius-Mossotti expression with the correction term that accounts for the radiation[213]

$$\alpha = \pi \varepsilon_0 \varepsilon_h d^3 \left(2\frac{\varepsilon_m + 2\varepsilon_h}{\varepsilon_m - \varepsilon_h} - i\frac{(kd)^3}{6} \right)^{-1} \tag{6.5}$$

where ε_h is the relative permittivity of the host medium, ε_0 is the vacuum permittivity, d is the diameter of the nanosphere, $k = k_0\sqrt{\varepsilon_h}$ is the host medium wavenumber and k_0 is the wavenumber in vacuum. The gold nanosphere is described by its relative permittivity ε_m given here by the Drude model as

$$\varepsilon_m = \varepsilon_\infty \left[1 - \frac{\omega_p^2}{\omega(\omega + i\gamma)} \right] \tag{6.6}$$

where ε_∞ is the high-frequency fitting parameter, ω_p is the plasma frequency and γ is the damping factor. For gold, I assume $\varepsilon_\infty = 9.5$, $\omega_p = 4.4124\times10^{15}$ rad/s, and $\gamma = 1.05\times10^{14}$ rad/s [215].

The total electromagnetic fields at an arbitrary observation point $\mathbf{r}_{obs}$ is given by[216]

$$\mathbf{E}^t(\mathbf{r}_{obs}) = \mathbf{E}^i(\mathbf{r}_{obs}) + \sum_{n=1}^{N} \underline{\mathbf{G}}(\mathbf{r}_{obs}, \mathbf{r}_n) \cdot \mathbf{p}_n \tag{6.7}$$

$$\mathbf{H}^t(\mathbf{r}_{obs}) = \mathbf{H}^i(\mathbf{r}_{obs}) + \sum_{n=1}^{N} \frac{ck^2}{4\pi} \frac{e^{ikr}}{r} \left(1 - \frac{1}{ikr}\right) (\hat{\mathbf{r}}_{obs} \times \mathbf{p}_n) \tag{6.8}$$

where c is the speed of light in the host medium, and $\underline{\mathbf{G}}(\mathbf{r}_{obs}, \mathbf{r}_n)$ is the dyadic Green's function defined as

$$\underline{\mathbf{G}}(\mathbf{r}_{obs}, \mathbf{r}_n) = \frac{e^{ikr}}{4\pi\varepsilon_0\varepsilon_h} \left[\left(\frac{k^2}{r} + \frac{ik}{r^2} - \frac{1}{r^3} \right) \underline{\mathbf{I}} - \left(\frac{k^2}{r} + \frac{3ik}{r^2} - \frac{3}{r^3} \right) \hat{\mathbf{r}}\hat{\mathbf{r}} \right] \tag{6.9}$$

In Eq. (6.8) and Eq. (6.9), $r = |\mathbf{r}|$ with $\mathbf{r} = \mathbf{r}_{obs} - \mathbf{r}_n$, where $\mathbf{r}_n$ is the source dipole location and $\underline{\mathbf{I}}$ is the 3×3 identity dyad.

The overall electric dipole and overall magnetic dipole moments of a cluster of N nanospheres with the cluster center at the origin are defined as [49]

$$\mathbf{p} = \sum_{n=1}^{N} \mathbf{p}_n, \quad \mathbf{m} = \frac{-i\omega}{2} \sum_{n=1}^{N} \mathbf{r}_n \times \mathbf{p}_n \tag{6.10}$$

respectively.

According to Eq.(6.7) and Eq.(6.8) , to calculate the electric and magnetic field, the induced electric dipole for each sphere needs to be found. In doing so, I need to construct and solve a linear system of equations in terms of the induced dipole moments and the external excitation field. The local electric field $\mathbf{E}^{loc}(\mathbf{r}_n)$, is given by

$$\mathbf{E}^{loc}(\mathbf{r}_n) = \mathbf{E}^i(\mathbf{r}_n) + \sum_{\substack{m=1 \\ m \neq n}}^{N} \underline{\mathbf{G}}(\mathbf{r}_n, \mathbf{r}_m) \cdot \mathbf{p}(\mathbf{r}_m) \tag{6.11}$$

By writing Eq. (6.4) and Eq. (6.11) for $n = 1, ..., N$, I can construct the linear system

$$\left[A\right]\begin{bmatrix}\mathbf{p}_1\\ \vdots\\ \mathbf{p}_N\end{bmatrix}=\begin{bmatrix}\alpha\mathbf{E}^i(\mathbf{r}_1)\\ \vdots\\ \alpha\mathbf{E}^i(\mathbf{r}_N)\end{bmatrix} \tag{6.12}$$

where $\left[A\right]$ is a $3N\times 3N$ matrix made of 3×3 sub-blocks $\underline{\mathbf{A}}_{nm}$, with $n,m\in\{1,\ldots,N\}$, given by

$$\underline{\mathbf{A}}_{nm}=\begin{cases}\underline{\mathbf{I}} & m=n\\ -\alpha\underline{\mathbf{G}}(\mathbf{r}_n,\mathbf{r}_m) & m\neq n\end{cases} \tag{6.13}$$

As mentioned earlier, one of the goals of this thesis, is to sort the magnetic nanoantennas based on their quality factor associated to the magnetic resonance, that depends on both material and radiation losses that are accounted for by using the dynamic Green's function (Eq.(6.9)). One way to calculate the quality factor of each cluster, is to find the cluster natural frequencies. To do so, I need to solve Eq. (6.12) for ω when $\mathbf{E}_i=0$. One has non-trivial solutions to such a system only when

$$\det\left[\underline{\underline{\mathbf{A}}}(\omega)\right]=0 \tag{6.14}$$

In general, solving Eq. (6.14) for ω, gives complex frequencies. One way to calculate the natural frequencies is solving Eq. (6.14) numerically. Under certain approximations one can also obtain analytical formulas of resonance frequencies. Similarly, in [217] authors applied SDA to calculate the natural frequency of a dimer of particles made of metallic nanoshell and dielectric core for symmetric and anti-symmetric conditions. In the next section, I study only the rotationally symmetric magnetic resonance case by simplifying the Eq. (6.14) to a scalar equation and for the first time I provide a simple approximate formula to estimate the natural frequency and quality factor of clusters with an arbitrary number of metal nanospheres.

A. Magnetic resonance frequency

Owing to the rotational symmetry associated to a magnetic resonance in a cluster, each nanosphere induces a circulating displacement current resulting in the rotationally symmetric electric dipole moment disposition shown in Fig. 6-2. This resonance generates the overall longitudinal magnetic dipole moment of

the cluster provided in Eq. (6.10). Therefore, owing to symmetry, I reduce the system in Eq. (6.12) made of $3N$ equations to a single scalar equation. This is because each sphere has identical induced electric dipole moment amplitude p_φ and polarized along the $\hat{\boldsymbol{\varphi}}_n$ direction as $\mathbf{p}_n = p_\varphi \hat{\boldsymbol{\varphi}}_n$. Thus, the local electric field at the nth nanosphere is written as $\mathbf{E}^{loc}(\mathbf{r}_n) = (p_\varphi / \alpha)\ \hat{\boldsymbol{\varphi}}_n$. So, Eq. (6.11) is written as

$$(p_\varphi / \alpha)\ \hat{\boldsymbol{\varphi}}_n - \sum_{\substack{m=1 \\ m \neq n}}^{N} \underline{\mathbf{G}}(\mathbf{r}_n, \mathbf{r}_m) \cdot p_\varphi \hat{\boldsymbol{\varphi}}_m = \mathbf{E}^i(\mathbf{r}_n) \tag{6.15}$$

Natural frequencies are solution of Eq. (6.15) without excitation wave ($\mathbf{E}^i = 0$). By dividing all vector terms in Eq. (6.15) by $\alpha^{-1} p_\varphi$ and projecting the vectors in Eq. (6.15) on $\hat{\boldsymbol{\varphi}}_n$ I obtain

$$1 - \sum_{\substack{m=1 \\ m \neq n}}^{N} \alpha\ \hat{\boldsymbol{\varphi}}_n \cdot \underline{\mathbf{G}}(\mathbf{r}_n, \mathbf{r}_m) \cdot \hat{\boldsymbol{\varphi}}_m = 0 \tag{6.16}$$

In Sec. 4 the complex natural frequency solution of Eq. (6.16) are also calculated numerically.

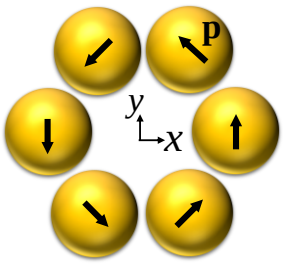

Fig. 6-2. The magnetic resonance has a symmetric disposition of electric dipoles along $\hat{\boldsymbol{\varphi}}$, producing a strong magnetic field at the center.

A closed form formula for the complex natural frequency is obtained by applying some approximations. The first assumption is that both nanospheres and their mutual distances are sub-wavelength. Therefore, it is possible to replace the dynamic terms in both the polarizability and the Green's functions by the electrostatic ones. Which means the quasi static solution is equivalent to the limiting case

where $k \to 0$ in Eq. (6.5) and Eq. (6.9), but keeping the correct frequency dependent dielectric constant ε_m in Eq. (6.9). The polarizability reduces to the Claussius-Mossotti relation [213]

$$\alpha \approx \alpha_0 = \frac{1}{2}\pi\varepsilon_0\varepsilon_h d^3\left(\frac{\varepsilon_m - \varepsilon_h}{\varepsilon_m + 2\varepsilon_h}\right) \tag{6.17}$$

The Green's function is approximated in the static regime as[214]

$$\underline{\mathbf{G}}(\mathbf{r}_n, \mathbf{r}_m) \approx \frac{1}{4\pi\varepsilon_0\varepsilon_h}\left[-\frac{1}{r_{nm}^3}\underline{\mathbf{I}} + \frac{3}{r_{nm}^3}\hat{\mathbf{r}}_{\mathbf{nm}}\hat{\mathbf{r}}_{\mathbf{nm}}\right] \tag{6.18}$$

By substituting Eq. (6.17) and Eq. (6.18) in Eq. (6.16), after some algebraic manipulation Eq. (6.16) is reduced to

$$\varepsilon_m = \frac{1+2L}{1-L}\varepsilon_h \tag{6.19}$$

where $L = \left(2r_c / d\right)^3 / T$, and

$$\begin{aligned} T = \sum_{\substack{m=1 \\ m\neq n}}^{N} \Bigg\{ & \left(\frac{r_c}{r_{nm}}\right)^3 \Big[\left(\frac{3A_{nm}}{D_{nm}} - 1\right)\sin\varphi_n \sin\varphi_m + \\ & -\frac{3B_{nm}}{D_{nm}}\sin(\varphi_n + \varphi_m) + \left(\frac{3C_{nm}}{D_{nm}} - 1\right)\cos\varphi_n \cos\varphi_m\Big]\Bigg\} \end{aligned} \tag{6.20}$$

In Eq. (6.20), A_{nm}, B_{nm}, C_{nm} and D_{nm} are the coefficients which relate the nth nanosphere to the mth one and are defined as

$$\begin{aligned} A_{nm} &= (\cos\varphi_n - \cos\varphi_m)^2 \\ B_{nm} &= (\cos\varphi_n - \cos\varphi_m)(\sin\varphi_n - \sin\varphi_m) \\ C_{nm} &= (\sin\varphi_n - \sin\varphi_m)^2 \\ D_{nm} &= A_{nm} + C_{nm} \end{aligned} \tag{6.21}$$

We are looking for complex natural angular frequency as $\omega = \omega' + i\omega''$. Substituting the Drude model for metal permittivity Eq. (6.6) into Eq. (6.19), and solving for ω, leads to the closed-form formula for complex natural angular frequency as

$$\omega' \approx \sqrt{\frac{\omega_p^2}{\varepsilon_\infty - \frac{1+2L}{1-L}\varepsilon_h} - \frac{\gamma^2}{4}}, \qquad \omega'' \approx -\frac{\gamma}{2} \tag{6.22}$$

Note that Eq. (6.22) reduces to the natural frequency reported in [218] that was obtained for the specific case with *N*=4 nanospheres.

It is important to note that with the quasi-static approximation, I neglect the radiation damping, therefore material loss (based on the Drude model) is the only remaining loss when evaluating these formulas. Since the natural frequency is complex, one can define the quality factor, as [219]

$$Q = -\frac{\omega'}{2\omega''} \tag{6.23}$$

A system with high quality factor provides a sharp resonance and strong overall magnetic dipole moment. According to the derived approximate formula for the natural frequency (Eq. (6.22)), I find an approximate formula for the quality factor of clusters with arbitrary number of nanospheres as

$$Q \approx \sqrt{\frac{\left(\omega_p/\gamma\right)^2}{\varepsilon_\infty - \frac{1+2L}{1-L}\varepsilon_h} - \frac{1}{4}} \tag{6.24}$$

where the number of nanospheres (N) is accounted for in the L parameter. In the next Section, I report the approximate (only material loss is considered) quality factor and natural frequency of the clusters of Fig. 6-1 with a comparison to the numerically found ones (both material loss and radiation loss are considered).

Sec. 6.4 Results and discussion

I address the effect of cluster parameters on the resonance frequency and on the two figures of merit F_H and F_Y introduced in Sec. 2. Studied structures include dimers, trimers, tetramers, pentamers, hexamers and octamers embedded in a host medium with relative permittivity $\varepsilon_h = 2.25$ (it could represent the permittivity of an environment consisting of a glass substrate and a solution).

In the following, the magnetic resonance frequency is calculated using two distinct methods: (i) by solving Eq. (6.14) for complex frequency, in two ways: numerically, when the electric polarizability in Eq. (5) is used (denoted by $f_r(I)$ in Table 1) and by using the closed formula solution obtained via the approximate analytical method introduced in Sec. 3 (denoted as $f_r(II)$ in Table 1), and (ii) by finding the purely-real resonance frequency defined as the frequency that renders the magnetic field enhancement F_H maximum at the cluster center under time harmonic excitation (resonance denoted by $f_r(III)$ in Table 1). In this latter case, I assume the cluster illuminated by a single plane wave with electric field polarized along the y-axis and magnetic field along *z*, as shown in Fig. 6-3 (a).

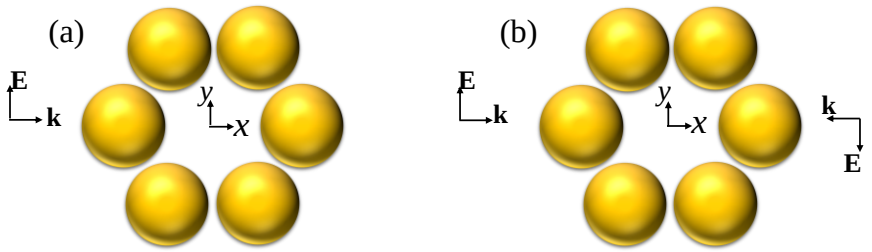

Fig. 6-3. Hexamer illuminated by (a) a single plane wave polarized along *y* axis, (b) a superposition of two counter-propagating plane waves with anti-symmetric electric field distribution with respect to the *y*-*z* plane, such that the electric field vanishes at the cluster center where a maximum of incident magnetic field is polarized along *z*.

In the reported comparisons of resonance frequencies calculated by different methods, I consider constant sphere diameter and gap in the clusters of Fig. 6-1 as 50 nm and 5 nm respectively. In fifth column of Table 1 I report F_H at the resonance frequency under single plane wave excitation. Finally, the quality factor Q based on the natural resonance frequency calculated numerically $f_r(I)$ and with the approximate formula $f_r(II)$ as in Eq. (6.22) are reported in the sixth and seventh columns of Table 1, respectively. Furthermore, to provide a clear comparison among the methods, I define the percentage error in the real part of frequencies calculated numerically ($f_r'(I)$) and analytically (by approximate formula) ($f_r'(II)$) relative to $f_r(III)$ as

$$|e_r|\% = \left| \frac{f_r'(I \text{ or } II) - f_r(III)}{f_r(III)} \right| \times 100 \tag{6.25}$$

For the clusters reported in Table 1, the relative error for natural frequency calculated numerically ($f_r'(I)$) and approximately ($f_r'(II)$), is always less than 1% and 10% respectively. The very good agreement between $f_r'(I)$ and $f_r'(III)$, is consistent with the high quality factor $Q(I)$, which means that the resonant mode is clearly excited and well defined even by single plane wave excitation (we recall that to purely excite the magnetic resonance, two counter propagating plane waves need to be used, otherwise the single plane wave excites also other cluster modes). Note also that our approximate formula Eq. (22) provides a good estimate of resonance frequency. Moreover, by looking at the magnetic field enhancement F_H and the quality factor Q calculated numerically and approximately, two things can be inferred, (i) our approximate formula for quality factor works as a tool to show how strong the magnetic nanoantenna enhances the magnetic field, (ii) as the number of elements in a cluster increases, the magnetic field enhancement at the cluster center, and the quality factor decrease.

As shown in the Appendix A, for a cluster with a number of nanospheres *N*, assuming the resonance is made of *N* induced electric dipole moments perfectly polarized along $\hat{\boldsymbol{\varphi}}$ as shown in Fig. 6-2, the ratio of scattered power to the absorbed power is proportional to $P^{scat} / P^{abs} \propto N / \sin^2(\pi / N)$. This means that when *N* increases, for the magnetic resonance in these clusters, the loss due to scattering (as a magnetic dipole) is larger than the loss in the nanospheres. Hence, when the cluster is enlarged by adding more nanospheres (whereas the diameter of each nanosphere and the gap between them is fixed), the quality factor calculated numerically ($Q(I)$) (which is based on both material and radiation loss) drops more rapidly than the one calculated approximately ($Q(II)$) (which is only based on material loss).

Table 1. Comparison of natural frequencies found with different methods and the quality factor of different clusters of gold nanospheres when *d*=50nm nm and *g*=5 nm

Cluster	$f_r(I)$ THz $f_r'+if_r''$	$f_r(II)$ THz $f_r'+if_r''$	$f_r(III)$ THz	F_H	$Q(I)$	$Q(II)$
$N=2$	566- i10 $\lvert e_r \rvert = 0.1\%$	564-i8 $\lvert e_r \rvert = 0.2\%$	566	9	28.6	33.8
$N=3$	538 - i10 $\lvert e_r \rvert = 0.2\%$	540 - i8 $\lvert e_r \rvert = 0.5\%$	537	6.7	26.6	32.3
$N=4$	513- i11 $\lvert e_r \rvert = 0.4\%$	523-i8 $\lvert e_r \rvert = 2\%$	511	7.1	22.6	31.3
$N=5$	494- i13 $\lvert e_r \rvert = 0.3\%$	513-i8 $\lvert e_r \rvert = 4\%$	492	6.5	18.9	30.7
$N=6$	479- i15 $\lvert e_r \rvert = 0.3\%$	506-i8 $\lvert e_r \rvert = 6\%$	477	5.8	15.6	30.3
$N=8$	456 -i21 $\lvert e_r \rvert = 1\%$	500-i8 $\lvert e_r \rvert = 10\%$	452	4.5	10.8	29.9

Next, in Fig. 6-4 I explore the effect of the nanospheres' diameter *d* and gap spacing *g* on the magnetic field enhancement F_H (evaluated at the cluster center at its resonance frequency) for the clusters shown in Fig. 6-1.

I excite each cluster with a single plane wave polarized along the *y*-direction as shown in Fig. 3(a). For each cluster the nanosphere diameter varies from 5 nm to 90 nm and the gap varies from 1 nm to 20 nm. Note that the resonance frequency is not constant when varying *d* and *g*, therefore in Fig. 6-4 I superimpose some of the iso-frequency contours denoting the resonance frequency at which F_H is given.

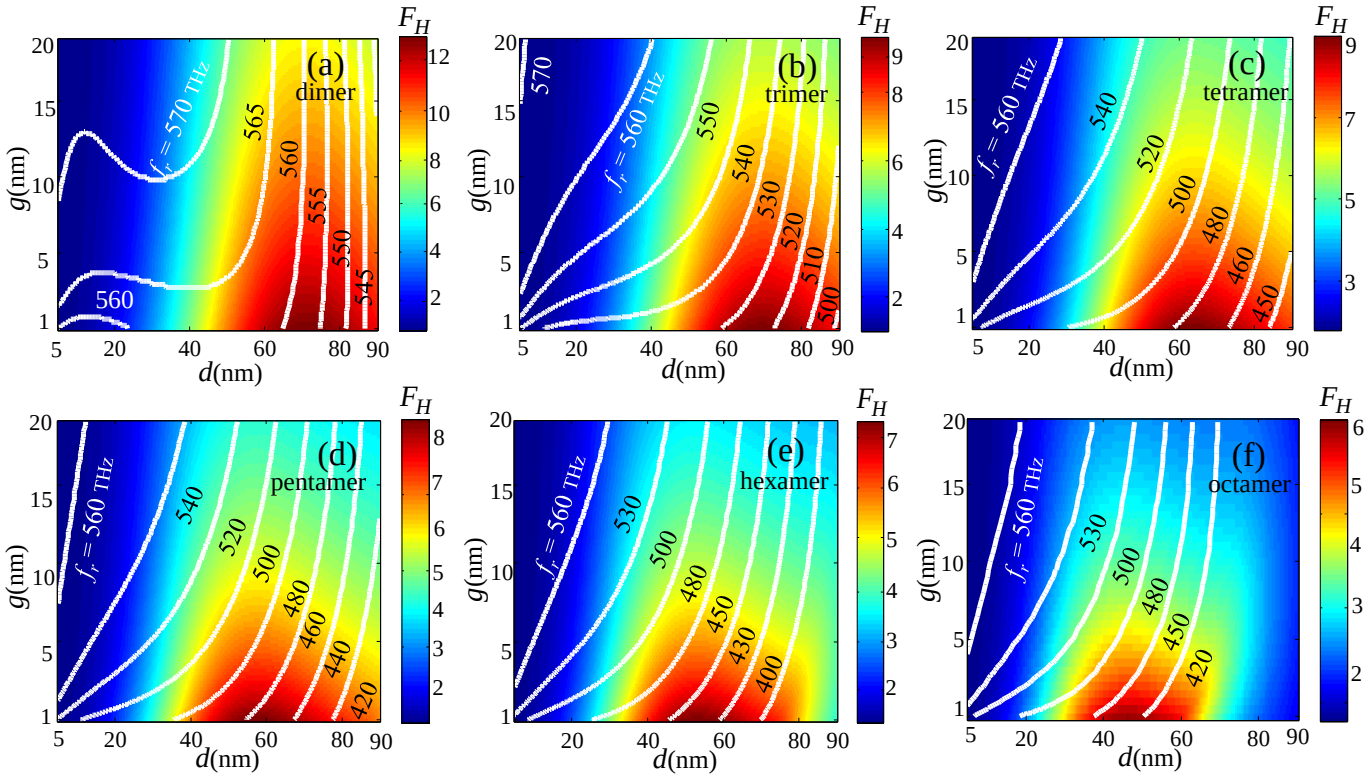

Fig. 6-4. Magnetic field enhancement F_H at the center of each cluster at its resonance frequency for: (a) dimer, (b) trimer, (c) tetramer (d) pentamer (e) hexamer (f) octamer. Nanospheres' diameter d and gap g vary between 5 and 90 nm and between 1 and 20 nm, respectively. Each cluster is excited by a single plane wave polarized along the y axis.

Results shown in Fig. 6-4 verify the important conclusion that as the cluster's number of nanospheres increases, the magnetic field enhancement at its center decreases. Furthermore, according to, for a given N and g, the magnetic field enhancement at the cluster center increases by increasing the nanosphere diameter, till it reaches a maximum for an optimum diameter, and if the diameter is further increased F_H decreases. Moreover, according to Fig. 6-4 for a given sphere diameter, F_H decreases by increasing the gap space between two adjacent nanospheres.

Fig. 6-5 shows the normalized local field admittance F_Y at the center of a hexamer evaluated at its resonance frequency, which depends on the varying parameters d and g. According to Fig. 6-5 the effect of

diameter and gap on the local field admittance at the center of hexamer, is the same as the magnetic field enhancement case, i.e. for a certain nanosphere diameter increasing the gap, causes decrease in F_Y and for a specific gap, increasing the diameter causes increase in F_Y till it reaches the optimum diameter after which by increasing the diameter, F_Y decreases. Another important conclusion from Fig. 6-5 is that with single plane wave excitation, the local field admittance at the cluster center is not large, which means with this type of excitation, the cluster is not able to create a strong magnetic dominant region. This is a motivation to change the excitation beam to superposition of two counter-propagating plane waves to eliminate the electric field at the cluster center and enhance the local field admittance, as shown in Fig. 6-10.

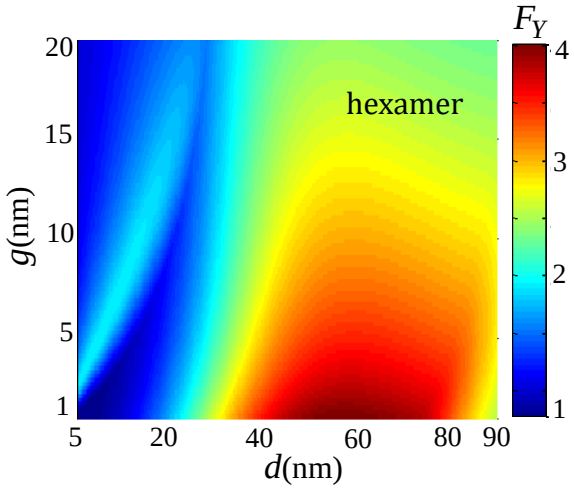

Fig. 6-5. Local field admittance (F_Y) at the center of a hexamer when *d* and *g* vary in the ranges 5-90 nm and 1-20 nm, respectively. The hexamer is excited by a single plane wave polarized along the *y* axis.

Since circular clusters produce circulating currents, the radius of the cluster plays an important role in characterizing the magnetic response. As it is clear from Fig. 6-4, for each cluster there are many pairs of *d* and *g* (but different cluster radius r_c) that yield the same resonance frequency and different magnetic field enhancement. To investigate the effect of cluster radius on the magnetic field enhancement (Fig. 6-6), I use Fig. 6-4 to extract information about resonating clusters at a certain resonance frequency (here I choose

480 THz, since most of the clusters have resonance at this frequency). Fig. 6-6 represents the magnetic field enhancement (F_H) at the cluster center versus radius of cluster (r_c) for clusters with various number of nanospheres which resonate at 480 THz. It is worth mentioning that for each cluster with specific number of nanospheres (*N*) resonating at 480 THz, there is an optimum cluster radius at which the magnetic field enhancement is maximized. Moreover, when the number of nanospheres in a cluster increases, the optimum radius of the cluster increases and its corresponding magnetic field enhancement reduces.

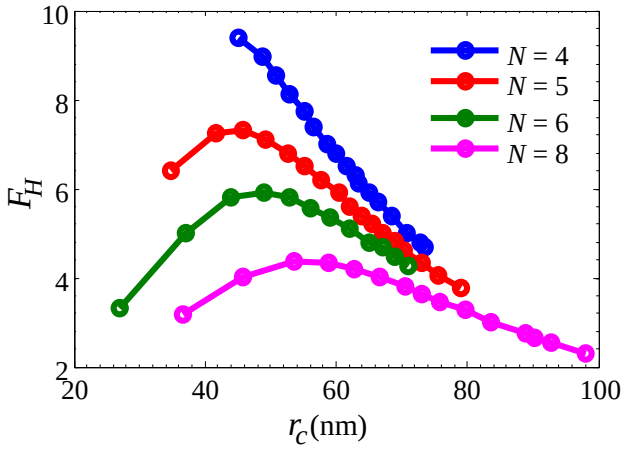

Fig. 6-6. Magnetic field enhancement (F_H) at the center of a cluster versus cluster's radius for different cases on particle numbers *N*. In all cases geometries are chosen so clusters resonate at 480 THz.

As mentioned earlier, to create a magnetic dominant region, one needs to establish symmetry conditions on both the cluster and the incident field such that the net electric response of the cluster is suppressed. The clusters I introduced so far are rotationally symmetric and host strong magnetic dipolar mode. Moreover, by applying two counter-propagating plane waves with anti-symmetric electric field distribution with respect to cluster symmetry plane (*y*-*z* plane in our structure) as shown in Fig. 6-3(b), the external electric field vanishes and due to the clusters rotational symmetry, no net electric field is created at the cluster center. This excitation method leads to strong electric field in the gap region between nanospheres and strong magnetic field at the cluster center. Our findings (for brevity details not shown here) show that for the clusters studied in this chapter, the magnetic field enhancement defined as in Eq. (1) does not depend on the excitation type, i.e., a single plane wave versus two counter-propagating plane waves as in Fig. 6-3

(b). With two counter-propagating plane waves illumination, for each cluster, I study the behavior of magnetic field enhancement, with respect to frequency, based on both the analytical formulation using SDA and full wave simulations. Full wave simulations are performed by the frequency domain finite elements method (FEM), implemented in the commercial software CST Microwave Studio by Computer Simulation Technology AG. Fig. 6-7 shows the magnetic field enhancement (F_H) versus frequency for clusters shown in Fig. 1, at the cluster center, by using SDA [Fig. 6-7 (a)] and full wave simulations [Fig. 6-7 (b)] when the diameter of each nanosphere and the gap spacing are kept constant as 50 nm and 5 nm, respectively and the clusters are excited by two counter-propagating plane waves as shown in Fig. 6-3 (b).

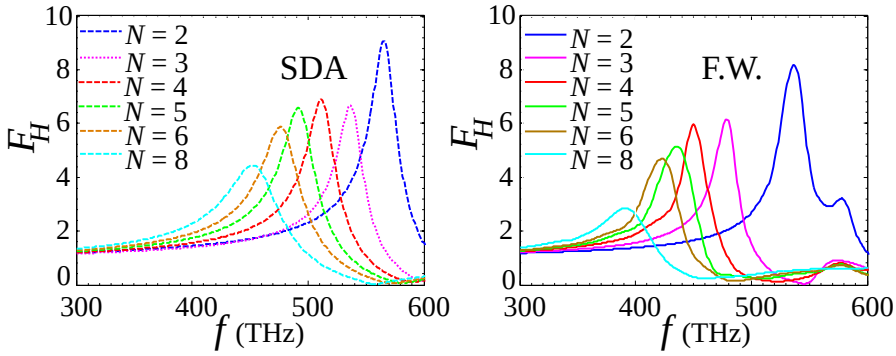

Fig. 6-7. Magnetic field enhancement at the cluster center versus frequency for different cluster sizes. Results are calculated via (a) SDA analysis and via (b) full wave (F.W.) simulations. In each case the cluster is excited by two counter-propagating plane waves as in Fig. 6-3 (b).

Fig. 6-7 confirms that both analysis methods lead to the same conclusion that enlarging the cluster by adding more nanospheres results in reducing the magnetic field enhancement at the cluster center, red shifting the resonance frequency and increasing the resonance line width. There is a slight difference between the resonance frequencies obtained with full wave simulation and those obtained with SDA (5% in the dimer case and increasing to 15% in the octamer case). SDA calculations also overestimate the magnetic field enhancement by 8% in the trimer case and up to by 50% in the octamer case. The difference between the results obtained with these two methods, grows as the number of nanospheres increases. This difference originates from the fact that in SDA I neglect the magnetic dipole moment of each nanosphere and also all

higher order multipoles, and by adding more nanospheres in a cluster, the effect is cumulative. To elaborate on this issue, I study also the absorption [Fig. 6-8 (a-b)], scattering [Fig. 6-8 (c-d)], and extinction [Fig. 6-8 (e-f)] cross sections of the clusters shown in Fig. 1 based on equations given in Appendix B. These cross sections are evaluated using both the SDA [Fig. 6-8 (a, c, e)] and full wave simulations [Fig. 6-8 (b, d, f)] assuming the diameter of each nanosphere and the gap spacing to be constant as 50 nm and 5 nm, respectively. In these simulations clusters are excited by two counter-propagating plane waves as shown in Fig. 6-3(b). In each plot, the cross sections are normalized to the geometrical cross section of a single nanosphere $\sigma_g = \pi(d/2)^2$. At the magnetic resonance, each cluster exhibits a peak in the absorption and scattering, and hence in the extinction cross section. Moreover, according to the cross sections specifically obtained by full wave simulations, I observe that adding more nanospheres in a cluster leads to larger cross section. Furthermore, since the scattering cross section is proportional to the total magnetic dipole moment of the cluster, as the number of nanospheres increases, stronger magnetic dipole moment is achieved. I used two counter-propagating plane waves excitation since it facilitates the simulation burden and it makes the electric dipole moment vanish. Higher order multipoles like the electric quadrupole are still present, though weak compared to the magnetic dipole since each of these simulations are carried out at the magnetic resonance frequency. Effects of the electric quadrupole are visible at higher frequencies in the simulations, analogously to what was shown in detail in Figs. 3-5 of[186] for spherical clusters. Note that higher order multipoles are not visible in the scattering cross section calculated with the SDA since it is evaluated in an approximate way (Eq. (A5) by considering only the scattering due to a magnetic dipole).

Results also confirm the trend already observed in Fig. 6-7: as I increase the number of the nanospheres in the cluster the results of the SDA diverge from those of full-wave simulations.

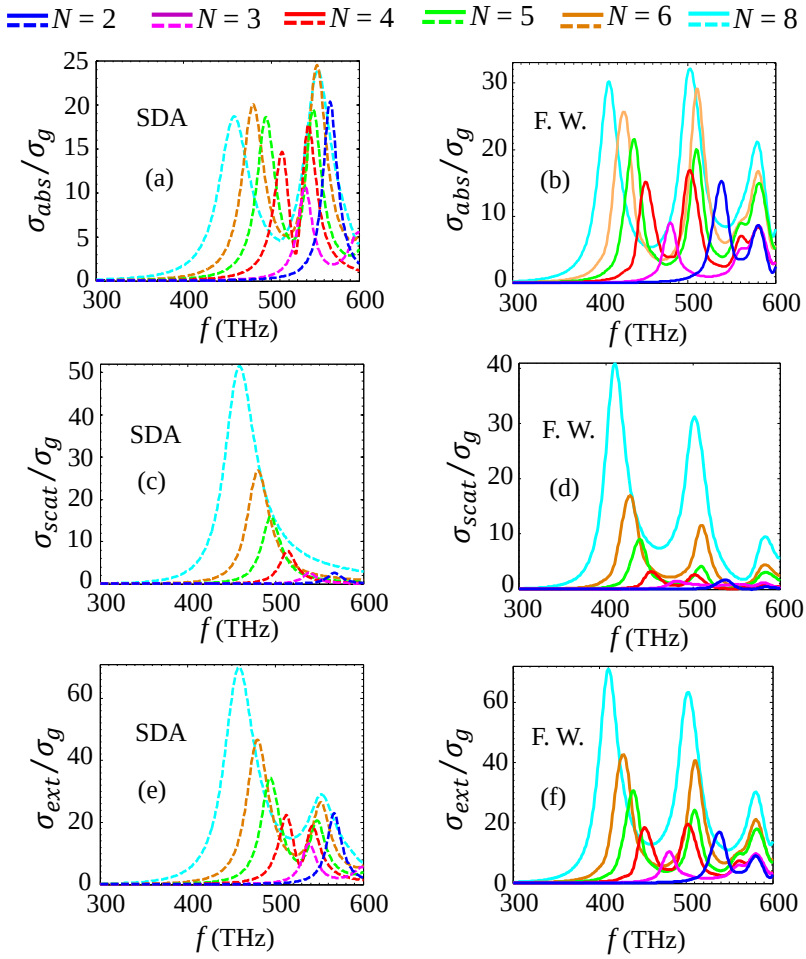

Fig. 6-8. Normalized absorption (a-b), scattering (c-d) and extinction (e-f) cross sections of clusters versus frequency, for different cluster sizes. Cross sections are normalized with respect to the geometrical cross section of a single nanosphere $\sigma_g = \pi(d/2)^2$. Results are calculated via SDA analysis (a, c, e) and via full wave (F.W.) simulations (b, d, f). In all cluster cases, the nanospheres' diameter and gaps are kept constant as 50 nm and 5 nm respectively. In each case the cluster is excited by two counter-propagating plane waves as in Fig. 6-3(b).

Although the magnetic field enhancement reduces at the cluster center as the cluster expands, to elaborate on the possible advantages of large clusters, I provide the magnetic field enhancement profile in the *x*-*y* plane for different clusters at their resonance frequency. Fig. 6-9(a-f) represents the magnetic field enhancement (F_H) profile in logarithmic scale (as $10\log_{10}(F_H)$ the color legend is saturated for the values more than 10.4) calculated using SDA analysis for clusters represented in Fig. 6-1 when the nanospheres' diameter and gap between them are kept constant as 50 nm and 5 nm respectively and the clusters are excited

by two counter-propagating plane waves as shown in Fig. 6-3(b), at their resonance frequency obtained from Fig. 6-7(a). According to Fig. 6-9, the magnetic field enhancement at the gap space between adjacent nanospheres is always strong and it is slightly stronger near the nanospheres rather than at the cluster center. Moreover, as the number of nanospheres in the cluster increases, the area with strong magnetic field becomes wider. According to Table 1 the quality factor decreases with size which results in the reduction of the magnetic field enhancement at the cluster center. Therefore, there is always a trade-off between getting the maximum magnetic field enhancement at a certain point such as the center of a cluster and having strong magnetic field over a wide area inside the cluster. Plots in Fig. 6-9 show also a strong magnetic field enhancement outside the cluster with the shape of two vertical bands (dark red bands with extraordinary large F_H). This is due to the specific excitation used in Fig. 6-9 with two counter-propagating plane waves shown in Fig. 6-3(b) that form a standing wave pattern of the incident magnetic field. There are two nulls with half a wavelength distance and result in locally huge magnetic field enhancement [202].

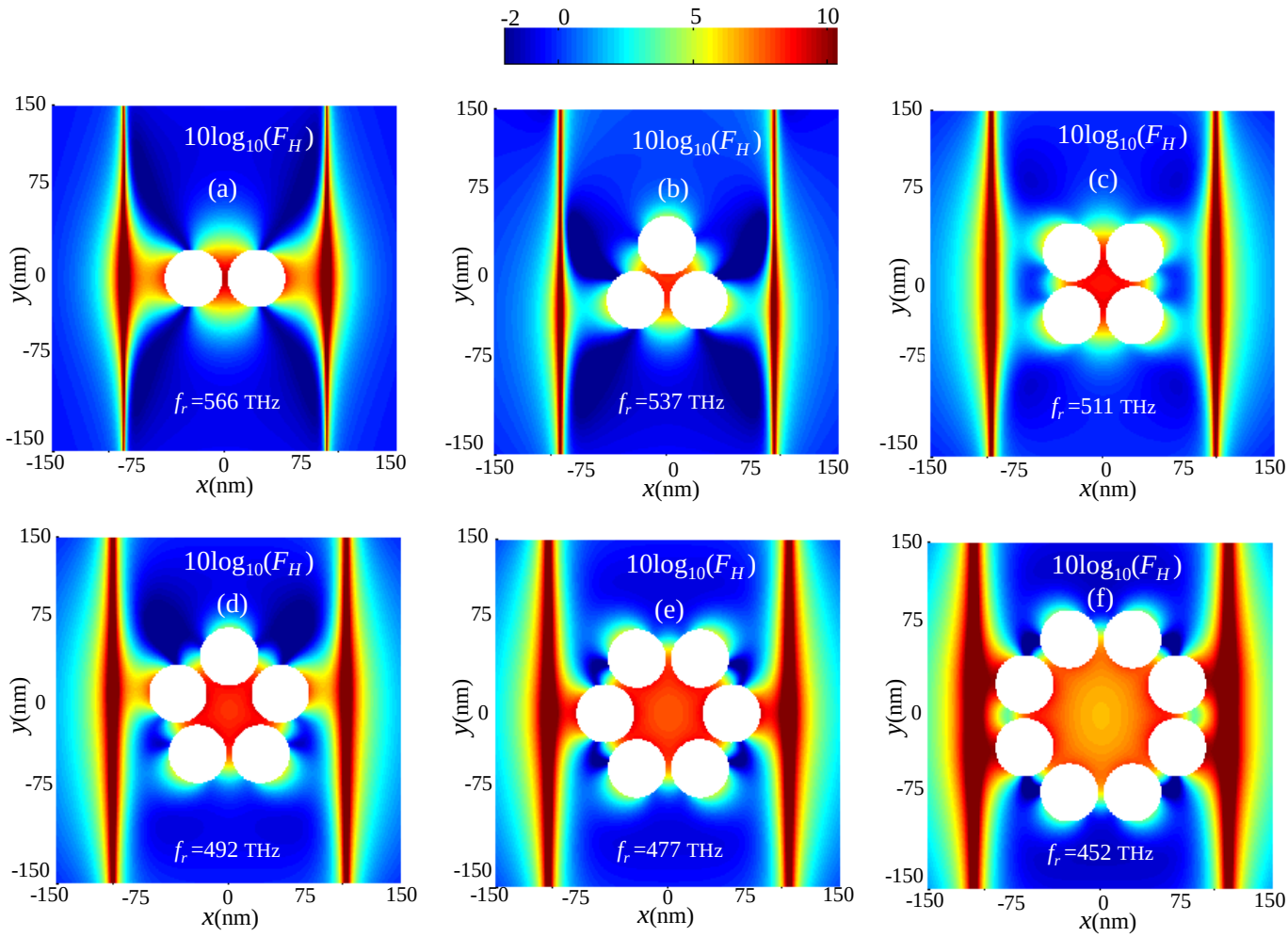

Fig. 6-9. Magnetic field enhancement (F_H) profile in logarithmic scale (as $10\log_{10}(F_H)$, the color legend is saturated for the values more than 10.4) of (a) dimer, (b) trimer, (c) tetramer, (c) pentamer, (d) hexamer, (e) octamer with $d = 50$ nm and $g = 5$ nm. Each cluster is excited with two counter-propagating plane waves with anti-symmetric electric field with respect to the *y*-*z* plane.

Furthermore, to demonstrate the advantage of the symmetric excitation method (as shown in Fig. 6-3 (b)) and to create the magnetic dominant region with low electric field, I investigate the local field admittance (F_Y) profile in the *x*-*y* plane when the clusters are excited with two counter-propagating plane waves as in Fig. 6-3 (b). Fig. 6-10(a-f) shows the local field admittance profile in logarithmic scale (the color legend is saturated for the values more than 4) calculated using SDA method for clusters shown in

Fig. 6-1 with fixed diameter and gap of 50 nm and 5 nm respectively, while the clusters are excited with two counter-propagating plane waves with anti-symmetric electric field with respect to the *y*-*z* plane.

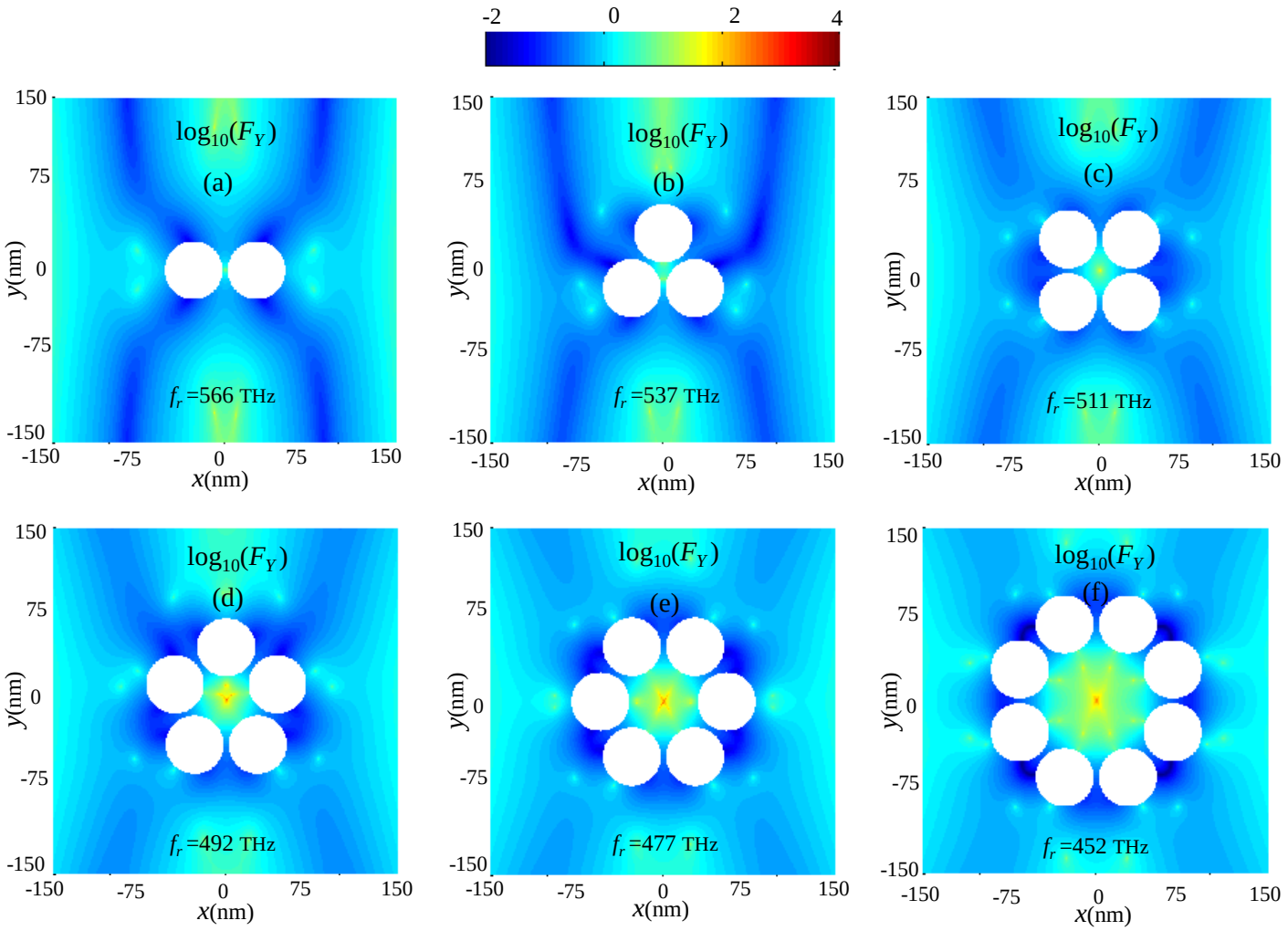

Fig. 6-10. The local field admittance (F_Y) profile of different clusters with *d*=50 nm and $g = 5$ nm, in logarithmic scale (the color legend is saturated for the values more than 4, i.e., for $F_Y > 10^4$) (a) dimer, (b) trimer, (c) tetramer, (d) pentamer, (e) hexamer, (f) octamer. Each cluster is excited with two counter-propagating plane waves with anti-symmetric electric field with respect to the *y*-*z* plane. Results show a large magnetic to electric field ratio around the center.

Owing to the two counter-propagating plane waves excitation shown in Fig. 6-3 (b), the incident electric fields cancel out exactly at the center of the cluster, so a giant local field admittance is expected at the center of each cluster. Moreover, enlarging the clusters by adding more nanospheres, leads to a wide area inside the cluster which possesses strong magnetic field (Fig. 6-9) and large field admittance (Fig.

6-10). In other words, there is a region of magnetic dominance. Furthermore, comparison of Fig. 6-10 (e) and Fig. 6-9 for the case of $d = 50$ nm and $g = 5$ nm, clearly shows that the level of local field admittance is much higher when the clusters are excited by a symmetric excitation.

Sec. 6.5 Conclusion

I have investigated clusters of gold nanospheres embedded in a host medium as magnetic nanoantennas to enhance the magnetic field at optical frequencies and I have shown how the electric field can be reduced at the cluster center. I sorted clusters based on their quality factor, the magnetic field enhancement and their ability to create a wide magnetic dominant region. I applied SDA to calculate the total magnetic and electric field at an arbitrary point while the clusters were illuminated by two different methods of excitation: (i) single plane wave and (ii) superposition of two counter-propagating plane waves to eliminate the electric field at the cluster center where the magnetic field is enhanced. I provided for the first time, a formula to approximate the natural frequency of clusters and their quality factor with arbitrary number of elements. I also, calculated the natural frequency and quality factor numerically and demonstrated the validity range of our proposed formulation. I defined two figures of merit to study the magnetic nanoantennas efficacy: (i) magnetic field enhancement (F_H) which shows the ability of the nanaoantenna to enhance the magnetic field and (ii) the local field admittance (F_Y) which shows how much the magnetic field is enhanced compared to the electric field. I verified our analytic results against full wave simulations and showed their consistency. The results indicated three facts about the clusters of nanospheres as magnetic nanoantennas: (i) increasing the number of elements in a cluster, leads to red shift in resonance frequency, decrease in quality factor and the level of magnetic field enhancement at the center of cluster whereas the area of magnetic dominant region increases; (ii) in each cluster, increasing the diameter of spheres first causes stronger enhancement and there is an optimum diameter after which the enhancement reduces by further increasing the diameter. (iii) increasing the gap spacing in a cluster, causes less magnetic

field enhancement at the cluster center. According to our study, clusters of gold nanospheres, because of their symmetry, when illuminated by a symmetric excitation are good magnetic nanoantennas with large magnetic to electric field ratio at the center.

APPENDIX A: Radiated and absorbed power by the cluster

I assume that for a resonating cluster with *N* nanospheres, the magnetic resonance has a symmetric disposition of electric dipoles as shown in Fig. 6-2. Hence all the N electric dipoles are polarized along the $\hat{\boldsymbol{\varphi}}$ direction and have equal magnitude p_φ. According to [220], [221], the absorbed time-average power in the nth nanosphere of the cluster is

$$P_n^{abs} = \frac{\omega\varepsilon_0\varepsilon_h}{2}\left[\frac{\mathrm{Im}(\alpha)}{\varepsilon_0\varepsilon_h} - \frac{k^3}{6\pi(\varepsilon_0\varepsilon_h)^2}|\alpha|^2\right]|\mathbf{E}^{loc}(\mathbf{r}_n)|^2 \tag{A26}$$

where α is the polarizability of each nanosphere given in Eq. (5). Moreover, since I assume that at resonance $\mathbf{E}^{loc}(\mathbf{r}_n) = (p_\varphi/\alpha)\,\hat{\boldsymbol{\varphi}}_n$, Eq. (A1) reads

$$P_n^{abs} = -\frac{\omega}{2}\left[\mathrm{Im}\left(\frac{1}{\alpha}\right) + \frac{k^3}{6\pi\varepsilon_0\varepsilon_h}\right]|p_\varphi|^2 \tag{A27}$$

Owing to the circular symmetry of the dipoles' strength, the total cluster power lost due to absorption is

$$P^{abs} = \sum_{n=1}^{N} P_n^{abs} = -\frac{\omega N}{2}\left[\mathrm{Im}\left(\frac{1}{\alpha}\right) + \frac{k^3}{6\pi\varepsilon_0\varepsilon_h}\right]|p_\varphi|^2 \tag{A28}$$

According to Eq. (10), and because of the symmetry of the magnetic resonance, the overall magnetic dipole moment of the cluster with N nanospheres when the cluster center is at the origin is

$$\mathbf{m} = -\frac{i\omega}{2} r_c p_\varphi N\,\hat{\mathbf{z}} \tag{A29}$$

where r_c is the radius of the cluster, defined in Eq. (6-3). The scattered power by the cluster is evaluated as the power scattered by a magnetic dipole moment leading to [222]

$$P^{scat} = \frac{\omega}{2}\frac{k^3\mu_0^2}{6\pi\varepsilon_0\varepsilon_h}\frac{|\mathbf{m}|^2}{\eta^2} \tag{A30}$$

where I have neglected the power contributions associated to higher order multipoles. By substituting Eq. (A4) into Eq. (A5), the total scattered power by the cluster is

$$P^{scat} = \frac{\omega^5}{48\pi}k\varepsilon_0\varepsilon_h\mu_0^2 r_c^2 N^2 \mid p_\varphi \mid^2 \tag{A31}$$

If I assume that in a cluster with N nanospheres, the diameter of each nanosphere and the gap between them is kept constant when varying N, by substituting the expression for the cluster radius in Eq. (6.3) into Eq. (A6), the ratio of scattered power by a cluster to the absorbed power is

$$\frac{P^{scat}}{P^{abs}} = \frac{N}{\sin^2(\pi/N)}\frac{\omega^4}{96\pi}\frac{k\varepsilon_0\varepsilon_h\mu_0^2(d+g)^2}{-\left[\mathrm{Im}\left(\frac{1}{\alpha}\right)+\frac{k^3}{6\pi\varepsilon_0\varepsilon_h}\right]} \tag{A32}$$

Moreover, one can substitute the Drude model permittivity provided in Eq. (6.6), into the electric polarizability (Eq.(6.5)), then the ratio of the scattered power by a cluster to the absorbed power is written as

$$\frac{P^{scat}}{P^{abs}} = \frac{N}{\sin^2(\pi/N)}Z \tag{A33}$$

where

$$Z = \frac{\omega^3\varepsilon_0^2\varepsilon_h\mu_0^2 k\pi d^3(d+g)^2}{576}\left\{\frac{[\omega^2(\varepsilon_\infty-\varepsilon_h)-\varepsilon_\infty\omega_p^2]^2}{\gamma\varepsilon_\infty\omega_p^2}+\frac{\gamma^2\omega^2(\varepsilon_\infty-\varepsilon_h)^2}{\gamma\varepsilon_\infty\omega_p^2}\right\} \tag{A34}$$

APPENDIX B. Absorption, scattering and extinction cross section

According to [223], the absorption, scattering and extinction cross sections are defined as

$$\sigma_{abs} = \frac{\sum_{n=1}^{N} P_n^{abs}}{S^i}, \qquad \sigma_{scat} = \frac{P^{scat}}{S^i} \tag{B1}$$

and $\sigma_{ext} = \sigma_{abs} + \sigma_{scat}$. Here P_n^{abs} and P^{scat} are calculated using Eq. (A1) and Eq. (A5), and $S^i = \frac{\eta}{2}|\mathbf{H}^i|^2$, where $|\mathbf{H}^i|$ is the magnitude of the total incident magnetic field exciting the cluster meta-particle. Note that I am focusing on the magnetic dipole excitation of a cluster that is seen here as a single scattering and absorbing meta-particle. Indeed, scattering of a particle described by its magnetic dipole is proportional to $|\mathbf{m}|^2 = \left|\alpha_m^{eff}\mathbf{H}^i\right|^2$ (α_m^{eff} is the effective magnetic polarizability of the cluster meta-particle) as shown in Eq. (A5), and its absorption is proportional to $\mathrm{Im}\{\mathbf{m}\cdot\mathbf{H}^{i*}\} \propto |\mathbf{H}^i|^2$, where the asterisk * denotes complex conjugation. This case is analogous to that of a particle described by its electric dipole absorption and scattering that would be proportional to $S^i = \frac{1}{2\eta}|\mathbf{E}^i|^2$. Note that in our simulations where I use an excitation made of two counter-propagating plane waves (as shown in Fig. 6-3(b)), S^i defined above is equivalent to $S^i = 4\hat{\mathbf{k}}^{pw}\cdot\frac{1}{2}\mathrm{Re}\{\mathbf{E}^{pw}\times\mathbf{H}^{pw*}\} = 4\frac{\eta}{2}|\mathbf{H}^{pw}|^2$, where $\hat{\mathbf{k}}^{pw}$ is normalized wavevector of either plane wave and $\mathbf{E}^{pw}$ and $\mathbf{H}^{pw}$ are its electric and magnetic fields. For the case of two counter-propagating plane waves considered in Fig. 6-3 (b) I have $\mathbf{H}^i = 2\mathbf{H}^{pw}$ and $\mathbf{E}^i = 0$ at the cluster center where I assume the equivalent magnetic dipole is located.

CHAPTER 7 : MAGNETIC FIELD ENHANCEMENT AT NANOSCALE: A COMPARATIVE STUDY

Sec. 7.1 Motivation

In chapter 6, I focused on a specific class of magnetic nanoantennas namely nanoclusters for which clusters of nanospheres are used to create a magnetic dipole moment which in turn enhances the magnetic field locally. These types of structures are made of plasmonic particles. However, plasmonic structures are known to be affected by unavoidable losses in metals in optical frequencies. This inherent problem of metals can be avoided by using subwavelength dielectric particles with high permittivity which are providing a new paradigm to constitute building blocks of novel nanostructures for magnetic field enhancement [21], [22], [243], [23]–[25]. Unlike plasmonic antennas where oscillations of the free electron plasma and collective lattice vibrations dictate the local response of the light-matter interaction, dielectric antennas rely on the fields and displacement currents induced in the antenna structure.

In this chapter, I discuss the choice of material, structure, shapes and arrangements that can create a highly enhanced magnetic field in the optical regime. Specifically, I study different metallic and dielectric structures to enhance the local magnetic field and compare their performance under similar condition. Moreover, I employ a structured beam as an excitation to achieve maximum magnetic to electric field enhancement. Specifically, I turn my attention to vector beams with cylindrical symmetry, or so-called vortex beams, which are experimentally functional in the selective excitation of Mie resonances in dense dielectric particles[25], [26]. A particular cylindrically symmetric vector beam category useful for selective excitation of the magnetic dipolar moment is the azimuthally electric-polarized vector beam (APB), which

hosts a strong longitudinal magnetic field along the beam axis where electric field vanishes [236], [248] and it has been used to excite magnetic dipoles[249], [250], [17].

The structures I study include cluster of gold nanospheres, cluster of gold nanopillars, gold triabolo and a silicon shell, all placed over a glass substrate with permittivity 2.25, while being excited by APB with the beam waist[251] as w_0=0.7λ in the corresponding excitation frequency . I design the parameters for each structure such that all of them have magnetic resonance in near infrared region around λ=800nm to be suitable for investigating magnetic dipole transition of trivalent lanthanides.

Sec. 7.2 Plasmonic magnetic nanoantennas

The first structure that I investigate is a cluster of six gold nanospheres (hexamer) as shown in Fig. 7-1(a). The diameter of each nanosphere is 120 nm and the gap between two adjacent ones in the cluster is 10 nm. The gold nanosphere is described with its relative permittivity ε_m given by the Drude model[252]. When excited by an APB, due to cylindrical polarization of the electric field, each sphere forms an azimuthally directed electric dipole, and the collection of dipoles make a circular electric current in the azimuthal direction which is equivalent to a magnetic dipole along z-direction (normal to the cluster plane) [17], [19]. In the near field of a magnetic dipole, magnetic field is much stronger than electric field and this used in a variety of recent research directions. In Fig. 7-1 (b) I have illustrated the magnetic field enhancement at the center of the cluster varying the excitation wavelength. Full-wave simulations are performed by the frequency-domain finite-element method implemented in COMSOL Multiphysics. As one can infer, this magnetic nanoantenna is able to enhance the magnetic field more than 3.5-fold at 780 nm. Fig 1.(c) and 1 (d), demonstrate the profile of F_Y and F_Y , in the x-y plane passing through the middle of cluster, at the magnetic resonance wavelength of the cluster respectively (780 nm). The strongest normalized field admittance F_Y occurs on the center of the cluster, thanks to the vanishing electric field component of the APB and the rotational symmetry of the nanocluster. As it is shown in [19] if I increase the number of

nanospheres in the cluster, the area with strong magnetic field becomes wider, however, it results in the reduction of the magnetic field enhancement at the cluster center.

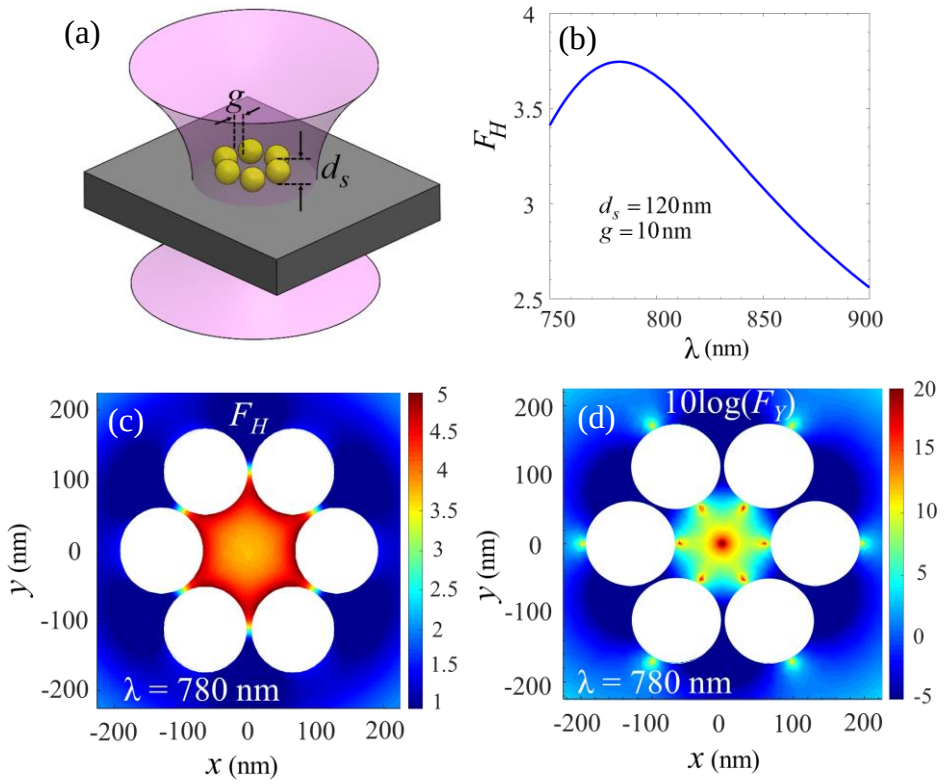

Fig. 7-1. (a) Cluster of gold nanospheres on top of a glass substrate, excited with the APB illuminated from the glass side. (b) The magnetic field enhancement at the center of cluster vs. excitation wavelength. (c) The magnetic field enhancement (F_H) profile and (d) The local field admittance (F_Y) at the resonance wavelength at the *x*-*y* plane crossing the middle of cluster. In (d), F_Y is shown in the logarithmic scale [as $10\log_{10}(F_Y)$, the color legend is saturated for the values more than 20]. In (c) and (d), white circles show the nanospheres cross section with the observation plane.

The next structure is cluster of six gold nanopillars as is shown in Fig. 7-2 (a). For each pillar, the diameter and height is 95 nm and 90nm, respectively and the gap between two adjacent pillars is 15 nm in the cluster, so the cluster resonates at 780 nm. Under APB excitation, the pillars form an azimuthal electric current which is equivalent to a magnetic dipole in the center of the cluster. The magnetic field enhancement

in the cluster center versus excitation wavelength, and profile of F_H and F_Y at the resonance wavelength in the *x-y* plane passing through the middle of cluster are shown in Fig. 7-2 (b), (c) and (d), respectively. By comparing this structure with cluster of nanospheres one can observe that they both resonate at the same wavelength and although the gap spacing is larger in the cluster of nanopillars, but the magnetic field enhancement is slightly higher. Moreover, in terms of design of clusters, pillars have one degree of freedom more than spheres to tune the resonance wavelength. However, their fabrication is challenging and limited to the resolution of electron beam lithography or focused ion beam methods.

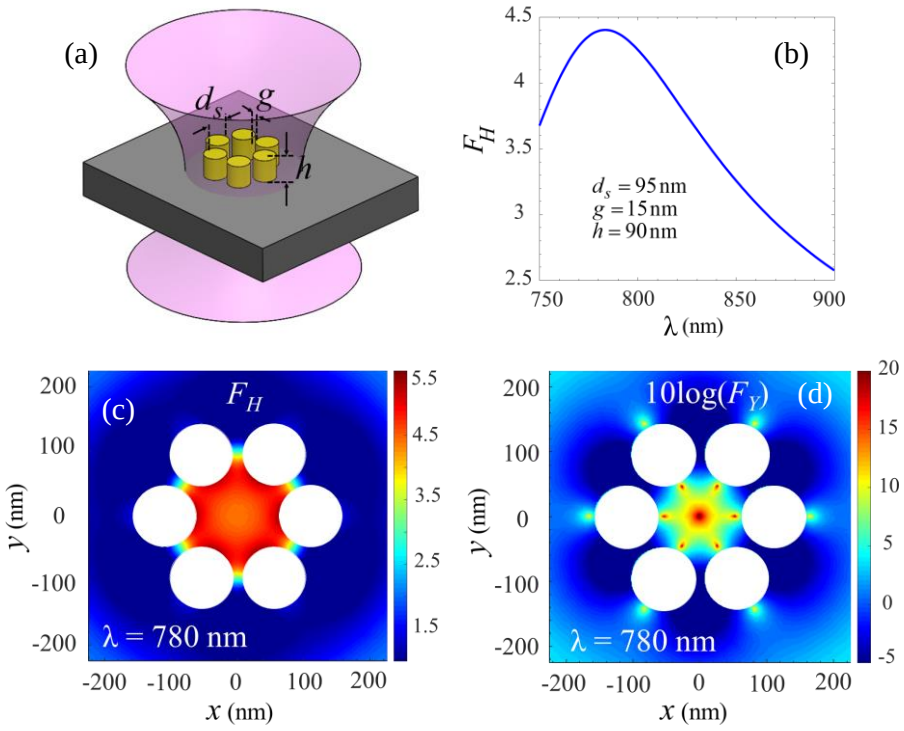

Fig. 7-2. (a) Cluster of gold nanopillars on top of a glass substrate, excited with the APB illuminated from the glass side. (b) The magnetic field enhancement at the center of cluster vs. excitation wavelength. (c) The magnetic field enhancement (F_H) profile and (d) the local field admittance (F_Y) at the resonance wavelength at the *x-y* plane crossing the middle of cluster. In (d), F_Y is shown in the logarithmic scale [as $10\log_{10}(F_Y)$, the color legend is saturated for the values more than 20]. In (c) and (d), white circles show the nanopillars cross section with the observation plane.

The last plasmonic structure that I investigate here is a gold triabolo. The ability of plasmonic diabolo structure to enhance the magnetic field at visible and infrared wavelength has been explored recently [15], [237], [13], [233], [238]. Here, by modifying the diabolo structure, I add some circular symmetry to it. As a result, when excited with an APB, the symmetry of structure helps to generate additional circular electric current and therefore provides stronger longitudinal magnetic dipole. A triabolo consists of three planar metal triangles attached together through their facing tips. The side of each equilateral triangle (shown with s in Fig. 7-3(a)) is 150 nm and the side of joint face (small equilateral triangle in the middle, shown with g) is 50 nm whereas the thickness of this structure is 100 nm. This structure is placed over a glass substrate and is illuminated with an APB from the bottom as shown in Fig. 7-3 (a). The magnetic field enhancement versus wavelength evaluated 5 nm above the center of triabolo, as well as the profile of F_H and F_Y in the x-y plane, 5 nm above the triabolo structure, at 810 nm are given in Fig 3 (b) , (c) and (d), respectively. As one can predict, magnetic field is enhanced between the main triangles and around the joint of triangles since the electric current is strong on the joint. However, the field admittance is maximum at center of structure mainly because of the APB characteristics. Although this structure is successful in providing magnetic field enhancement in the near-IR region, but its enhancement is weaker compared to other proposed structures in this chapter. This kind structure can be easily used also at lower frequencies.

Before turning our attention to the last magnetic nanoantenna, it is worth mentioning that, as it is well-known, all of the aforementioned metallic nanostructures provide giant electric field in the gaps between adjacent nanoparticles. Based on Babinet's principle (with some approximation, since this structure has finite thickness), complementary structures to the investigated ones, should provide strong magnetic field in the gap between adjacent nanoparticles.

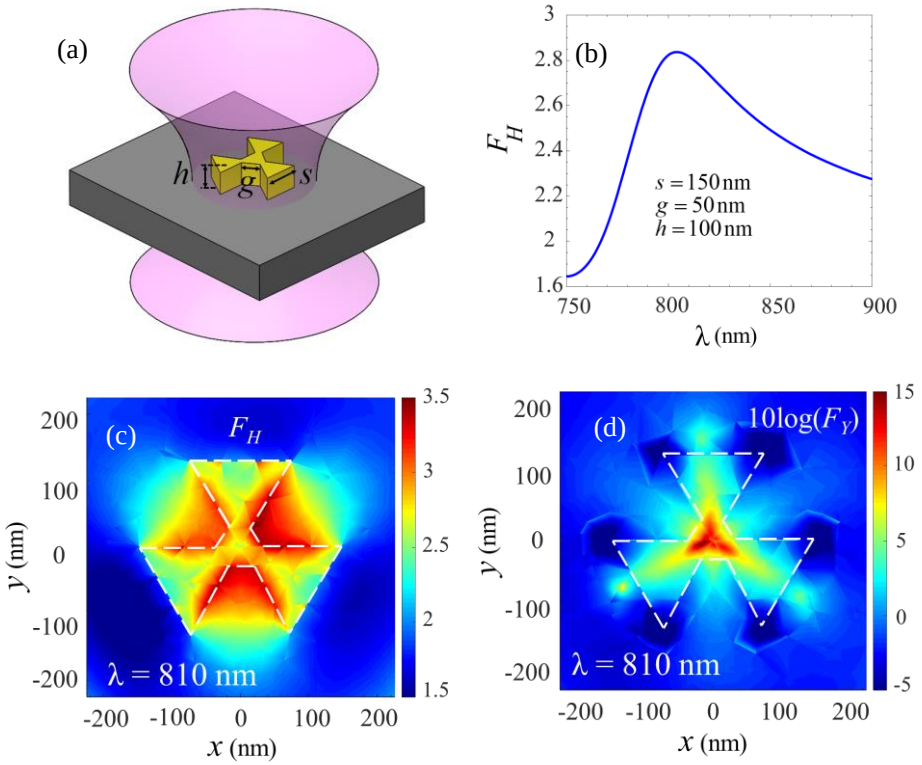

Fig. 7-3. (a) Gold triabolo on top of a glass substrate, excited with the APB illuminated from the glass side. (b) The magnetic field enhancement vs. excitation wavelength at 5 nm above the center of triabolo. (c) The magnetic field enhancement (F_H) profile and (d) the local field admittance (F_Y) at the resonance wavelength at the *x*-*y* plane 5 nm above the triabolo structure. In (d), F_Y is shown in the logarithmic scale [as $10\log_{10}(F_Y)$, the color legend is saturated for the values more than 20].

Sec. 7.3 Dielectric nanoantenna

Next, I show that high-index dielectric nanoantennas are a great alternative to their plasmonic counterpart as a way to enhance the magnetic response at optical regime. Indeed, when a high- refractive index dielectric is excited at its resonance, a strong electric displacement current is generated inside it. This displacement current can be used to form a magnetic dipole for magnetic field enhancement[239]–[243], [25]. In [25], I previously analytically and experimentally investigated the ability of a silicon disk illuminated by an APB to enhance the magnetic field at optical frequencies. However, in order to make a strong magnetic field "inside" the disk, accessible for magnetic dipole emitters, it may be useful to make a hollow nanodisk[18], [228], [244]. The geometry of a silicon hollow disk is shown in Fig.7-4. The outer

and inner diameters of the hollow disk are 250 and 100 nm, respectively whereas the height is 175 nm and it is placed over a glass substrate. Under APB illumination, the circulating displacement current which is formed in the hollow disk azimuthally, makes a magnetic dipole along the axis of the disk which enhances the magnetic response in the near-field. In Fig. 7-4 (b) I demonstrate the magnetic field enhancement versus wavelength at the center of the hollow disk. As one can observe, the maximum magnetic field enhancement is 5.3 which is higher than all the plasmonic structures that I have studied at this wavelength range. This is probably related to the larger volume hosting field displacement currents and not necessarily to lower losses in the silicon structure compared to its plasmonic counterparts since the linewidth is comparable to the previous examples. Moreover, I have shown the profile of F_H and F_Y in the *x*-*y* plane crossing the center of the hollow disk in Fig 7-4 (b) and Fig. 7-4 (c). As expected the admittance is maximum on the axis of the hollow disk for symmetry reasons, of both the nanoantenna and the illumination.

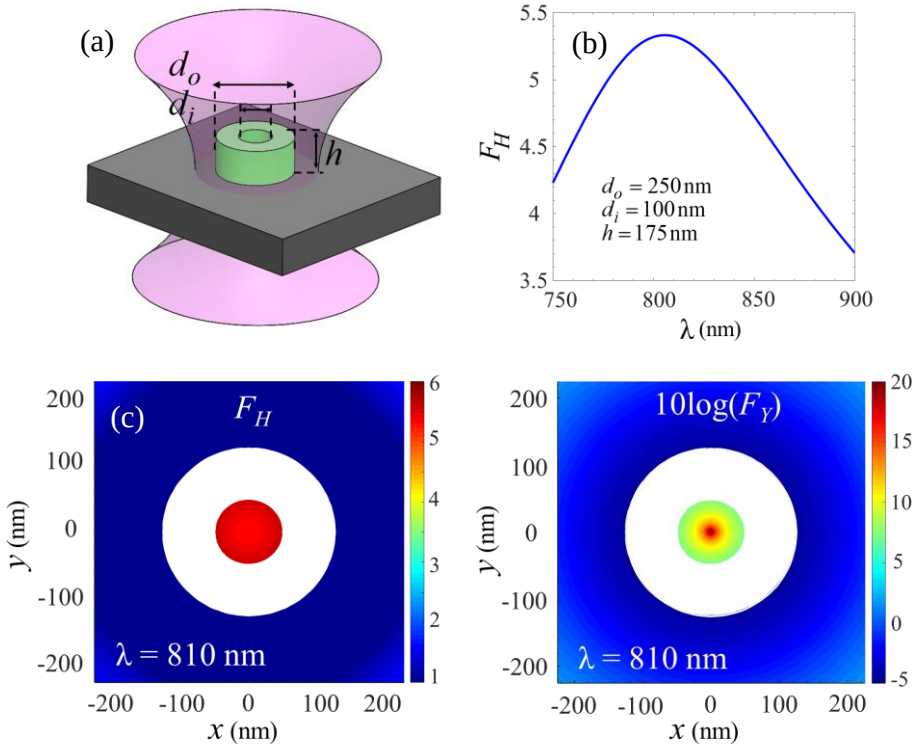

Fig. 7-4. (a) Silicon hollow disk on a glass substrate excited with an APB illuminated from glass side (b) The magnetic field enhancement vs excitation wavelength at the center of hollow disk. (c) The magnetic field enhancement

(F_H) profile and (d) the normalized field admittance (F_Y) profile in the *x*-*y* plane passing through the center of hollow disk at the resonance wavelength of disk (810 nm). In (d) F_Y is shown in the logarithmic scale [as $10\log_{10}(F_Y)$, the color legend is saturated for the values more than 20]. In (c) and (d), white area indicates the hollow disk.

Sec. 7.4 Conclusion

In conclusion, I demonstrated the ability of various plasmonic and a dielectric nano-engineered structures to enhance the magnetic field under a vortex beam illumination in near-IR region. Because of rotational symmetry the magnetic field at the center area of these nanoantennas are 10-100 times stronger than the electric field there, which illustrates the efficacy of these nanoantennas to enhance magnetic field when illuminated with the APB. In all case I have utilized the azimuthally polarized beam as excitation because its rotational symmetry facilitates the excitement of azimuthal electric current in rotationally symmetric antennas that led to a dominant magnetic field region at the center of the nanoantennas. These antennas act as magnetic nanoprobes and are useful to detect magnetic dipole transitions in molecules and in lanthanides, and to enhance the magnetic part of light in chirality detection.

REFERENCES

[1] G. M. Hwang, L. Pang, E. H. Mullen, and Y. Fainman, "Plasmonic Sensing of Biological Analytes Through Nanoholes," *IEEE Sens. J.*, vol. 8, no. 12, pp. 2074–2079, Dec. 2008.

[2] G. Lu *et al.*, "Plasmonic Sensing via Photoluminescence of Individual Gold Nanorod," *J. Phys. Chem. C*, vol. 116, no. 48, pp. 25509–25516, Dec. 2012.

[3] S. Campione, S. M. Adams, R. Ragan, and F. Capolino, "Comparison of electric field enhancements: Linear and triangular oligomers versus hexagonal arrays of plasmonic nanospheres," *Opt. Express*, vol. 21, no. 7, pp. 7957–7973, Apr. 2013.

[4] M. Torabzadeh, I.-Y. Park, R. A. Bartels, A. J. Durkin, and B. J. Tromberg, "Compressed single pixel imaging in the spatial frequency domain," *J. Biomed. Opt.*, vol. 22, no. 3, p. 030501, Mar. 2017.

[5] K. Nakayama, K. Tanabe, and H. A. Atwater, "Plasmonic nanoparticle enhanced light absorption in GaAs solar cells," *Appl. Phys. Lett.*, vol. 93, no. 12, p. 121904, Sep. 2008.

[6] K. X. Wang, Z. Yu, S. Sandhu, V. Liu, and S. Fan, "Condition for perfect antireflection by optical resonance at material interface," *Optica*, vol. 1, no. 6, pp. 388–395, Dec. 2014.

[7] M. Scalora *et al.*, "Second- and third-harmonic generation in metal-based structures," *Phys. Rev. A*, vol. 82, no. 4, p. 043828, Oct. 2010.

[8] M. Kamandi, C. Guclu, T. S. Luk, G. T. Wang, and F. Capolino, "Giant field enhancement in longitudinal epsilon-near-zero films," *Phys. Rev. B*, vol. 95, no. 16, p. 161105, Apr. 2017.

[9] M. A. Vincenti, M. Kamandi, D. de Ceglia, C. Guclu, M. Scalora, and F. Capolino, "Second-harmonic generation in longitudinal epsilon-near-zero materials," *Phys. Rev. B*, vol. 96, no. 4, p. 045438, Jul. 2017.

[10] J. B. Pendry, "Negative Refraction Makes a Perfect Lens," *Phys. Rev. Lett.*, vol. 85, no. 18, pp. 3966–3969, Oct. 2000.

[11] *Principles of Surface-Enhanced Raman Spectroscopy*. Elsevier, 2009.

[12] T. Pakizeh, M. S. Abrishamian, N. Granpayeh, A. Dmitriev, and M. Käll, "Magnetic-field enhancement in gold nanosandwiches," *Opt. Express*, vol. 14, no. 18, pp. 8240–8246, Sep. 2006.

[13] Y. Yang, H. T. Dai, and X. W. Sun, "Fractal diabolo antenna for enhancing and confining the optical magnetic field," *AIP Adv.*, vol. 4, no. 1, p. 017123, Jan. 2014.

[14] P. Albella *et al.*, "Low-Loss Electric and Magnetic Field-Enhanced Spectroscopy with Subwavelength Silicon Dimers," *J. Phys. Chem. C*, vol. 117, no. 26, pp. 13573–13584, Jul. 2013.

[15] T. Grosjean, M. Mivelle, F. I. Baida, G. W. Burr, and U. C. Fischer, "Diabolo Nanoantenna for Enhancing and Confining the Magnetic Optical Field," *Nano Lett.*, vol. 11, no. 3, pp. 1009–1013, Mar. 2011.

[16] A. Alu and N. Engheta, "The quest for magnetic plasmons at optical frequencies," *Opt. Express*, vol. 17, no. 7, p. 5723, Mar. 2009.

[17] C. Guclu, M. Veysi, and F. Capolino, "Photoinduced Magnetic Nanoprobe Excited by an Azimuthally Polarized Vector Beam," *ACS Photonics*, vol. 3, no. 11, pp. 2049–2058, Nov. 2016.

[18] K. Yao and Y. Liu, "Controlling Electric and Magnetic Resonances for Ultracompact Nanoantennas with Tunable Directionality," *ACS Photonics*, vol. 3, no. 6, pp. 953–963, Jun. 2016.

[19] M. Darvishzadeh-Varcheie, C. Guclu, and F. Capolino, "Magnetic Nanoantennas Made of Plasmonic Nanoclusters for Photoinduced Magnetic Field Enhancement," *Phys. Rev. Appl.*, vol. 8, no. 2, p. 024033, Aug. 2017.

[20] N. P. Montoni, S. C. Quillin, C. Cherqui, and D. J. Masiello, "Tunable Spectral Ordering of Magnetic Plasmon Resonances in Noble Metal Nanoclusters," *ACS Photonics*, vol. 5, no. 8, pp. 3272–3281, Aug. 2018.

[21] A. García-Etxarri *et al.*, "Strong magnetic response of submicron Silicon particles in the infrared," *Opt. Express*, vol. 19, no. 6, pp. 4815–4826, Mar. 2011.

[22] G. Boudarham, R. Abdeddaim, and N. Bonod, “Enhancing the magnetic field intensity with a dielectric gap antenna,” *Appl. Phys. Lett.*, vol. 104, no. 2, p. 021117, Jan. 2014.
[23] B. Hopkins, A. E. Miroshnichenko, and Y. S. Kivshar, “All-Dielectric Nanophotonic Structures: Exploring the Magnetic Component of Light,” in *Recent Trends in Computational Photonics*, A. Agrawal, T. Benson, R. M. De La Rue, and G. A. Wurtz, Eds. Cham: Springer International Publishing, 2017, pp. 285–313.
[24] S. Sun, R. Li, M. Li, Q. Du, C. E. Png, and P. Bai, “Hybrid Mushroom Nanoantenna for Fluorescence Enhancement by Matching the Stokes Shift of the Emitter,” *J. Phys. Chem. C*, vol. 122, no. 26, pp. 14771–14780, Jul. 2018.
[25] J. Zeng *et al.*, “Exclusive Magnetic Excitation Enabled by Structured Light Illumination in a Nanoscale Mie Resonator,” *ACS Nano*, vol. 12, no. 12, pp. 12159–12168, Dec. 2018.
[26] J. Zeng *et al.*, “In pursuit of photo-induced magnetic and chiral microscopy,” *EPJ Appl. Metamaterials*, vol. 5, p. 7, 2018.
[27] X. Wei, T. Wei, H. Xiao, and Y. S. Lin, “Nano-structured Pd-long period fiber gratings integrated optical sensor for hydrogen detection,” *Sens. Actuators B Chem.*, vol. 134, no. 2, pp. 687–693, Sep. 2008.
[28] C. Perrotton *et al.*, “A reliable, sensitive and fast optical fiber hydrogen sensor based on surface plasmon resonance,” *Opt. Express*, vol. 21, no. 1, p. 382, Jan. 2013.
[29] X. Zhao *et al.*, “A nano-opto-mechanical pressure sensor via ring resonator,” *Opt. Express*, vol. 20, no. 8, p. 8535, Apr. 2012.
[30] J. N. Dash, R. Jha, J. Villatoro, and S. Dass, “Nano-displacement sensor based on photonic crystal fiber modal interferometer,” *Opt. Lett.*, vol. 40, no. 4, p. 467, Feb. 2015.
[31] C. Preininger, I. Klimant, and O. S. Wolfbeis, “Optical Fiber Sensor for Biological Oxygen Demand,” *Anal. Chem.*, vol. 66, no. 11, pp. 1841–1846, Jun. 1994.
[32] S. Pandey, G. K. Goswami, and K. K. Nanda, “Green synthesis of biopolymer-silver nanoparticle nanocomposite: an optical sensor for ammonia detection,” *Int. J. Biol. Macromol.*, vol. 51, no. 4, pp. 583–589, Nov. 2012.
[33] J. Song *et al.*, “Electrical tracing-assisted dual-microring label-free optical bio/chemical sensors,” *Opt. Express*, vol. 20, no. 4, p. 4189, Feb. 2012.
[34] M. Khorasaninejad, N. Clarke, M. P. Anantram, and S. S. Saini, “Optical bio-chemical sensors on SNOW ring resonators,” *Opt. Express*, vol. 19, no. 18, p. 17575, Aug. 2011.
[35] S. Korposh *et al.*, “Fiber optic long period grating sensors with a nanoassembled mesoporous film of SiO_2 nanoparticles,” *Opt. Express*, vol. 18, no. 12, p. 13227, Jun. 2010.
[36] G. Lu *et al.*, “Live-Cell SERS Endoscopy Using Plasmonic Nanowire Waveguides,” *Adv. Mater.*, vol. 26, no. 30, pp. 5124–5128, Aug. 2014.
[37] P. Negri, J. Y. Choi, C. Jones, S. M. Tompkins, R. A. Tripp, and R. A. Dluhy, “Identification of Virulence Determinants in Influenza Viruses,” *Anal. Chem.*, vol. 86, no. 14, pp. 6911–6917, Jul. 2014.
[38] S. Steshenko, F. Capolino, P. Alitalo, and S. Tretyakov, “Effective model and investigation of the near-field enhancement and subwavelength imaging properties of multilayer arrays of plasmonic nanospheres,” *Phys. Rev. E*, vol. 84, no. 1, p. 016607, Jul. 2011.
[39] A. J. Haes and R. P. V. Duyne, “Preliminary studies and potential applications of localized surface plasmon resonance spectroscopy in medical diagnostics,” *Expert Rev. Mol. Diagn.*, vol. 4, no. 4, pp. 527–537, Jul. 2004.
[40] B. P. Rand, P. Peumans, and S. R. Forrest, “Long-range absorption enhancement in organic tandem thin-film solar cells containing silver nanoclusters,” *J. Appl. Phys.*, vol. 96, no. 12, pp. 7519–7526, Dec. 2004.
[41] K. Hering *et al.*, “SERS: a versatile tool in chemical and biochemical diagnostics,” *Anal. Bioanal. Chem.*, vol. 390, no. 1, pp. 113–124, Nov. 2007.
[42] S. Nie and S. R. Emory, “Probing Single Molecules and Single Nanoparticles by Surface-Enhanced Raman Scattering,” *Science*, vol. 275, no. 5303, pp. 1102–1106, Feb. 1997.

[43] K. Kneipp *et al.*, "Single Molecule Detection Using Surface-Enhanced Raman Scattering (SERS)," *Phys. Rev. Lett.*, vol. 78, no. 9, pp. 1667–1670, Mar. 1997.
[44] Z. Li *et al.*, "A plasmonic staircase nano-antenna device with strong electric field enhancement for surface enhanced Raman scattering (SERS) applications," *J. Phys. Appl. Phys.*, vol. 45, no. 30, p. 305102, 2012.
[45] K. Kneipp, H. Kneipp, and J. Kneipp, "Surface-Enhanced Raman Scattering in Local Optical Fields of Silver and Gold NanoaggregatesFrom Single-Molecule Raman Spectroscopy to Ultrasensitive Probing in Live Cells," *Acc. Chem. Res.*, vol. 39, no. 7, pp. 443–450, Jul. 2006.
[46] B. Yan, A. Thubagere, W. R. Premasiri, L. D. Ziegler, L. Dal Negro, and B. M. Reinhard, "Engineered SERS Substrates with Multiscale Signal Enhancement: Nanoparticle Cluster Arrays," *ACS Nano*, vol. 3, no. 5, pp. 1190–1202, May 2009.
[47] A. J. Pasquale, B. M. Reinhard, and L. Dal Negro, "Engineering Photonic–Plasmonic Coupling in Metal Nanoparticle Necklaces," *ACS Nano*, vol. 5, no. 8, pp. 6578–6585, Aug. 2011.
[48] S. Campione, C. Guclu, R. Ragan, and F. Capolino, "Fano resonances in metasurfaces made of linear trimers of plasmonic nanoparticles," *Opt. Lett.*, vol. 38, no. 24, pp. 5216–5219, Dec. 2013.
[49] S. Campione, C. Guclu, R. Ragan, and F. Capolino, "Enhanced Magnetic and Electric Fields via Fano Resonances in Metasurfaces of Circular Clusters of Plasmonic Nanoparticles," *ACS Photonics*, vol. 1, no. 3, pp. 254–260, Mar. 2014.
[50] J. J. Mock, S. M. Norton, S.-Y. Chen, A. A. Lazarides, and D. R. Smith, "Electromagnetic Enhancement Effect Caused by Aggregation on SERS-Active Gold Nanoparticles," *Plasmonics*, vol. 6, no. 1, pp. 113–124, Oct. 2010.
[51] S. Campione, S. M. Adams, R. Ragan, and F. Capolino, "Comparison of electric field enhancements: Linear and triangular oligomers versus hexagonal arrays of plasmonic nanospheres," *Opt. Express*, vol. 21, no. 7, p. 7957, Apr. 2013.
[52] S. M. Adams, S. Campione, F. Capolino, and R. Ragan, "Directing Cluster Formation of Au Nanoparticles from Colloidal Solution," *Langmuir*, vol. 29, no. 13, pp. 4242–4251, Apr. 2013.
[53] S. M. Adams *et al.*, "Non-lithographic SERS substrates: tailoring surface chemistry for Au nanoparticle cluster assembly," *Small Weinh. Bergstr. Ger.*, vol. 8, no. 14, pp. 2239–2249, Jul. 2012.
[54] W. Zhu and K. B. Crozier, "Quantum mechanical limit to plasmonic enhancement as observed by surface-enhanced Raman scattering," *Nat. Commun.*, vol. 5, p. 5228, Oct. 2014.
[55] J. H. Choi, S. M. Adams, and R. Ragan, "Design of a versatile chemical assembly method for patterning colloidal nanoparticles," *Nanotechnology*, vol. 20, no. 6, p. 065301, Feb. 2009.
[56] D. D. John *et al.*, "Multilayer Platform for Ultra-Low-Loss Waveguide Applications," *IEEE Photonics Technol. Lett.*, vol. 24, no. 11, pp. 876–878, Jun. 2012.
[57] D. J. Moss, R. Morandotti, A. L. Gaeta, and M. Lipson, "New CMOS-compatible platforms based on silicon nitride and Hydex for nonlinear optics," *Nat. Photonics*, vol. 7, no. 8, pp. 597–607, Aug. 2013.
[58] S. Romero-García, F. Merget, F. Zhong, H. Finkelstein, and J. Witzens, "Silicon nitride CMOS-compatible platform for integrated photonics applications at visible wavelengths," *Opt. Express*, vol. 21, no. 12, p. 14036, Jun. 2013.
[59] O. Boyraz and B. Jalali, "Demonstration of directly modulated silicon Raman laser," *Opt. Express*, vol. 13, no. 3, pp. 796–800, Feb. 2005.
[60] J. S. Levy, A. Gondarenko, M. A. Foster, A. C. Turner-Foster, A. L. Gaeta, and M. Lipson, "CMOS-compatible multiple-wavelength oscillator for on-chip optical interconnects," *Nat. Photonics*, vol. 4, no. 1, pp. 37–40, Jan. 2010.
[61] K. Ikeda, R. E. Saperstein, N. Alic, and Y. Fainman, "Thermal and Kerr nonlinear properties of plasma-deposited silicon nitride/ silicon dioxide waveguides," *Opt. Express*, vol. 16, no. 17, p. 12987, Aug. 2008.
[62] S. Minissale, S. Yerci, and L. D. Negro, "Nonlinear optical properties of low temperature annealed silicon-rich oxide and silicon-rich nitride materials for silicon photonics," *Appl. Phys. Lett.*, vol. 100, no. 2, p. 021109, Jan. 2012.

[63] Y. Huang, Q. Zhao, L. Kamyab, A. Rostami, F. Capolino, and O. Boyraz, "Sub-micron silicon nitride waveguide fabrication using conventional optical lithography," 2014, p. JT3A.27.
[64] W. Thrift *et al.*, "Bridging the Gap between Crosslinking Chemistry and Directed Assembly of Metasurfaces Using Electrohydrodynamic Flow," *ArXiv160906964 Cond-Mat Physicsphysics*, Aug. 2016.
[65] R. W. Taylor *et al.*, "Precise Subnanometer Plasmonic Junctions for SERS within Gold Nanoparticle Assemblies Using Cucurbit[n]uril 'Glue,'" *ACS Nano*, vol. 5, no. 5, pp. 3878–3887, May 2011.
[66] J. A. Fan *et al.*, "DNA-Enabled Self-Assembly of Plasmonic Nanoclusters," *Nano Lett.*, vol. 11, no. 11, pp. 4859–4864, Nov. 2011.
[67] V. V. Thacker *et al.*, "DNA origami based assembly of gold nanoparticle dimers for surface-enhanced Raman scattering," *Nat. Commun.*, vol. 5, p. 3448, Mar. 2014.
[68] I. H. Stein, V. Schüller, P. Böhm, P. Tinnefeld, and T. Liedl, "Single-Molecule FRET Ruler Based on Rigid DNA Origami Blocks," *ChemPhysChem*, vol. 12, no. 3, pp. 689–695, Feb. 2011.
[69] Q. Ruan, L. Shao, Y. Shu, J. Wang, and H. Wu, "Growth of Monodisperse Gold Nanospheres with Diameters from 20 nm to 220 nm and Their Core/Satellite Nanostructures," *Adv. Opt. Mater.*, vol. 2, no. 1, pp. 65–73, Jan. 2014.
[70] P. B. Johnson and R. W. Christy, "Optical Constants of the Noble Metals," *Phys. Rev. B*, vol. 6, no. 12, pp. 4370–4379, Dec. 1972.
[71] J. Theiss, P. Pavaskar, P. M. Echternach, R. E. Muller, and S. B. Cronin, "Plasmonic Nanoparticle Arrays with Nanometer Separation for High-Performance SERS Substrates," *Nano Lett.*, vol. 10, no. 8, pp. 2749–2754, Aug. 2010.
[72] W. Thrift *et al.*, "Surface enhanced Raman scattering for detection of Pseudomonas aeruginosa quorum sensing compounds," 2015, vol. 9550, pp. 95500B-95500B–13.
[73] M. Darvishzadeh-Varcheie, C. Guclu, R. Ragan, O. Boyraz, and F. Capolino, "Field enhancement with plasmonic nano-antennas on silicon-based waveguides," 2015, p. 95473E.
[74] M. D. Varcheie, Q. Zhao, C. Guclu, R. Ragan, O. Boyraz, and F. Capolino, "Field enhancement and optical trapping with plasmonic nano antennas on silicon-based waveguides," in *Radio Science Meeting (Joint with AP-S Symposium), 2015 USNC-URSI*, 2015, pp. 350–350.
[75] K. C. Neuman and A. Nagy, "Single-molecule force spectroscopy: optical tweezers, magnetic tweezers and atomic force microscopy," *Nat. Methods*, vol. 5, no. 6, pp. 491–505, Jun. 2008.
[76] J. A. Dionne, "Towards all-optical chiral resolution with achiral plasmonic and dielectric nanostructures (Conference Presentation)," in *Complex Light and Optical Forces XII*, 2018, vol. 10549, p. 1054913.
[77] J. Jahng *et al.*, "Linear and Nonlinear Optical Spectroscopy at the Nanoscale with Photoinduced Force Microscopy," *Acc. Chem. Res.*, vol. 48, no. 10, pp. 2671–2679, Oct. 2015.
[78] J. Zeng *et al.*, "Sharply Focused Azimuthally Polarized Beams with Magnetic Dominance: Near-Field Characterization at Nanoscale by Photoinduced Force Microscopy," *ACS Photonics*, vol. 5, no. 2, pp. 390–397, Feb. 2018.
[79] M. Kamandi *et al.*, "Enantiospecific Detection of Chiral Nanosamples Using Photoinduced Force," *Phys. Rev. Appl.*, vol. 8, no. 6, p. 064010, Dec. 2017.
[80] D. Nowak *et al.*, "Nanoscale chemical imaging by photoinduced force microscopy," *Sci. Adv.*, vol. 2, no. 3, p. e1501571, Mar. 2016.
[81] A. Serdyukov, I. Semchenko, S. Tretyakov, and A. Sihvola, *Electromagnetics of bi-anisotropic materials : theory and applications*. Australia: Gordon and Breach Science, 2001.
[82] I. V. Lindell, A. H. Sihvola, S. A. Tretyakov, and A. J. vitanen, *Electromagnetic Waves in Chiral and Bi-Isotropic Media*. Boston: Artech House, 1994.
[83] T. Mackay and A. Lakhtakia, *Electromagnetic Anisotropy and Bianisotropy - A Field Guide*. London: World Scientific Publishing, 2010.
[84] S. Campione and F. Capolino, "Ewald method for 3D periodic dyadic Green's functions and complex modes in composite materials made of spherical particles under the dual dipole approximation," *Radio Sci.*, vol. 47, no. 6, p. RS0N06, Dec. 2012.

[85] D. Jackson, *Classical Electrodynamics*. New York: Wiley, 1998.
[86] M. Kamandi, S.-M.-H. Emadi, and R. Faraji-Dana, "Integral Equation Analysis of Multilayered Waveguide Bends Using Complex Images Green's Function Technique," *J. Light. Technol.*, vol. 33, no. 9, pp. 1774–1779, May 2015.
[87] T. Tumkur *et al.*, "Wavelength-Dependent Optical Force Imaging of Bimetallic Al–Au Heterodimers," *Nano Lett.*, vol. 18, no. 3, pp. 2040–2046, Mar. 2018.
[88] R. Alaee, C. Rockstuhl, and I. Fernandez-Corbaton, "An electromagnetic multipole expansion beyond the long-wavelength approximation," *Opt. Commun.*, vol. 407, pp. 17–21, Jan. 2018.
[89] V. S. Asadchy, I. A. Faniayeu, Y. Ra'di, and S. A. Tretyakov, "Determining polarizability tensors for an arbitrary small electromagnetic scatterer," *Photonics Nanostructures - Fundam. Appl.*, vol. 12, no. 4, pp. 298–304, Aug. 2014.
[90] M. Veysi, C. Guclu, and F. Capolino, "Vortex beams with strong longitudinally polarized magnetic field and their generation by using metasurfaces," *JOSA B*, vol. 32, no. 2, pp. 345–354, Feb. 2015.
[91] J. P. Gordon, "Radiation Forces and Momenta in Dielectric Media," *Phys. Rev. A*, vol. 8, no. 1, pp. 14–21, Jul. 1973.
[92] D. Gao *et al.*, "Optical manipulation from the microscale to the nanoscale: fundamentals, advances and prospects," *Light Sci. Appl.*, vol. 6, no. 9, p. e17039, Sep. 2017.
[93] M. Albooyeh *et al.*, "Photo-induced force vs power in chiral scatterrers," in *2017 IEEE International Symposium on Antennas and Propagation USNC/URSI National Radio Science Meeting*, 2017, pp. 35–36.
[94] J. Zeng *et al.*, "In pursuit of photo-induced magnetic and chiral microscopy," *EPJ Appl. Metamaterials*, vol. 5, p. 7, 2018.
[95] J. Jahng *et al.*, "Gradient and scattering forces in photoinduced force microscopy," *Phys. Rev. B*, vol. 90, no. 15, p. 155417, Oct. 2014.
[96] K. L. Kelly et al., "The Optical Properties of Metal Nanoparticles: The Influence of Size, Shape, and Dielectric Environment," *J. Phys. Chem. B*, vol. 107, no. 3, pp. 668–677, Jan. 2003.
[97] P. K. Jain, K. S. Lee, I. H. El-Sayed, and M. A. El-Sayed, "Calculated Absorption and Scattering Properties of Gold Nanoparticles of Different Size, Shape, and Composition: Applications in Biological Imaging and Biomedicine," *J. Phys. Chem. B*, vol. 110, no. 14, pp. 7238–7248, Apr. 2006.
[98] M. Darvishzadeh-Varcheie, C. Guclu, and F. Capolino, "Magnetic Nanoantennas Made of Plasmonic Nanoclusters for Photoinduced Magnetic Field Enhancement," *Phys. Rev. Appl.*, vol. 8, no. 2, p. 024033, Aug. 2017.
[99] M. Darvishzadeh-Varcheie, C. Guclu, R. Ragan, O. Boyraz, and F. Capolino, "Electric field enhancement with plasmonic colloidal nanoantennas excited by a silicon nitride waveguide," *Opt. Express*, vol. 24, no. 25, pp. 28337–28352, Dec. 2016.
[100] C. F. Bohren, "PhD Thesis," University of Arizona, 1975.
[101] M. Veysi, C. Guclu, and F. Capolino, "Focused azimuthally polarized vector beam and spatial magnetic resolution below the diffraction limit," *JOSA B*, vol. 33, no. 11, pp. 2265–2277, Nov. 2016.
[102] C. Guclu, M. Veysi, and F. Capolino, "Photoinduced Magnetic Nanoprobe Excited by an Azimuthally Polarized Vector Beam," *ACS Photonics*, vol. 3, no. 11, pp. 2049–2058, Nov. 2016.
[103] S. Campione and F. Capolino, "Ewald method for 3D periodic dyadic Green's functions and complex modes in composite materials made of spherical particles under the dual dipole approximation," *Radio Sci.*, vol. 47, no. 6, p. RS0N06, Dec. 2012.
[104] N. Tischler *et al.*, "Experimental control of optical helicity in nanophotonics," *Light Sci. Appl.*, vol. 3, no. 6, p. e183, Jun. 2014.
[105] I. Fernandez-Corbaton, "Helicity and duality symmetry in light matter interactions: Theory and applications," *ArXiv14074432 Phys.*, Jul. 2014.
[106] C. Guclu, V. A. Tamma, H. K. Wickramasinghe, and F. Capolino, "Photo-induced Magnetic Force Between Nanostructures," *Phys. Rev. B*, vol. 92, no. 23, Dec. 2015.

[107] R. F. Oulton, G. Bartal, D. F. P. Pile, and X. Zhang, "Confinement and propagation characteristics of subwavelength plasmonic modes," *New J. Phys.*, vol. 10, no. 10, p. 105018, 2008.
[108] S. M. Adams *et al.*, "Non-lithographic SERS Substrates: Tailoring Surface Chemistry for Au Nanoparticle Cluster Assembly," *Small*, vol. 8, no. 14, pp. 2239–2249, Jul. 2012.
[109] S. M. Adams, S. Campione, F. Capolino, and R. Ragan, "Directing Cluster Formation of Au Nanoparticles from Colloidal Solution," *Langmuir*, vol. 29, no. 13, pp. 4242–4251, Apr. 2013.
[110] J. A. Fan *et al.*, "Self-Assembled Plasmonic Nanoparticle Clusters," *Science*, vol. 328, no. 5982, pp. 1135–1138, May 2010.
[111] A. Baron, A. Aradian, V. Ponsinet, and P. Barois, "[INVITED] Self-assembled optical metamaterials," *Opt. Laser Technol.*, vol. 82, pp. 94–100, Aug. 2016.
[112] W. J. Thrift *et al.*, "Driving Chemical Reactions in Plasmonic Nanogaps with Electrohydrodynamic Flow," *ACS Nano*, vol. 11, no. 11, pp. 11317–11329, Nov. 2017.
[113] C. Q. Nguyen *et al.*, "Longitudinal Monitoring of Biofilm Formation via Robust Surface-Enhanced Raman Scattering Quantification of Pseudomonas aeruginosa-Produced Metabolites," *ACS Appl. Mater. Interfaces*, vol. 10, no. 15, pp. 12364–12373, Apr. 2018.
[114] R. Fuchs and F. Claro, "Multipolar response of small metallic spheres: Nonlocal theory," *Phys. Rev. B*, vol. 35, no. 8, pp. 3722–3727, Mar. 1987.
[115] C. Ciracì *et al.*, "Probing the Ultimate Limits of Plasmonic Enhancement," *Science*, vol. 337, no. 6098, pp. 1072–1074, Aug. 2012.
[116] C. David and F. J. García de Abajo, "Spatial Nonlocality in the Optical Response of Metal Nanoparticles," *J. Phys. Chem. C*, vol. 115, no. 40, pp. 19470–19475, Oct. 2011.
[117] A. I. Fernández-Domínguez, A. Wiener, F. J. García-Vidal, S. A. Maier, and J. B. Pendry, "Transformation-Optics Description of Nonlocal Effects in Plasmonic Nanostructures," *Phys. Rev. Lett.*, vol. 108, no. 10, p. 106802, Mar. 2012.
[118] S. Raza, S. I. Bozhevolnyi, M. Wubs, and N. A. Mortensen, "Nonlocal optical response in metallic nanostructures," *J. Phys. Condens. Matter*, vol. 27, no. 18, p. 183204, 2015.
[119] Y. Huang, L. Ma, M. Hou, J. Li, Z. Xie, and Z. Zhang, "Hybridized plasmon modes and near-field enhancement of metallic nanoparticle-dimer on a mirror," *Sci. Rep.*, vol. 6, Jul. 2016.
[120] S. S. Wang and R. Magnusson, "Theory and applications of guided-mode resonance filters," *Appl. Opt.*, vol. 32, no. 14, pp. 2606–2613, May 1993.
[121] S. Zou, N. Janel, and G. C. Schatz, "Silver nanoparticle array structures that produce remarkably narrow plasmon lineshapes," *J. Chem. Phys.*, vol. 120, no. 23, pp. 10871–10875, May 2004.
[122] D. C. Skigin and M. Lester, "Study of resonant modes of a periodic metallic array near a dielectric interface: evanescent-to-propagating coupling via surface plasmon excitation," *J. Opt. Pure Appl. Opt.*, vol. 8, no. 3, p. 259, 2006.
[123] V. G. Kravets, F. Schedin, and A. N. Grigorenko, "Extremely Narrow Plasmon Resonances Based on Diffraction Coupling of Localized Plasmons in Arrays of Metallic Nanoparticles," *Phys. Rev. Lett.*, vol. 101, no. 8, p. 087403, Aug. 2008.
[124] B. Auguié and W. L. Barnes, "Collective Resonances in Gold Nanoparticle Arrays," *Phys. Rev. Lett.*, vol. 101, no. 14, p. 143902, Sep. 2008.
[125] N. J. Halas, S. Lal, W.-S. Chang, S. Link, and P. Nordlander, "Plasmons in Strongly Coupled Metallic Nanostructures," *Chem. Rev.*, vol. 111, no. 6, pp. 3913–3961, Jun. 2011.
[126] V. Giannini, A. I. Fernández-Domínguez, S. C. Heck, and S. A. Maier, "Plasmonic Nanoantennas: Fundamentals and Their Use in Controlling the Radiative Properties of Nanoemitters," *Chem. Rev.*, vol. 111, no. 6, pp. 3888–3912, Jun. 2011.
[127] D. Wang, W. Zhu, Y. Chu, and K. B. Crozier, "High Directivity Optical Antenna Substrates for Surface Enhanced Raman Scattering," *Adv. Mater.*, vol. 24, no. 32, pp. 4376–4380.
[128] M. Shyiq Amin, J. Woong Yoon, and R. Magnusson, "Optical transmission filters with coexisting guided-mode resonance and Rayleigh anomaly," *Appl. Phys. Lett.*, vol. 103, no. 13, p. 131106, Sep. 2013.

[129] G. S. Bisht *et al.*, "Controlled Continuous Patterning of Polymeric Nanofibers on Three-Dimensional Substrates Using Low-Voltage Near-Field Electrospinning," *Nano Lett.*, vol. 11, no. 4, pp. 1831–1837, Apr. 2011.
[130] W. Thrift *et al.*, "Surface enhanced Raman scattering for detection of Pseudomonas aeruginosa quorum sensing compounds," 2015, vol. 9550, pp. 95500B-95500B–13.
[131] M. Laroche, S. Albaladejo, R. Gómez-Medina, and J. J. Sáenz, "Tuning the optical response of nanocylinder arrays: An analytical study," *Phys. Rev. B*, vol. 74, no. 24, p. 245422, Dec. 2006.
[132] P. Ghenuche *et al.*, "Optical Extinction in a Single Layer of Nanorods," *Phys. Rev. Lett.*, vol. 109, no. 14, p. 143903, Oct. 2012.
[133] H. Marinchio, R. Carminati, A. García-Martín, and J. J. Sáenz, "Magneto-optical Kerr effect in resonant subwavelength nanowire gratings," *New J. Phys.*, vol. 16, no. 1, p. 015007, 2014.
[134] R. Gomez-Medina, M. Laroche, and J. J. Sáenz, "Extraordinary optical reflection from sub-wavelength cylinder arrays," *Opt. Express*, vol. 14, no. 9, pp. 3730–3737, May 2006.
[135] S. Albaladejo *et al.*, "Radiative corrections to the polarizability tensor of an electrically small anisotropic dielectric particle," *Opt. Express*, vol. 18, no. 4, pp. 3556–3567, Feb. 2010.
[136] S. Campione and F. Capolino, "Ewald method for 3D periodic dyadic Green's functions and complex modes in composite materials made of spherical particles under the dual dipole approximation," *Radio Sci.*, vol. 47, no. 6, p. RS0N06, Dec. 2012.
[137] M. Haghtalab and R. Faraji-Dana, "Integral equation analysis and optimization of 2D layered nanolithography masks by complex images Green's function technique in TM polarization," *JOSA A*, vol. 29, no. 5, pp. 748–756, May 2012.
[138] S. Steshenko and F. Capolino, "Single Dipole Approximation for Modeling Collections of Nanoscatterers," in *Theory and Phenomena of Metamaterials*, CRC Press, 2009.
[139] M. Darvishzadeh-Varcheie, C. Guclu, and F. Capolino, "Magnetic Nanoantennas Made of Plasmonic Nanoclusters for Photoinduced Magnetic Field Enhancement," *Phys. Rev. Appl.*, vol. 8, no. 2, p. 024033, Aug. 2017.
[140] J. D. Jackson, *Classical Electrodynamics*, 3rd ed. Wiley, 1998.
[141] S. Linden, J. Kuhl, and H. Giessen, "Controlling the Interaction between Light and Gold Nanoparticles: Selective Suppression of Extinction," *Phys. Rev. Lett.*, vol. 86, no. 20, pp. 4688–4691, May 2001.
[142] A. D. Humphrey and W. L. Barnes, "Plasmonic surface lattice resonances in arrays of metallic nanoparticle dimers," *J. Opt.*, vol. 18, no. 3, p. 035005, 2016.
[143] D. Maystre, "Theory of Wood's Anomalies," in *Plasmonics: From Basics to Advanced Topics*, S. Enoch and N. Bonod, Eds. Berlin, Heidelberg: Springer Berlin Heidelberg, 2012, pp. 39–83.
[144] D. B. Mazulquim *et al.*, "Efficient band-pass color filters enabled by resonant modes and plasmons near the Rayleigh anomaly," *Opt. Express*, vol. 22, no. 25, pp. 30843–30851, Dec. 2014.
[145] N. J. H. N. K. Grady, "Grady, N. K., Halas, N. J. & Nordlander, P. Influence of dielectric function properties on the optical response of plasmon resonant metallic nanoparticles. Chem. Phys. Lett. 399, 167-171," *Chem. Phys. Lett.*, vol. 399, no. 1–3, pp. 167–171, 2004.
[146] J. Theiss, P. Pavaskar, P. M. Echternach, R. E. Muller, and S. B. Cronin, "Plasmonic Nanoparticle Arrays with Nanometer Separation for High-Performance SERS Substrates," *Nano Lett.*, vol. 10, no. 8, pp. 2749–2754, Aug. 2010.
[147] M. Veysi, C. Guclu, and F. Capolino, "Vortex beams with strong longitudinally polarized magnetic field and their generation by using metasurfaces," *JOSA B*, vol. 32, no. 2, pp. 345–354, Feb. 2015.
[148] K. Kneipp, H. Kneipp, and J. Kneipp, "Surface-Enhanced Raman Scattering in Local Optical Fields of Silver and Gold NanoaggregatesFrom Single-Molecule Raman Spectroscopy to Ultrasensitive Probing in Live Cells," *Acc. Chem. Res.*, vol. 39, no. 7, pp. 443–450, Jul. 2006.
[149] K. Kneipp *et al.*, "Single Molecule Detection Using Surface-Enhanced Raman Scattering (SERS)," *Phys. Rev. Lett.*, vol. 78, no. 9, pp. 1667–1670, Mar. 1997.
[150] J.-M. Nam, J.-W. Oh, H. Lee, and Y. D. Suh, "Plasmonic Nanogap-Enhanced Raman Scattering with Nanoparticles," *Acc. Chem. Res.*, vol. 49, no. 12, pp. 2746–2755, Dec. 2016.

[151] D. O. Sigle *et al.*, "Observing Single Molecules Complexing with Cucurbit[7]uril through Nanogap Surface-Enhanced Raman Spectroscopy," *J. Phys. Chem. Lett.*, vol. 7, no. 4, pp. 704–710, Feb. 2016.
[152] F. Capolino, D. R. Wilton, and W. A. Johnson, "Efficient computation of the 2-D Green's function for 1-D periodic structures using the Ewald method," *IEEE Trans. Antennas Propag.*, vol. 53, no. 9, pp. 2977–2984, Sep. 2005.
[153] F. T. Celepcikay, D. R. Wilton, D. R. Jackson, and F. Capolino, "Choosing splitting parameters and summation limits in the numerical evaluation of 1-D and 2-D periodic Green's functions using the Ewald method," *Radio Sci.*, vol. 43, no. 6, p. RS6S01, Dec. 2008.
[154] N. G. Bastús, J. Comenge, and V. Puntes, "Kinetically Controlled Seeded Growth Synthesis of Citrate-Stabilized Gold Nanoparticles of up to 200 nm: Size Focusing versus Ostwald Ripening," *Langmuir*, vol. 27, no. 17, pp. 11098–11105, Sep. 2011.
[155] M. Burresi *et al.*, "Probing the Magnetic Field of Light at Optical Frequencies," *Science*, vol. 326, no. 5952, pp. 550–553, Oct. 2009.
[156] H. Giessen and R. Vogelgesang, "Glimpsing the Weak Magnetic Field of Light," *Science*, vol. 326, no. 5952, pp. 529–530, Oct. 2009.
[157] T. H. Taminiau, S. Karaveli, N. F. van Hulst, and R. Zia, "Quantifying the magnetic nature of light emission," *Nat. Commun.*, vol. 3, p. 979, Jul. 2012.
[158] M. Kasperczyk, S. Person, D. Ananias, L. D. Carlos, and L. Novotny, "Excitation of Magnetic Dipole Transitions at Optical Frequencies," *Phys. Rev. Lett.*, vol. 114, no. 16, p. 163903, Apr. 2015.
[159] A. Alu and N. Engheta, "The quest for magnetic plasmons at optical frequencies," *Opt. Express*, vol. 17, no. 7, p. 5723, Mar. 2009.
[160] P. Albella *et al.*, "Low-Loss Electric and Magnetic Field-Enhanced Spectroscopy with Subwavelength Silicon Dimers," *J. Phys. Chem. C*, vol. 117, no. 26, pp. 13573–13584, Jul. 2013.
[161] L. Zou *et al.*, "Dielectric resonator nanoantennas at visible frequencies," *Opt. Express*, vol. 21, no. 1, pp. 1344–1352, Jan. 2013.
[162] G. N. Malheiros-Silveira, G. S. Wiederhecker, and H. E. Hernández-Figueroa, "Dielectric resonator antenna for applications in nanophotonics," *Opt. Express*, vol. 21, no. 1, pp. 1234–1239, Jan. 2013.
[163] R. Verre, Z. J. Yang, T. Shegai, and M. Käll, "Optical Magnetism and Plasmonic Fano Resonances in Metal–Insulator–Metal Oligomers," *Nano Lett.*, vol. 15, no. 3, pp. 1952–1958, Mar. 2015.
[164] R. S. Savelev, S. V. Makarov, A. E. Krasnok, and P. A. Belov, "From optical magnetic resonance to dielectric nanophotonics (A review)," *Opt. Spectrosc.*, vol. 119, no. 4, pp. 551–568, Oct. 2015.
[165] D. Markovich *et al.*, "Enhancement of artificial magnetism via resonant bianisotropy," *Sci. Rep.*, vol. 6, Mar. 2016.
[166] T. J. Yen *et al.*, "Terahertz Magnetic Response from Artificial Materials," *Science*, vol. 303, no. 5663, pp. 1494–1496, Mar. 2004.
[167] J. D. Baena, R. Marqués, F. Medina, and J. Martel, "Artificial magnetic metamaterial design by using spiral resonators," *Phys. Rev. B*, vol. 69, no. 1, p. 014402, Jan. 2004.
[168] A. N. Lagarkov and A. K. Sarychev, "Electromagnetic properties of composites containing elongated conducting inclusions," *Phys. Rev. B*, vol. 53, no. 10, pp. 6318–6336, Mar. 1996.
[169] G. Dolling, C. Enkrich, M. Wegener, J. F. Zhou, C. M. Soukoulis, and S. Linden, "Cut-wire pairs and plate pairs as magnetic atoms for optical metamaterials," *Opt. Lett.*, vol. 30, no. 23, pp. 3198–3200, Dec. 2005.
[170] S. Linden *et al.*, "Photonic Metamaterials: Magnetism at Optical Frequencies," *IEEE J. Sel. Top. Quantum Electron.*, vol. 12, no. 6, pp. 1097–1105, Nov. 2006.
[171] C. M. Soukoulis, S. Linden, and M. Wegener, "Negative Refractive Index at Optical Wavelengths," *Science*, vol. 315, no. 5808, pp. 47–49, Jan. 2007.
[172] V. M. Shalaev, "Optical negative-index metamaterials," *Nat. Photonics*, vol. 1, no. 1, pp. 41–48, Jan. 2007.
[173] J. B. Pendry, A. J. Holden, D. J. Robbins, and W. J. Stewart, "Magnetism from conductors and enhanced nonlinear phenomena," *IEEE Trans. Microw. Theory Tech.*, vol. 47, pp. 2075–2084, Nov. 1999.

[174] R. A. Shelby, D. R. Smith, and S. Schultz, "Experimental Verification of a Negative Index of Refraction," *Science*, vol. 292, no. 5514, pp. 77–79, Apr. 2001.
[175] K. Aydin, I. Bulu, K. Guven, M. Kafesaki, C. M. Soukoulis, and E. Ozbay, "Investigation of magnetic resonances for different split-ring resonator parameters and designs," *New J. Phys.*, vol. 7, no. 1, p. 168, 2005.
[176] J. Zhou, Th. Koschny, M. Kafesaki, E. N. Economou, J. B. Pendry, and C. M. Soukoulis, "Saturation of the Magnetic Response of Split-Ring Resonators at Optical Frequencies," *Phys. Rev. Lett.*, vol. 95, no. 22, p. 223902, Nov. 2005.
[177] S. Linden, C. Enkrich, M. Wegener, J. Zhou, T. Koschny, and C. M. Soukoulis, "Magnetic Response of Metamaterials at 100 Terahertz," *Science*, vol. 306, no. 5700, pp. 1351–1353, Nov. 2004.
[178] C. Enkrich *et al.*, "Magnetic Metamaterials at Telecommunication and Visible Frequencies," *Phys. Rev. Lett.*, vol. 95, no. 20, p. 203901, Nov. 2005.
[179] N. Katsarakis *et al.*, "Magnetic response of split-ring resonators in the far-infrared frequency regime," *Opt. Lett.*, vol. 30, no. 11, pp. 1348–1350, Jun. 2005.
[180] T. D. Corrigan, P. W. Kolb, A. B. Sushkov, H. D. Drew, D. C. Schmadel, and R. J. Phaneuf, "Optical plasmonic resonances in split-ring resonator structures: an improved LC model," *Opt. Express*, vol. 16, no. 24, pp. 19850–19864, Nov. 2008.
[181] M. S. Wheeler, J. S. Aitchison, and M. Mojahedi, "Three-dimensional array of dielectric spheres with an isotropic negative permeability at infrared frequencies," *Phys. Rev. B*, vol. 72, no. 19, p. 193103, Nov. 2005.
[182] S. Campione, S. Lannebère, A. Aradian, M. Albani, and F. Capolino, "Complex modes and artificial magnetism in three-dimensional periodic arrays of titanium dioxide microspheres at millimeter waves," *JOSA B*, vol. 29, no. 7, pp. 1697–1706, Jul. 2012.
[183] S. Campione, M. B. Sinclair, and F. Capolino, "Effective medium representation and complex modes in 3D periodic metamaterials made of cubic resonators with large permittivity at mid-infrared frequencies," *Photonics Nanostructures - Fundam. Appl.*, vol. 11, no. 4, pp. 423–435, Nov. 2013.
[184] S. Lannebère, S. Campione, A. Aradian, M. Albani, and F. Capolino, "Artificial magnetism at terahertz frequencies from three-dimensional lattices of TiO_2 microspheres accounting for spatial dispersion and magnetoelectric coupling," *JOSA B*, vol. 31, no. 5, pp. 1078–1086, May 2014.
[185] C. R. Simovski and S. A. Tretyakov, "Model of isotropic resonant magnetism in the visible range based on core-shell clusters," *Phys. Rev. B*, vol. 79, no. 4, p. 045111, Jan. 2009.
[186] A. Vallecchi, M. Albani, and F. Capolino, "Collective electric and magnetic plasmonic resonances in spherical nanoclusters," *Opt. Express*, vol. 19, no. 3, p. 2754, Jan. 2011.
[187] S. Mühlig *et al.*, "Self-Assembled Plasmonic Core–Shell Clusters with an Isotropic Magnetic Dipole Response in the Visible Range," *ACS Nano*, vol. 5, no. 8, pp. 6586–6592, Aug. 2011.
[188] A. Vallecchi, M. Albani, and F. Capolino, "Effect of irregularities of nanosatellites position and size on collective electric and magnetic plasmonic resonances in spherical nanoclusters," *Opt. Express*, vol. 21, no. 6, p. 7667, Mar. 2013.
[189] Z. Qian *et al.*, "Raspberry-like Metamolecules Exhibiting Strong Magnetic Resonances," *ACS Nano*, vol. 9, no. 2, pp. 1263–1270, Feb. 2015.
[190] S. Campione and F. Capolino, "Electromagnetic coupling and array packing induce exchange of dominance on complex modes in 3D periodic arrays of spheres with large permittivity," *JOSA B*, vol. 33, no. 2, pp. 261–270, Feb. 2016.
[191] D. K. Morits and C. R. Simovski, "Negative effective permeability at optical frequencies produced by rings of plasmonic dimers," *Phys. Rev. B*, vol. 81, no. 20, p. 205112, May 2010.
[192] A. Alù, A. Salandrino, and N. Engheta, "Negative effective permeability and left-handed materials at optical frequencies," *Opt. Express*, vol. 14, no. 4, p. 1557, Feb. 2006.
[193] M. Hentschel, M. Saliba, R. Vogelgesang, H. Giessen, A. P. Alivisatos, and N. Liu, "Transition from Isolated to Collective Modes in Plasmonic Oligomers," *Nano Lett.*, vol. 10, no. 7, pp. 2721–2726, Jul. 2010.

[194] B. Luk'yanchuk *et al.*, "The Fano resonance in plasmonic nanostructures and metamaterials," *Nat. Mater.*, vol. 9, no. 9, pp. 707–715, Sep. 2010.
[195] S. N. Sheikholeslami, A. García-Etxarri, and J. A. Dionne, "Controlling the Interplay of Electric and Magnetic Modes via Fano-like Plasmon Resonances," *Nano Lett.*, vol. 11, no. 9, pp. 3927–3934, Sep. 2011.
[196] N. Liu *et al.*, "Manipulating Magnetic Plasmon Propagation in Metallic Nanocluster Networks," *ACS Nano*, vol. 6, no. 6, pp. 5482–5488, Jun. 2012.
[197] C. Guclu, M. Veysi, M. Darvishzadeh-Varcheie, and F. Capolino, "Artificial Magnetism via Nanoantennas under Azimuthally Polarized Vector Beam Illumination," 2016, p. JW2A.21.
[198] C. Guclu, M. Veysi, M. Darvishzadeh-Vercheie, and F. Capolino, "Optical nanoantennas as magnetic nanoprobes for enhancing light-matter interaction," in *2016 10th International Congress on Advanced Electromagnetic Materials in Microwaves and Optics (METAMATERIALS)*, 2016, pp. 391–393.
[199] F. Shafiei *et al.*, "A subwavelength plasmonic metamolecule exhibiting magnetic-based optical Fano resonance," *Nat. Nanotechnol.*, vol. 8, no. 2, pp. 95–99, Feb. 2013.
[200] A. E. Krasnok, A. E. Miroshnichenko, P. A. Belov, and Y. S. Kivshar, "All-dielectric optical nanoantennas," *Opt. Express*, vol. 20, no. 18, pp. 20599–20604, Aug. 2012.
[201] R. Hussain *et al.*, "Enhancing Eu^3+ magnetic dipole emission by resonant plasmonic nanostructures," *Opt. Lett.*, vol. 40, no. 8, p. 1659, Apr. 2015.
[202] C. Guclu, M. Veysi, and F. Capolino, "Photoinduced Magnetic Nanoprobe Excited by an Azimuthally Polarized Vector Beam," *ACS Photonics*, vol. 3, no. 11, pp. 2049–2058, Nov. 2016.
[203] A. I. Kuznetsov, A. E. Miroshnichenko, M. L. Brongersma, Y. S. Kivshar, and B. Luk'yanchuk, "Optically resonant dielectric nanostructures," *Science*, vol. 354, no. 6314, p. aag2472, Nov. 2016.
[204] R. Wilson, "The use of gold nanoparticles in diagnostics and detection," *Chem. Soc. Rev.*, vol. 37, no. 9, pp. 2028–2045, Aug. 2008.
[205] G. L. Nealon, B. Donnio, R. Greget, J.-P. Kappler, E. Terazzi, and J.-L. Gallani, "Magnetism in gold nanoparticles," *Nanoscale*, vol. 4, no. 17, pp. 5244–5258, Aug. 2012.
[206] G. Peng *et al.*, "Diagnosing lung cancer in exhaled breath using gold nanoparticles," *Nat. Nanotechnol.*, vol. 4, no. 10, pp. 669–673, Oct. 2009.
[207] S. Zeng, K.-T. Yong, I. Roy, X.-Q. Dinh, X. Yu, and F. Luan, "A Review on Functionalized Gold Nanoparticles for Biosensing Applications," *Plasmonics*, vol. 6, no. 3, pp. 491–506, Apr. 2011.
[208] D. Liu, Z. Wang, and X. Jiang, "Gold nanoparticles for the colorimetric and fluorescent detection of ions and small organic molecules," *Nanoscale*, vol. 3, no. 4, pp. 1421–1433, Apr. 2011.
[209] C. Wu *et al.*, "Fano-resonant asymmetric metamaterials for ultrasensitive spectroscopy and identification of molecular monolayers," *Nat. Mater.*, vol. 11, no. 1, pp. 69–75, Jan. 2012.
[210] Z. Zhang, R. D. Ross, and R. K. Roeder, "Preparation of functionalized gold nanoparticles as a targeted X-ray contrast agent for damaged bone tissue," *Nanoscale*, vol. 2, no. 4, p. 582, 2010.
[211] M. Veysi, C. Guclu, and F. Capolino, "Vortex beams with strong longitudinally polarized magnetic field and their generation by using metasurfaces," *J. Opt. Soc. Am. B*, vol. 32, no. 2, p. 345, Feb. 2015.
[212] M. Veysi, C. Guclu, and F. Capolino, "Focused azimuthally polarized vector beam and spatial magnetic resolution below the diffraction limit," *JOSA B*, vol. 33, no. 11, pp. 2265–2277, Nov. 2016.
[213] S. Steshenko and F. Capolino, "Single Dipole Approximation for Modeling Collections of Nanoscatterers," in *Theory and Phenomena of Metamaterials*, CRC Press, 2009.
[214] S. Campione, S. M. Adams, R. Ragan, and F. Capolino, "Comparison of electric field enhancements: linear and triangular oligomers versus hexagonal arrays of plasmonic nanospheres," *Opt. Express*, vol. 21, no. 7, pp. 7957–7973, Apr. 2013.
[215] N. J. H. N. K. Grady, "Grady, N. K., Halas, N. J. & Nordlander, P. Influence of dielectric function properties on the optical response of plasmon resonant metallic nanoparticles. Chem. Phys. Lett. 399, 167-171," *Chem. Phys. Lett.*, vol. 399, no. 1–3, pp. 167–171, 2004.
[216] J. D. Jackson, *Classical Electrodynamics*, 3rd ed. Wiley, 1998.

[217] A. Vallecchi, S. Campione, and F. Capolino, “Symmetric and antisymmetric resonances in a pair of metal-dielectric nanoshells: tunability and closed-form formulas,” *J. Nanophotonics*, vol. 4, no. 1, pp. 041577-041577–13, 2010.
[218] A. Vallecchi and F. Capolino, “Metamaterials Based on Pairs of Tightly Coupled Scatterers,” in *Theory and Phenomena of Metamaterials*, CRC Press, 2009.
[219] L. Li and C.-H. Liang, “ANALYSIS OF RESONANCE AND QUALITY FACTOR OF ANTENNA AND SCATTERING SYSTEMS USING COMPLEX FREQUENCY METHOD COMBINED WITH MODEL-BASED PARAMETER ESTIMATION,” *Prog. Electromagn. Res.*, vol. 46, pp. 165–188, 2004.
[220] R. Carminati, J.-J. Greffet, C. Henkel, and J. M. Vigoureux, “Radiative and non-radiative decay of a single molecule close to a metallic nanoparticle,” *Opt. Commun.*, vol. 261, no. 2, pp. 368–375, May 2006.
[221] L. Novotny and B. Hecht, *Principles of Nano-Optics*, 2nd ed. Cambridge University Press, 2012.
[222] I. Liberal, Y. Ra’di, R. Gonzalo, I. Ederra, S. A. Tretyakov, and R. W. Ziolkowski, “Least Upper Bounds of the Powers Extracted and Scattered by Bi-anisotropic Particles,” *IEEE Trans. Antennas Propag.*, vol. 62, no. 9, pp. 4726–4735, Sep. 2014.
[223] I. Liberal, I. Ederra, R. Gonzalo, and R. W. Ziolkowski, “Upper Bounds on Scattering Processes and Metamaterial-Inspired Structures That Reach Them,” *IEEE Trans. Antennas Propag.*, vol. 62, no. 12, pp. 6344–6353, Dec. 2014.
[224] C. M. Dodson and R. Zia, “Magnetic dipole and electric quadrupole transitions in the trivalent lanthanide series: Calculated emission rates and oscillator strengths,” *Phys. Rev. B*, vol. 86, no. 12, p. 125102, Sep. 2012.
[225] N. Yang, Y. Tang, and A. E. Cohen, “Spectroscopy in sculpted fields,” *Nano Today*, vol. 4, no. 3, pp. 269–279, Jun. 2009.
[226] F. T. Rabouw, P. T. Prins, and D. J. Norris, “Europium-Doped NaYF4 Nanocrystals as Probes for the Electric and Magnetic Local Density of Optical States throughout the Visible Spectral Range,” *Nano Lett.*, vol. 16, no. 11, pp. 7254–7260, Nov. 2016.
[227] B. Choi, M. Iwanaga, Y. Sugimoto, K. Sakoda, and H. T. Miyazaki, “Selective Plasmonic Enhancement of Electric- and Magnetic-Dipole Radiations of Er Ions,” *Nano Lett.*, vol. 16, no. 8, pp. 5191–5196, Aug. 2016.
[228] J. Li, N. Verellen, and P. Van Dorpe, “Enhancing Magnetic Dipole Emission by a Nano-Doughnut-Shaped Silicon Disk,” *ACS Photonics*, vol. 4, no. 8, pp. 1893–1898, Aug. 2017.
[229] D. J. Richardson, J. Nilsson, and W. A. Clarkson, “High power fiber lasers: current status and future perspectives [Invited],” *JOSA B*, vol. 27, no. 11, pp. B63–B92, Nov. 2010.
[230] T. H. Taminiau, S. Karaveli, N. F. van Hulst, and R. Zia, “Quantifying the magnetic nature of light emission,” *Nat. Commun.*, vol. 3, p. 979, Jul. 2012.
[231] S. Karaveli, A. J. Weinstein, and R. Zia, “Direct Modulation of Lanthanide Emission at Sub-Lifetime Scales,” *Nano Lett.*, vol. 13, no. 5, pp. 2264–2269, May 2013.
[232] R. Hussain *et al.*, “Enhancing Eu^3+ magnetic dipole emission by resonant plasmonic nanostructures,” *Opt. Lett.*, vol. 40, no. 8, p. 1659, Apr. 2015.
[233] M. Mivelle, T. Grosjean, G. W. Burr, U. C. Fischer, and M. F. Garcia-Parajo, “Strong Modification of Magnetic Dipole Emission through Diabolo Nanoantennas,” *ACS Photonics*, vol. 2, no. 8, pp. 1071–1076, Aug. 2015.
[234] D. N. Chigrin, D. Kumar, D. Cuma, and G. von Plessen, “Emission Quenching of Magnetic Dipole Transitions near a Metal Nanoparticle,” *ACS Photonics*, vol. 3, no. 1, pp. 27–34, Jan. 2016.
[235] M. Sanz-Paz *et al.*, “Enhancing Magnetic Light Emission with All-Dielectric Optical Nanoantennas,” *Nano Lett.*, vol. 18, no. 6, pp. 3481–3487, Jun. 2018.
[236] M. Veysi, C. Guclu, and F. Capolino, “Focused azimuthally polarized vector beam and spatial magnetic resolution below the diffraction limit,” *JOSA B*, vol. 33, no. 11, pp. 2265–2277, Nov. 2016.

[237] Z. Gao, L. Shen, E. Li, L. Xu, and Z. Wang, "Cross-Diabolo Nanoantenna for Localizing and Enhancing Magnetic Field With Arbitrary Polarization," *J. Light. Technol.*, vol. 30, no. 6, pp. 829–833, Mar. 2012.
[238] Y. Chen, Y. Chen, J. Chu, and X. Xu, "Bridged Bowtie Aperture Antenna for Producing an Electromagnetic Hot Spot," *ACS Photonics*, vol. 4, no. 3, pp. 567–575, Mar. 2017.
[239] A. E. Krasnok, A. E. Miroshnichenko, P. A. Belov, and Y. S. Kivshar, "All-dielectric optical nanoantennas," *Opt. Express*, vol. 20, no. 18, pp. 20599–20604, Aug. 2012.
[240] D. Permyakov *et al.*, "Probing magnetic and electric optical responses of silicon nanoparticles," *Appl. Phys. Lett.*, vol. 106, no. 17, p. 171110, Apr. 2015.
[241] R. S. Savelev, S. V. Makarov, A. E. Krasnok, and P. A. Belov, "From optical magnetic resonance to dielectric nanophotonics (A review)," *Opt. Spectrosc.*, vol. 119, no. 4, pp. 551–568, Oct. 2015.
[242] R. Alaee, M. Albooyeh, A. Rahimzadegan, M. S. Mirmoosa, Y. S. Kivshar, and C. Rockstuhl, "All-dielectric reciprocal bianisotropic nanoparticles," *Phys. Rev. B*, vol. 92, no. 24, p. 245130, Dec. 2015.
[243] A. I. Kuznetsov, A. E. Miroshnichenko, M. L. Brongersma, Y. S. Kivshar, and B. Luk'yanchuk, "Optically resonant dielectric nanostructures," *Science*, vol. 354, no. 6314, p. aag2472, Nov. 2016.
[244] T. Feng, Y. Xu, Z. Liang, and W. Zhang, "All-dielectric hollow nanodisk for tailoring magnetic dipole emission," *Opt. Lett.*, vol. 41, no. 21, pp. 5011–5014, Nov. 2016.
[245] W. H. Weber and G. W. Ford, "Optical electric-field enhancement at a metal surface arising from surface-plasmon excitation," *Opt. Lett.*, vol. 6, no. 3, pp. 122–124, Mar. 1981.
[246] A. Bouhelier, M. Beversluis, A. Hartschuh, and L. Novotny, "Near-Field Second-Harmonic Generation Induced by Local Field Enhancement," *Phys. Rev. Lett.*, vol. 90, no. 1, p. 013903, Jan. 2003.
[247] M. Kamandi, C. Guclu, T. S. Luk, G. T. Wang, and F. Capolino, "Giant field enhancement in longitudinal epsilon-near-zero films," *Phys. Rev. B*, vol. 95, no. 16, p. 161105, Apr. 2017.
[248] J. Zeng *et al.*, "Sharply Focused Azimuthally Polarized Beams with Magnetic Dominance: Near-Field Characterization at Nanoscale by Photoinduced Force Microscopy," *ACS Photonics*, vol. 5, no. 2, pp. 390–397, Feb. 2018.
[249] M. Kasperczyk, S. Person, D. Ananias, L. D. Carlos, and L. Novotny, "Excitation of Magnetic Dipole Transitions at Optical Frequencies," *Phys. Rev. Lett.*, vol. 114, no. 16, p. 163903, Apr. 2015.
[250] P. Woźniak, P. Banzer, and G. Leuchs, "Selective switching of individual multipole resonances in single dielectric nanoparticles," *Laser Photonics Rev.*, vol. 9, no. 2, pp. 231–240, 2015.
[251] M. Veysi, C. Guclu, and F. Capolino, "Vortex beams with strong longitudinally polarized magnetic field and their generation by using metasurfaces," *J. Opt. Soc. Am. B*, vol. 32, no. 2, p. 345, Feb. 2015.
[252] N. K. Grady, N. J. Halas, and P. Nordlander, "Influence of dielectric function properties on the optical response of plasmon resonant metallic nanoparticles," *Chem. Phys. Lett.*, vol. 399, no. 1, pp. 167–171, Nov. 2004.